DESIGN AND VALIDATION OF THE BALL LENS-BASED INTRAVASCULAR CATHETER FOR OPTICAL COHERENCE TOMOGRAPHY AND FLUORESCENCE LIFETIME IMAGING MICROSCOPY

A Dissertation

by

XI CHEN

Submitted to the Office of Graduate and Professional Studies of
Texas A&M University
in partial fulfillment of the requirements for the degree of

DOCTOR OF PHILOSOPHY

Chair of Committee,	Brian E. Applegate
Co-Chair of Committee,	Javier A. Jo
Committee Members,	Vladislav V. Yakovlev
	Jim Ji
Head of Department,	Mike McShane

December 2020

Major Subject: Biomedical Engineering

ABSTRACT

Diagnosis of atherosclerosis requires morphological and biochemical information in vivo and one single imaging system cannot provide comprehensive details. Therefore, researchers have been interested in combining two different imaging systems to diagnose atherosclerosis simultaneously with fiber endoscope. This dissertation focuses on the development of dual-modality ball lens-based fiber endoscope for Optical Coherence Tomography (OCT) and Fluorescence Lifetime Imaging Microscopy (FLIM) for intravascular atherosclerosis diagnosis.

We proposed a combined simulation, fabrication, and measurement method for ball lens-based endoscope based on double clad fiber (DCF) for OCT and FLIM. Simulation is important to minimize manufacturing time by establishing a preferred shape for the partial ellipsoid lens before optimizing the manufacturing process. It also allows us, in conjunction with optical performance characterization techniques, to predict the performance of any given endoscope in the intravascular environment. Different fiber endoscopes based on different fiber were designed, optimized and fabricated for OCT system, Time-Domain FLIM system, Frequency-Domain FLIM system, and dual-modality OCT/FLIM system. Each type endoscope optical performance, mechanical performance and application to atherosclerosis was confirmed with a series of experiments.

The dual-modality OCT/FLIM system compatible with the endoscope was designed and developed. The operating wavelength for OCT and FLIM were 1310nm and 375nm, respectively. The combined system was used to image atherosclerosis through a dual-modality ball lens-based endoscope. The morphological and biochemical information of the atherosclerosis images were

collected and studied. The whole system also was minimized inside the moveable cart for convenient usage.

DEDICATION

To my parents and my fiancée.

ACKNOWLEDGEMENTS

I would like to thank my advisors Dr. Brian Applegate and Dr. Javier Jo, who gave me the chance to work in such a fantastic research environment. I am grateful for their guidance and support while researching and working at Texas A&M University (TAMU). Dr. Applegate guided me how to research in a new field, including finding an interesting and useful research topic, designing and developing optical imaging systems, and testing and troubleshooting the system. Dr. Jo helped me a lot in animal sample preparation for imaging as well as histopathological analysis besides research knowledge and methods. Advices given by two advisors have been a great help in my academic career and my future research life.

I would like to thank Dr. Vladislav Yakovlev for helping me understand the fundamentals of scattering and non-linear optics in his course. I would also like to thank him for his time and energy to serve on my committee.

I would like to thank Dr. Jim Ji for teaching me useful and interesting fundamentals of imaging processing. I would also like to thank him for his time and energy to serve on my committee.

I would like to appreciate Michael J. Serafino for his tremendous cooperation on the system synchronization, excellent acquisition code and processing algorithm, and very kind discussion about the project. I would also like to thank Wihan Kim for his knowledgeable recommendation and kind cooperation on the project. Also, my special thanks go to all other former and current team members of this OCT-FLIM project – Jesung Park, Paritosh Pande, Shrestha Sebina, Jesus Rico Jimenez, Zheng Tan and Julia Buck.

I would like to acknowledge our collaborator at UT Medical Center, Dr. Brian Walton for his suggestions and support. I appreciate him for clinical application of an OCT-FLIM imaging system in animals during cardiac surgery. Also, I would like to thank Rosalva Munoz for all the administrative and research support along the whole project.

I also would like to thank Sangmin Kim for his support and suggestion. We took courses, worked on projects, and ate lunch during PhD life. He gave me lots of support to my research and my personal life. I would like to extend my appreciation to Shrestha Sebina, Wihan Kim, Scott Mattison, Jeremy Pearson and Esteban Carbajal for their warm welcome to the lab. I also want to thank Shuna Cheng, Zhaokai Meng, Felipe Zambrano, Elvis Duran, Rodrigo Cuenca, Ronald Juarez and Jorge Palma for their suggestions and support.

I would like to thank to Barbara Slusher for placing numerous orders for the research. I would also like to thank Carl Johnson for fabricating lots of optic-mechanical components for the project. Their support helped me design and fabricate endoscopes.

Finally, I would like to thank my family. I would like to take this opportunity to express my gratitude to my parents for their love and encouragement all my life. Their love, support and encourage helped me overcome difficult days and hard time of my life. Thanks to my fiancée Liang Liang for her support and happiness she gave me all the time. Thank you for your assistance, encouragement and accompany.

CONTRIBUTORS AND FUNDING SOURCES

Contributors

This work was supervised by a dissertation committee consisting of Dr. Brian Applegate (advisor), Dr. Javier Jo (co-advisor) and Dr. Vladislav Yakovlev of the Department of Biomedical Engineering and Dr. Jim Ji of the Department of Electrical and Computer Engineering.

The optical imaging system automation and processing algorithm was developed by Michael J. Serafino. The rotary joint was designed and developed by Wihan Kim. All other work conducted for the dissertation was completed by the student.

Funding Sources

Graduate study was supported by a research assistantship from Texas A&M University and the project is supported by NIH 5R01HL111361-02.

NOMENCLATURE

APD	Avalanche Photodiode
BF	Bandpass Filter
BS	Beam Splitter
CF	Coreless Fiber
CT	Computed Tomography
DCF	Double Clad Fiber
DS	Dichroic Mirror
DOF	Depth of Focus
FAD	Flavin Adenine Dinucleotide
FDFLIM	Frequency-Domain Fluorescence Lifetime Imaging Microscopy
FDOCT	Frequency-Domain Optical Coherence Tomography
FLIM	Fluorescence Lifetime Imaging Microscopy
FOV	Field of View
FWHM	Full Width at Half of Maximum
GRIN	Gradient Index
IACUC	Institutional Animal Care and Use Committee
ID	Inner Diameter
IVUS	Intravascular Ultrasound
LDL	Low-density Lipoprotein
MMF	Multimode fiber
MRI	Magnetic Resonance Imaging

NA	Numerical Aperture
NADH	Nicotinamide Adenine Dinucleotide
NIR	Near Infrared
NURD	Nonuniform Rotational Distortion
OCT	Optical Coherence Tomography
OD	Outer Diameter
PBS	Phosphate Buffer Saline
PMT	Photo-Multiplier Tube
POP	Physical Optics Propagation
POPOP	1,4-bis(5-phenyloxazol-2-yl) benzene
SDOCT	Spectral-Domain Optical Coherence Tomography
SMF	Single-Mode Fiber
SNR	Signal-to-Noise Ratio
SSOCT	Swept Source Optical Coherence Tomography
VCSEL	Vertical-Cavity Surface-Emitting Laser
VIS	Visible
TCFA	Thin Cap Fibroatheroma
TDOCT	Time-Domain OCT
UV	Ultraviolet

TABLE OF CONTENTS

Page

LIST OF FIGURES

Page

LIST OF TABLES

Page

1. INTRODUCTION

1.1 Motivation

Research in biomedical imaging focuses on research and application on technique for non-invasively or minimally invasive optical imaging method for diseases. Over the last century, biomedical imaging techniques was growing rapidly for more diseases which were not well understood and treated.

Atherosclerosis is the leading cause of morbidity and mortality in the United States and other industrialized countries[1, 2]. It is characterized as a systemic, progressive disease in which the arterial wall thickens through a process of inflammation[3, 4], oxidative stress, and dyslipidemia. As the result of inflammation, atherosclerosis with early- and intermediate plaques has signs of leukocyte recruitment, replication of macrophages, degradation of elastin and collagen, lipid-laden cores[5-7]. These artery plaques may finally rupture leading to sudden thrombosis and occlusion of the vessel[8] which obstructs blood flow to the heart (coronary heart disease), brain (ischemic stroke), or lower extremities[6]. However, the mechanisms and progression of atherosclerosis is complex and still unknown, and more detailed detection of the progression is required. Also, future development of treatment for atherosclerosis also depends on a more detailed understanding of plaque development. Therefore, better biomedical imaging methods for diagnosis of atherosclerosis with high sensitivity and specificity is important.

In general, diagnostical imaging system detect the biomarkers of the disease, and a few biomarkers related with atherosclerosis progression have been identified and will be discussed below.

Blood vessels are usually composed of three layers, the tunica intima which is a single layer of endothelial cell, tunica medial which is the thickest layer, and tunica adventitia. The intima

is thinnest layer composed of a single layer of endothelial cell. The media is the thickest layer, composed of smooth muscle cells, elastic fibers consisting of elastin and connective tissue. The atherosclerosis often begins with intimal thickening which is present in infants, while intimal smooth muscle cell secreting proteoglycan to attract lipoproteins. The increase of intimal lipoproteins leads to initiation of adhesion which facilitates the attachment of monocytes on endothelial cells as an early step in inflammation called monocyte infiltration [9]. The infiltrated macrophages promote oxidation of LDL accumulating within the deep intima as lipid pool, and update of oxidized LDL transformed macrophage into foam cells[9].

Necrotic core formation is attributed to the death of macrophage [10], and one subsequent pathway is fibroatheroma which has a fibrous cap consisting smooth muscle cells and matrix, over the foam cell, and then finally formed thin cap fibroatheroma (TCFA). The thin fibrous cap disrupts leading to the plaque ruptures which is defined as a lesion consisting of a necrotic core with an overlying thin disrupted fibrous cap [11].

Erosion occurring in the absence of rupture and thrombi are direct contact with intimal. The third coronary thrombosis is calcified nodule, which is defined as highly calcified coronary arteries. Percentage of plaque morphologies leading to acute coronary syndromes with thrombi is rupture (55-60%), erosion (30-35%), and calcified nodule (3-7%) [12][*].

Based on atherosclerosis progression, optical imaging systems are designed to detect different morphological and biochemical biomarkers. Optical imaging systems detect the response of human tissue to light, including volume scattering and absorption within tissue, reflection and

[*] The process of atherosclerosis is beyond the scope of this study and scheme for classifying atherosclerotic lesions is referred to reference.

transmission at tissue external surface and multi-layers boundary (e.g. intima and media)[13]. Different optical imaging systems were developed and implemented for plaque diagnosis.

As the atherosclerosis progresses, the thickness of the artery changes, plaque area and thickness change, and necrotic core extends. One important morphological parameter differentiating thin-cap fibroatheroma (TCFA) from ruptures, is the thickness of fibrous cap over the necrotic core <65 um. Therefore, the imaging method for morphological information for atherosclerosis should resolve the TCFA. In the other words, the imaging system should have an axial resolution that is sufficient to measure a few tens of microns. Also, the area of fibrous cap overlying above plaque and the necrotic core area size are other two important morphological parameters, which requires a sufficient lateral resolution to measure the size of the structure.

Intravascular ultrasound (IVUS) investigation has 70-200 μm axial resolution with >5mm penetration[14], which is capable to measure thickness of arterial intima-media complex[15] and differentiate between vessel layers and tissue types[16]. However, IVUS cannot reach the order of a few tens of microns to measure accurately fibrous cap's thickness of 65-150 μm, the predictor of unstable plaque. Magnetic Resonance Imaging (MRI) often provides the resolution of 80 μm-1 mm for characterization of atherosclerosis[17-19]. However, the acquisition in the order of from minutes to hours are long for in vivo monitoring[14, 20]. Optical Coherence Tomography (OCT) improves the spatial resolution and acquisition speed to visualize coronary artery with the high axial resolution and lateral resolution of ~10-20um in the order of seconds[21-24]. The thickness of tunica intima of the diseased arteries are below 1mm [25]. However, the limited tissue penetration of ~2mm leads to inability to image adventitia. Besides these imaging methods, such as Angioscopy, Computed tomography (CT) and others, also can give morphology information.

On the contrary, the plaque biochemical composition is also related with vulnerability of rupture and autofluorescence could be used as biochemical biomarkers. Biomarkers include lipid contents in plaques[26], and relative content of collagen and lipids within plaque[8]. They are related with endothelial activation, macrophage infiltration and apoptosis. Foam cell accumulates and collagen content increases in the early to middle stage, and vulnerable plaque has a lipid filled with necrotic core[27].

A few imaging modalities use autofluorescence to provide biochemical information[28-31]. Fluorescence Lifetime Imaging Microscopy (FLIM) is capable of quantifying the collagen, elastin, and lipid contents, and distinguishing between fibrotic and fibro-lipid plaques[26, 27, 32]. Near-infrared spectroscopy (NIRF) used the excitation of near infrared, was capable of necrotic cores which is significant for vulnerable plaque[33, 34].

Combination of two imaging modalities has been adopted by a number of groups to increase sensitivity and specificity for characterization of different disease. For example, some groups developed systems combining OCT and FLIM[35, 36], IVUS and FLIM[37], OCT and NIRF[33], IVUS and OCT[38], PET and CT[39], MRI and FLIM[40]. Different imaging modalities should be capable of combination and give complementary information[9] for dual-modality imaging system.

The combination of OCT and FLIM can provide complementary information of atherosclerosis, including morphological information and biochemical information. OCT has been shown to be capable of providing high-resolution information regarding structural components of plaque in humans [24, 41-43]. The tens of microns axial resolution, much better than IVUS and MRI, is sufficient to distinguish fibrous cap, which is the significant marker for TCFA, and assess late stent expansion and neointima growth pattern. Also, OCT is able to overcome two

shortcomings of IVUS, detection of lipid-rich lesions and assessment of calcified lesions. Current OCT solely can give us sensitivity and specificity of (89%, 93%)[24]. On the contrary, autofluorescence features of atherosclerotic plaques can be used to characterize plaque composition, and these biochemical markers include the relative content of collagen and lipids within plaques, and fluorescence lipids and lipoproteins[26, 29, 44]. Current FLIM technology solely can give us sensitivity and specificity of (85%, 95%)[45], (81%, 94%)[32], and (89%, 98%)[27]. Two types of information can help increase specificity and sensitivity, and facilitate signal interpretation. For example, Wang et at. combined OCT and fluorescence imaging for early bladder cancer diagnosis, to increase sensitivity and specificity of 79% and 53% only by fluorescence imaging to 100% and 81% with OCT[46]. OCT can increase specificity mainly because of hyperplastic lesions with low backscattering but high fluorescence. In addition, considering the IVUS's correction for fluorescence imaging, the fluorescence spectroscopy can be corrected by OCT for unknown subsurface structures[47].

Current understanding of atherosclerosis is mainly based on postmortem histopathology studies[8, 12]. In vivo imaging of morphological and biochemical changes accompanying plaque formation and response to treatment[48] is important for building our understanding of plaque formation and it will likely play a significant role in clinical diagnosis, monitoring and treatment of the disease. In vivo monitoring of molecular biomarkers related to endothelial activation, macrophage recruitment and activation, apoptosis among other mechanism, will be also crucial for improving understanding of plaque development[49]. To facilitate in vivo diagnosis, dual modality OCT/FLIM system requires endoscope system.

Optical fiber-based endoscopes were used for a variety of medical imaging applications [50] including intravascular investigation of atherosclerotic plaques [51, 52]. Many groups have

developed different side-imaging endoscopic OCT [51], which emitted and collected light at the side of the endoscope. The first side imaging endoscope was designed by Graded-Index (GRIN) lens and right angle prism[53], however, the outer diameter of the endoscope is 1.1 mm. The GRIN fiber-based endoscope and ball lens-based endoscope were also develop later[54]. A few groups used ABCD matrix to simulate the output of OCT endoscope [55-61], but the simulation and measurement for side-viewing endoscope was not validated, due to the fact that the system was not circularly symmetric and not paraxial for side view endoscope. In addition, it had chromatic aberration and astigmatism[60]. At the same time, designed FLIM catheter is also needed for clinical use in vivo. A number of scientific groups successfully developed FLIM catheters[37, 50, 62] based on grin lens, prism, or ball-lens. However, they didn't develop simulation methods to accurately predict the resolution. There were some groups developing double clad fiber (DCF) for some endoscope[34, 63, 64], showing that new fiber technology's potential for OCT/FLIM catheter.

From the discussion above, it is evident that dual-modality OCT/FLIM system can improve the atherosclerosis diagnosis. Also, a robust and accurate simulation method for different types of endoscope should be proposed and confirmed. Last, different types of endoscopes for OCT, FLIM, and dual-modality OCT/FLIM should be designed and fabricated.

1.2 Objective and Dissertation Outline

The goal of the project is to develop ball-lens based endoscope for dual-modality Swept-Source Optical Coherence Tomography (SSOCT) and Frequency-Domain Fluorescence Lifetime Imaging Microscopy (FDFLIM) system for intravascular disease diagnosis and detection. These aims are achieved in stages.

To begin, a general simulation, fabrication, and measurement method was proposed for ball lens-based endoscope based on single mode fiber (SMF), multimode fiber (MMF), and double clad fiber (DCF). Different optical propagation algorithms were analyzed and the optimal optical simulation models were proposed for different applications. The fabrication approach was also analyzed and standard operating process was proposed to minimize fabrication duration and tolerance. Finally, the measurement method and setup were prepared to validate the simulation and fabrication process.

At the same time, dual-modality OCT and FLIM system was designed and developed. The OCT subsystem is designed to have a scan depth of more than 1mm with high axial resolution, fast scanning speed and large enough lateral field of view. The FLIM subsystem is designed to have a good lateral resolution of smaller than 100 μm while collecting emission from the tissue. The shared common path compatible with the endoscope was designed to combine both optical imaging systems with high efficiency.

Subsequently, endoscope for Time-Domain Fluorescence Lifetime Imaging Microscopy (TDFLIM) based on MMF, endoscope for OCT based on SMF, endoscope for FDFLIM based on DCF and endoscope for OCT/FLIM based on DCF were designed and optimized based on simulation method, then were fabricated and validated with respective optical imaging system. The optical property and mechanical property were validated during the development process to improve endoscope fabrication process. Later, postmortem human arteries with a wide variety of plaques were imaged with the respective system. Arteries were characterized with the imaging system, and then analyzed with the corresponding histopathological slides.

Finally, accessories for in-vivo characterization were designed and prepared, including catheter housing and sterilization process. The system was improved for in vivo characterization. The endoscope was made for Watanbe rabbits in clinical settings.

This dissertation mainly focuses on the design, development and validation of dual modality OCT and FLIM system with endoscope for atherosclerosis. In this dissertation, the acquisition system of OCT and FLIM was built, and 3 types of endoscopes were designed and fabricated for experiments.

Chapter 2 discussed the fundamentals of beam propagation theory in air space and through fiber, and principles of OCT and FLIM respectively. The first sub-section covers the theory of beam propagation in air space and through fiber, and fiber principle, which is the fundamental for endoscope design and simulation. The second sub-section covers the fundamentals of the SSOCT and key parameters. The third sub-section covers the fundamental of FLIM, including TDFLIM and FDFLIM, and implementation methods.

Chapter 3 described the development and fabrication process of endoscope based on different types of fibers. It discusses the fabrication process, principle, and tolerance control for the fusion splicer. Details for each endoscope for specific application are described in respective chapter.

Chapter 4 covers the combined simulation, fabrication, and measurement method for ball lens-based endoscope based on multimode fiber. This chapter also validates the capability of the endoscope based on MMF for intravascular TDFLIM.

Chapter 5 covers the combined simulation, fabrication, and measurement method for ball lens-based endoscope based on DCF. This chapter also demonstrates the FDFLIM system for

intravascular application, and validates the capability of the endoscope based on DCF for intravascular FDFLIM.

Chapter 6 covers the combined simulation, fabrication, and measurement method for ball lens-based endoscope based on DCF. This chapter also demonstrates the dual modality SSOCT/FDFLIM system for intravascular application and validates the capability of the endoscope based on DCF for SSOCT/FDFLIM system.

Chapter 7 discusses some of the limitations of the system and improvement to be approached for better performance. Insights from the latest research finding for future work have also been included.

Chapter 8 summarizes the dissertation.

2. FUNDAMENTALS OF OPTICAL COHERENCE TOMOGRAPHY, FLUORESCENCE LIFETIME IMAGING MICROSCOPY AND ENDOSCOPE

This chapter discusses beam propagation theory, fundamentals of Optical Coherence Tomography (OCT) and fundamentals of Fluorescence Lifetime Imaging Microscopy (FLIM). The first sub-section covers the beam propagation theory in air space and through fiber, which is the fundamental for endoscope design and simulation. The second sub-section covers the fundamentals of Swept Source OCT (SSOCT) and key parameters. The third sub-section covers the fundamental of FLIM, including Time-Domain FLIM (TDFLIM) and Frequency-Domain FLIM (FDFLIM), and implementation methods.

2.1 Beam Propagation Theory

2.1.1 Gaussian Beam Optics

The Gaussian beam is a transverse electromagnetic (TEM) mode and the electric field is derived from paraxial Helmholtz equation [65]described by,

$$U(r) = A_0 \frac{W_0}{W(z)} \exp[-\frac{\rho^2}{W^2(z)}] \exp[-jkz - jk\frac{\rho^2}{2R(z)} + j\xi(z)] \quad \textbf{(1)}$$

where A_0 is amplitude, W_0 is waist radius, ρ is the lateral position ($\sqrt{x^2+y^2}$) on specific z position, and $\xi(z)$ is a phase retardation.

According to equation (1), the optical intensity is a function of the axial and radian distance,

$$I(\rho, z) = I_0[\frac{W_0}{W(z)}]^2 \exp[-\frac{2\rho^2}{W^2(z)}] \quad \textbf{(2)}$$

where $I_0 = |A_0|^2$. At each axial distance, the beam intensity drops from the beam axis to farther radial position. The beam radius at specific transverse plane is defined as the distance where the beam intensity drops to $1/e^2$ of the peak intensity on the beam axis, described by,

$$W(z) = W_0[1 + (\frac{z}{z_0})^2]^{1/2} \quad \textbf{(3)}$$

where the W_0 as the minimum beam radius in the transverse plane z=0. In both direction of beam, the beam radius increases and the distance between beam waist and the position where the beam radius grows to $\sqrt{2}$ of the beam waist is defined as Rayleigh Range. Depth of focus is defined as twice of the Rayleigh range z_0,

$$W_0 = (\frac{\lambda z_0}{\pi})^{1/2} \quad \textbf{(4)}$$

2.1.2 Beam Propagation through Air

Like ray optics, Gaussian beam will also be diverged or converged by lenses, but beam cannot focus to an infinite point. In the paraxial approximation of ray optics, ABCD matrix could relate the position and inclination of the beam transmitting though lens system. Similarly, ABCD matrix also was developed for Gaussian beam[65].

The Gaussian beam could be written as complex number q-parameter $q(z) = z + jz_0$, where z is the distance to the beam waist and z_0 is the Rayleigh range which is defined in equation (4). The matrix M of elements (A, B, C, D) in an arbitrary paraxial optical system could be used to converge or diverge Gaussian beam and the equation could be described by,

$$q_2 = \frac{Aq_1 + B}{Cq_1 + D} \quad \textbf{(5)}$$

A few groups used ABCD matrix to simulate the output of OCT endoscope [45-51], but ABCD matrix method was not applicable to circularly asymmetric. In addition, it cannot be applicable to the system with astigmatism occurring in side-viewing endoscope [50].

2.1.3 Fiber Optics and Beam Propagation Theory

An optical fiber is a dielectric waveguide to transmit light with very low loss[66]. The general fiber includes high-refractive-index core surrounding by low-refractive-index cladding. Refractive index profiles of common fiber are shown in the Figure 1. Modes are the possible solutions of the Helmholtz equation for waves representing certain unchanged amplitude distributions during propagation. They are derived from Maxwell's equations and the boundary conditions and the fundamental mode is Gaussian mode called LP01 mode. Main difference between SMF and MMF is quantity of modes transmitting through the fiber.

For step-index fiber design, if there is only one supported mode transmitting through the fiber, the fiber is called SMF. SMF should be confirmed with V-number below 2.405 according to the equation $V = \frac{2\pi}{\lambda} a\sqrt{n_{core}^2 - n_{clad}^2}$, where a is the radius of fiber core. On the contrary, multimode fiber has much higher V numbers, the number of supported modes is approximately calculated as $M \simeq \frac{V^2}{2}$ when V is very large. Between common SMF and MMF, some fibers have a few modes supported with V numbers varying between 2 to 20.

SMF's beam profile is close to Gaussian mode, and the mode radius can be calculated according to Marcuse's equation [67] $\frac{W}{a} \approx 0.65 + \frac{1.619}{V^{3/2}} + \frac{2.879}{V^6}$. However, the output beam profile from MMF is more complex because the output is the interference among all supported mode and it is not stable, because it also depends on light beam launching conditions, fiber bending conditions and so on.

Double-clad fiber is another type of optical fiber with three layers of optical material, core, the inner cladding and the outer cladding, shown in the Figure 1. Depending on refractive index

profile and application, there are two types of DCF and the DCF which is originally used for high power fiber amplifiers is useful for transmission of light and the fiber used for endoscope.

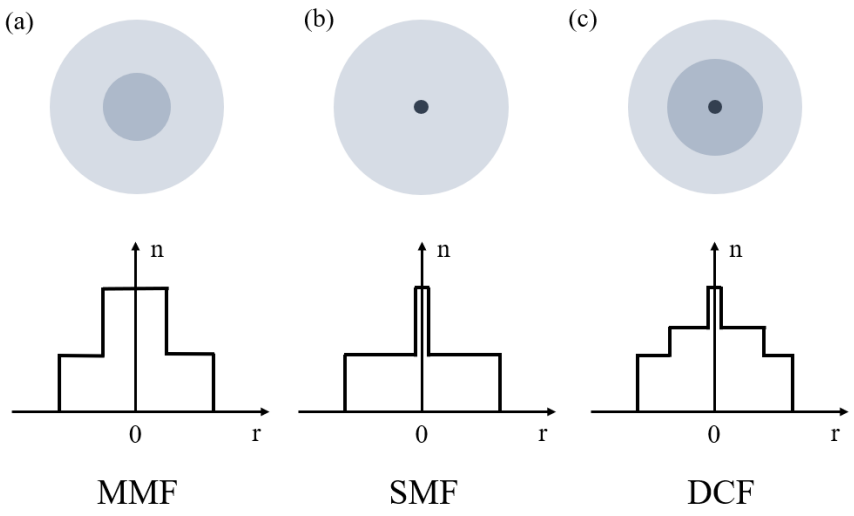

Figure 1. Refractive index profile of common fibers. (a) refractive index profile of multimode fiber (MMF) (b) refractive index profile of single mode fiber (SMF). (c) refractive index profile of double clad fiber (DCF).

2.2 Techniques of Frequency-Domain Optical Coherence Tomography

2.2.1 Theory of Optical Coherence Tomography

OCT is an imaging technique utilizing low-coherence interferometry for the depth-resolved reflectivity profiles of a sample. A generic OCT setup is shown in Figure 2. The laser could be super-luminescent diode and the detector is a spectrometer for Spectral-Domain OCT (SDOCT), or the laser is swept source laser and the detector is photo-detector for Swept Source OCT (SSOCT).

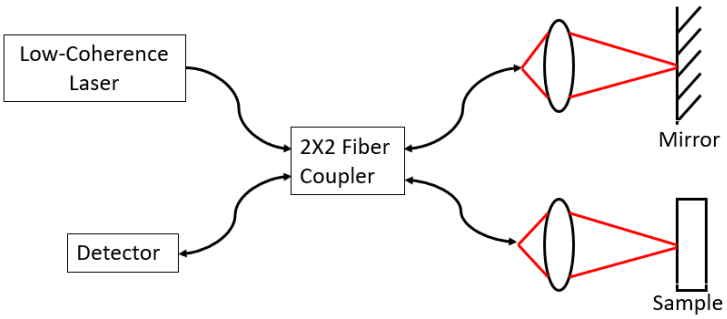

Figure 2. A generic schematic of FDOCT. Michelson interferometry design of a fiber-based OCT with low-coherence laser and detector.

In SSOCT, low-coherence laser is split to reference arm and sample arm implementing a simple Michelson interferometer. The coupler with different splitting ratio is used to split power with equal intensity or unequal intensity to reference arm and sample arm. Assuming the source spectrum is $I_i(k)$, where k is the spatial frequency, is split to reference arm and sample arm with 50:50 coupler which is independent on wavelength. The light in the reference arm collimated or focused on the mirror with high power reflectivity R_R, and then reflected back to the fiber coupler. The light in the sample arm focused on the sample with N discrete layers based on refractive index difference and reflectivity is $R_{s1}, R_{s2} \ldots R_{sn}$, where n is number of reflecting layers in the sample. The distance of the mirror surface from the fiber coupler (z_r) is same as the distance of the front surface from the fiber coupler (z_1), and physical distance of the sample's nth layer from the fiber coupler is z_n. The 50:50 coupler splits $I_i(k)$ combines beams from sample arm and reference arm, so the interference is given by,

$$I(k)=\frac{\rho}{4}\left[I_i(k)(R_R+R_{S1}+R_{S2}+...R_{Sn})\right] + \frac{\rho}{2}\left[I_i(k)\sum_{n=1}^{N}\sqrt{R_R R_{Sn}}\cos(2kn_r(z_R-z_{Sn}))\right] + \frac{\rho}{4}\left[I_i(k)\sum_{n\neq m=1}^{N}\sqrt{R_{Sn}R_{Sm}}\cos(2kn_r(z_{Sn}-z_{Sm}))\right] \quad (6)$$

where ρ is the responsivity of the detector (units Amperes/Watt), and the factor of 2 in the cosine terms reflects the round pathlength of light through the fiber coupler. There are three components in the equation above.

The first one is a pathlength-independent offset to the detector current, which is referred to as "DC" component. It is the main component of the detector current if the reference reflectivity (commonly ~1) dominates the sample reflectivity (on the order of ~10^{-4} to 10^{-5}). The second "cross-correlation" component is the desired component for OCT imaging, which depends on path difference between the reference arm and sample arm. The third "autocorrelation" term appear as artifacts in typical OCT imaging, but it is small compared to the DC and cross-correlation components.

To obtain the depth reflectivity profile in terms of z, an inverse Fourier transform of the linear interference signal is performed and described by

$$i(z)=\frac{\rho}{8}\left[\gamma(z)(R_R+R_{S1}+R_{S2}+...R_{Sn})\right] + \frac{\rho}{4}\left[\gamma(z)\otimes\sum_{n=1}^{N}\sqrt{R_R R_{Sn}}\delta(z\pm 2(z_R-z_{Sn}))\right] + \frac{\rho}{8}\left[\gamma(z)\otimes\sum_{n\neq m=1}^{N}\sqrt{R_{Sn}R_{Sm}}\delta(z\pm 2(z_{Sn}-z_{Sm}))\right] \quad (7)$$

The depth reflectivity profile is embedded in γ function which is the inverse Fourier transform of I(k). γ function is called the "coherence function", which dominates the axial point-

spread function (PSF). The FWHM of γ function defining the axial resolution of the depth reflectivity profile is coherence length of the laser $l_c = \frac{2\ln(2)}{n\pi}\frac{\lambda_0^2}{\Delta\lambda}$, where λ_0 is the center wavelength and $\Delta\lambda$ is FWHM of wavelength spectrum.

2.2.2 Figures of Merit

2.2.2.1 Resolution

As discussed in the previous section, the A-line represents the depth-resolved reflectivity profile of the sample at the focal point of the sample beam. With the scanning mechanism (rotation stage and pull back system for intravascular imaging system, or MEMS mirror), multiple A-scans are detected and assembled to 2D cross-section reflectivity map (B-scan) to show 3D volume of sample morphology details. For this reason, axial resolution and lateral resolutions are two important parameters in OCT imaging system.

The axial resolution is defined as FWHM of the axial PSF, which is determined by inverse Fourier transform of I(k). As an example, a Gaussian-shaped light source spectrum with FWHM of $\Delta\lambda$ and center wavelength λ_0, the axial resolution is determined the equation $l_c = \frac{2\ln(2)}{n\pi}\frac{\lambda_0^2}{\Delta\lambda}$.

Based on Rayleigh criterion, lateral resolution of the OCT imaging system is defined by FWHM of lateral PSF, and it is $\sqrt{2\ln(2)}$ times of beam waist radius assuming Gaussian beam at the sample.

2.2.2.2 Depth of Focus and Field of View

The other important parameter is depth of focus. Gaussian beam gradually grows “out of focus”, and the axial distance within which the beam radius lies within a factor $\sqrt{2}$ of its minimum value is knowns as the depth of focus or confocal parameter[65]. This range can be considered as

"in focus" and backscattered light from this range has practical usage. Depth of focus is twice the Rayleigh range $2z_0 = \frac{2\pi W_0^2}{\lambda}$.

The lateral field of view for OCT imaging system depends on the scanning system employed. For intravascular system, rotation stage could rotate the fiber around the arterial section, and pull back system could scan arterial section along the section.

2.2.2.3 Sensitivity Falloff and Maximum Imaging Depth

The theoretical deduction in section 2.2.2 illustrate the fundamental principle underlying SSOCT and SDOCT system. However, the instrumentation in practical has sampling issues.

The instrumentation always has limited spectral resolution, denoted by $\delta_r k$. In SSOCT $\delta_r k$ is limited by the instantaneous line shape of the laser and defined as FWHM spectral resolution. The detected interference signal is a convolution of the ideal spectral interferogram with a Gaussian function with FWHM of $\delta_r k$, which leads to falloff on A-scan data equaling to half of the coherence length $\hat{z}_{6dB} = \frac{\ln(2)}{n\pi}\frac{\lambda_0^2}{\Delta\lambda}$.

Also, FDOVT data processed by the computer and it involves sampling that spectral interferogram which means the sampling rate in SSOCT. The maximum and minimum depth samples is defined by the Nyquist criterion $z_{\max} = \frac{\lambda_0^2}{4 \bullet \delta_s \lambda}$.

2.3 Techniques of Fluorescence Lifetime Imaging

2.3.1 Basic Principle

Fluorescence is the emission of light by a molecule which absorbs light or other electromagnetic radiation[68]. The Jablonski diagram is an energy diagram shown in Figure 3,

used to illustrated various molecular processes for fluorescence. Each column represents a specific spin multiplicity. Typical Jablonski diagram only includes electronic energy level which is a specific column, and multiple vibrational level within each electronic energy which is a specific line in each column, omitting other details such as rotational levels. Bold lines represent the limits of electronic energy levels. The ground electronic energy level is S0, and the first excited electronic energy level is S1. Absorption is the process which an electron is excited from a lower energy level to a higher energy level, which is a very fast transition on the order of 10^{-15} seconds. Due to Boltzmann distribution of electrons within low energy levels, absorption usually occur from the S0 to higher electronic energy level.

On the contrary, excited states are not stable and electrons return to the lower state in the same multiplicity manifold, which is called fluorescence. Fluorescence is a slow process on the order of 10^{-9} to 10^{-7} second. The energy of the photon emitted in fluorescence is the same energy as the difference between two energies, $E = h\nu = E_m - E_n$, where h is the Planck's constant and v is the frequency of the photon, E is the energy of the specific energy level. Fluorescence energy of the photon is always less than that of the exciting photons, because energy is also lost in internal conversion and vibrational relaxation, which are non-radiative processes. Internal conversion represents a transition from a vibrational level in on electronic level to another vibrational level in a lower electronic level if vibrational energy level overlaps electronic energy level. Vibrational relaxation is the transition from a higher vibrational level to lower vibrational level in the same electronic level.

Phosphorescence process is slow process on the order of 10^{-4} to 10^{-1} seconds from an excited triplet state to a singlet ground state. It is after the slowest process called intersystem crossing, the transition from an excited singlet state to an excited triplet state.

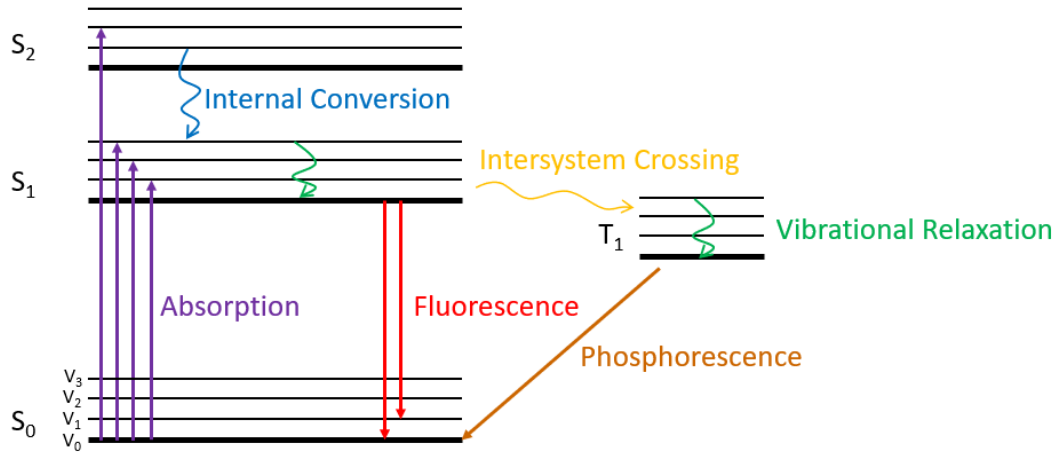

Figure 3. A Jablonski's diagram showing the process of fluorescence. S0 is the ground state, S1 and S2 are excited states, and T1 is an excited triplet state. Each column represents an electronic energy level. The bold lines represent the lowest vibrational energy level of the electronic energy level, and the thin lines represent rest of the vibrational energy levels. Purple arrows represent the absorption, red arrows represent the fluorescence, blue curved blue arrows represent internal conversion and curved green arrows represent vibrational relaxation, curved yellow arrows represents intersystem crossing, and brown arrows represent phosphorescence.

The lifetime of the fluorophore in the absence of non-radiative process is called intrinsic lifetime $\tau_n = \frac{1}{\Gamma}$ and the simplest case of a fluorescence decay follows a mono-exponential function. Suppose a sample containing the fluorophore is excited with an infinitely sharp pulse of light, and the excited-state population decays with a rate of $\Gamma + k_{nr}$ according to $\frac{dn(t)}{dt} = (\Gamma + k_{nr})n(t)$, where n(t) is the number of excited molecules at time t, and k_{nr} is the non-

radiative decay rate. The equation can be written in terms of the time-dependent intensity I(t), $I(t) = I_0 \exp(-t/\tau)$ where lifetime $\tau = (\Gamma + k_{nr})^{-1}$. The lifetime is the average amount of time fluorophores remain in the excited state excitation and for multi-exponential decay, the lifetime can be calculated as

$$< t >= \frac{\int_0^\infty tI(t)dt}{\int_0^\infty I(t)dt} \quad \textbf{(8)}$$

2.3.2 Time-Resolved Fluorescence Measurements

Time resolved measurement is used to measure intensity decays and steady-state measurement is an average of the time-resolved intensity. In cellular imaging using fluorescence measurement, the overlap of the emission from different fluorophore is difficult to be resolved from the steady-state result, but lifetimes are typically independent of the probe concentration. There are two methods for time-resolved fluorescence, time-domain and frequency-domain method.

As shown in Figure 4 (a), the excitation is a short pulse and the emission decays as a function of time in time-domain measurement. The lifetime can be calculated from the slope of a plot of log I(t). In frequency-domain measurement shown in Figure 4 (b), the excitation is an intensity-modulated light at a high frequency on the order of 10MHz to 100Mhz, and its reciprocal is comparable to the decay time of fluorescence. The emission is also intensity modulated at the same frequency with a phase shift. The ratio B/A and b/a represent the modulation of the emission and excitation respectively, and modulation is $m = \frac{B/A}{b/a}$ which is actually a demodulation factor. The lifetime can be calculated with the phase angle $\tau_\varphi = \omega^{-1} \tan\varphi$ and the modulation

$\tau_m = \frac{1}{\omega}[\frac{1}{m^2} - 1]^{1/2}$. For complex samples which have several lifetime components, a range of excitation modulation frequencies should be implemented for lifetime measurement.

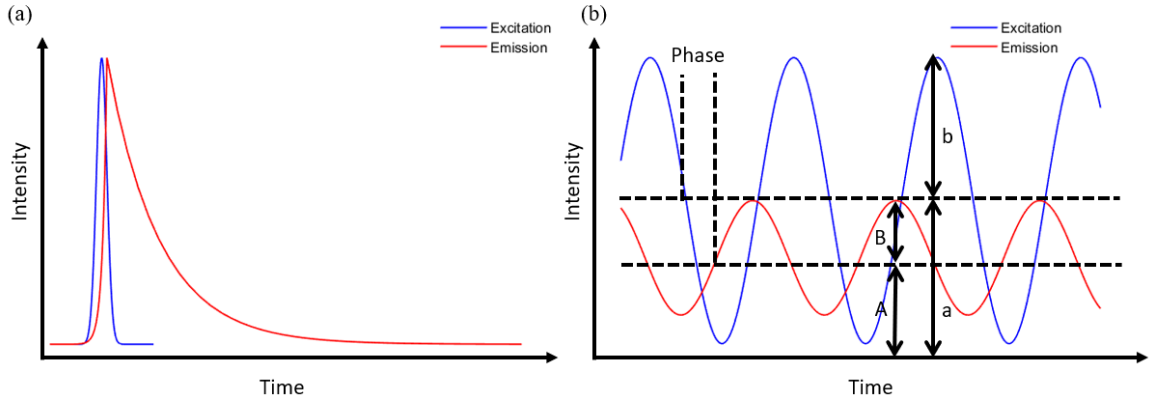

Figure 4. Time-resolved measurement methods. (a) Time-domain FLIM is excited by a sharp pulse and fluorescence decay is used for lifetime calculation. (b) Frequency-domain FLIM is excited by intensity-modulated light and phase angle and modulation are used for lifetime calculation.

2.3.3 Optical Configuration

For cellular tissue measurement, detected emission includes emission from all the fluorophores in the FOV, and in order to differentiate fluorescence from different fluorophore, the FLIM system are implemented with a few emission channels with a set of dichroic mirrors and filters in emission channel, shown in Figure 5. The specific channel bandwidths are chosen according to specific sample and applications.

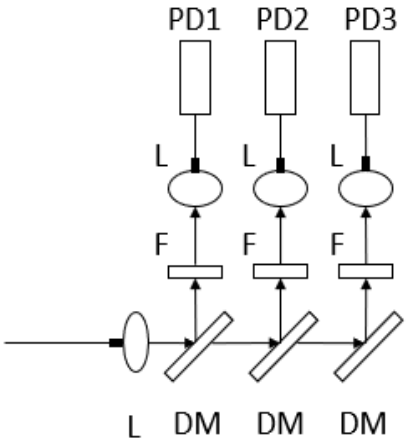

Figure 5. Basic schematic of the setup for multi channels. Emission is transmitting through the fiber to the lens. L: collimation and coupling lenses, DM dichroic mirrors, F: bandpass filters, PD: Detector not limited to APD or PMT

In this project, artery was imaged using the TDFLIM or FDFLIM system separately. The main auto-fluorophores in artery are collagen, LDL and elastin. Collagen has peak emission wavelength at 390nm, but peaks for two elastin and LDL overlap at 425 nm and the spectrum shape is also very similar. However, LDL lifetime is much higher than that of elastin since 450nm, which could be used to differentiate both. The first wavelength is chosen at ~390nm for collagen, the second and the third channels were chosen at ~450nm (same intensity and similar lifetime for LDL and elastin) and ~550nm (same intensity for LDL and elastin but higher lifetime of LDL).

3. BALL LENS-BASED ENDOSCOPE DESIGN AND FABRICATION

This chapter explains a general fabrication method for ball lens-based endoscopes based on SMF, MMF, or DCF. The type of fiber, ball lens shape and the fabrication details are different for different applications, and would be explained in details in the respective chapters.

3.1 Design of Ball Lens-Based Endoscope

A fiber preparation and splice workstation (FFS2000, Vytran) was used for endoscope fabrication. The 1.55-meter endoscope was constructed starting with a specific fiber, including SMF, MMF or DCF. The fiber was fusion spliced to a coreless fiber (CLF), which is solid pure fused silica rod with an acrylate coating like common fiber. Following splicing, the CLF was cleaved to a precise length, heated and shaped into an ellipsoid ball with predetermined semi-principal axes in the tungsten filament furnace of the workstation. The ellipsoidal shape was designed to compensate for the astigmatism caused by the toroidal shape of the catheter sheath and the silica tube used to cover and protect the fiber endoscope. The distal ball lens was polished with an angle of 41° using a commercial fiber polisher (69-3000-160, Buehler) with custom modifications to enable ball lens polishing at precise angles for side viewing endoscopes. The 41° angle was chosen so that total internal reflection (TIR) would occur at the polished glass-air interface, hence obviating the need for reflective coatings on the polished surface. In addition to the angle, precise control of the polishing depth from unpolished ball is necessary in order to achieve good performance. The schematic ball lens-based endoscope is illustrated in Figure 6.

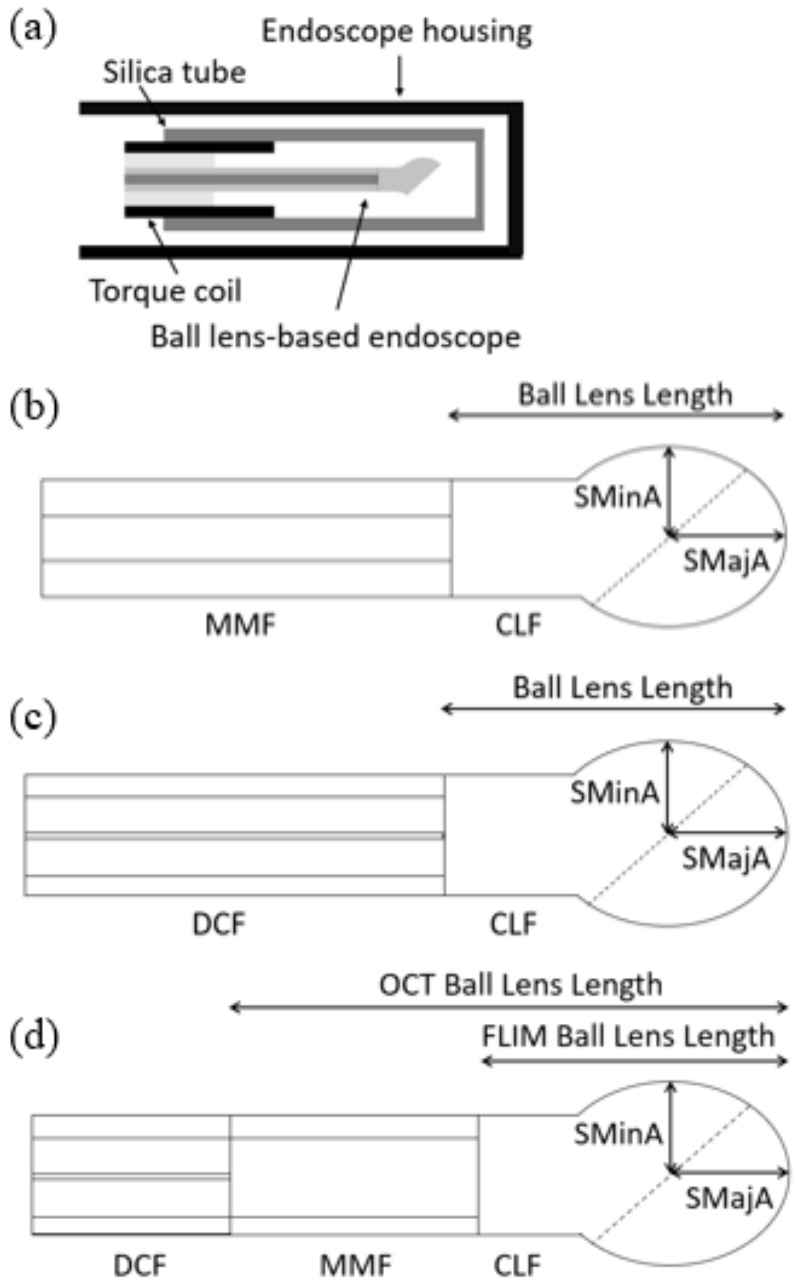

Figure 6. Schematic drawing of the ball lens-based endoscope. (a) Schematic drawing of the catheter. Heated and shaped CLF fusion spliced to a stripped fiber, and the fiber was glued with torque coil and silica tube. Torque Coil's ID is 270 μm and OD is 450 μm. Silica Tube's ID is 530 μm and OD is 620 μm. (b) Ball lens-based endoscope design based on MMF for TDFLIM, dashed line indicates polishing surface. MMF: multimode fiber, CLF: coreless fiber, SMajA: semi-major axis, SMinA: semi-minor axis. (c) Ball lens-based endoscope design based on DCF for FDFLIM. (d) Ball lens-based endoscope design based on DCF for OCT/FLIM.

3.2 Ball Lens Heating Process

FFS2000 system is designed to fusion splice two pieces of fibers with high coupling efficiency. The fusion splice process was controlled by 8 parameters shown in Figure 7 except Argon flow rate, which are default values for fiber with 125um cladding diameter. Default values are good parameters to fusion splice CLF with SMF, MMF and DCF.

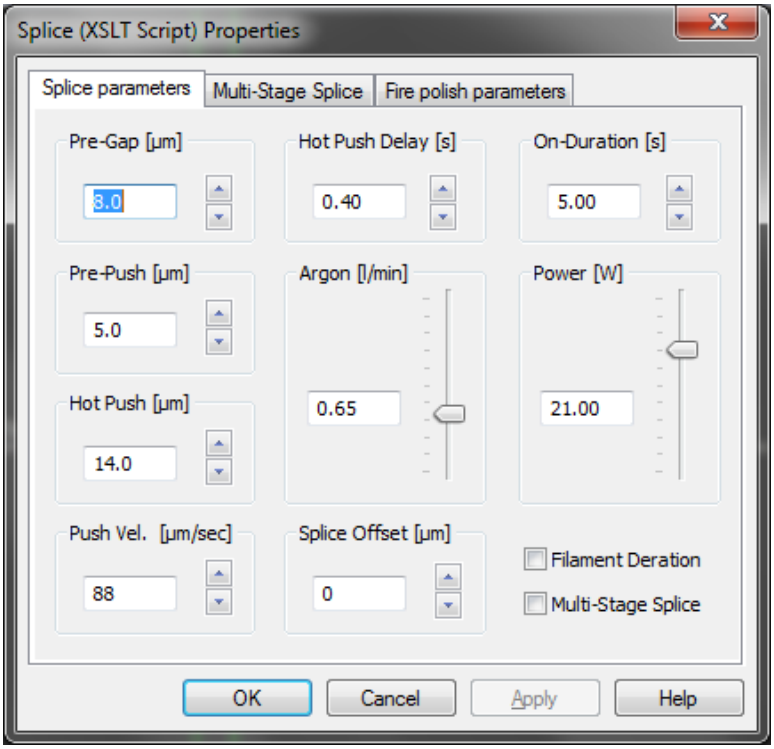

Figure 7. Vytran FFS2000 fusion splice parameters in Splice Properties. Values are default values for SMF (SMF-28e, Corning).

CLF was cleaved to a precise length, and aligned with another CLF automatically by FFS2000. CLF piece would be only fiber inserted into heating chamber at pre-calculated location to be heated to ball lens and the fusion splice parameters need to be researched on. The other piece of fiber need to be moved out to avoid interference with the CLF. Besides 8 parameters to be adjusted for specific ball lens shape indicated in Figure 7, there is another parameter used to tune

best shape defined as relative position between heating chamber and the fiber to be heated. After removing the fiber, the fusion splice head was moved closer to CLF, which is used to control the relative position between heating chamber and the fiber to be heated. After adjusting each parameter by single-variable experiment, we found heating power, duration, and heated length of coreless fiber inside heating chamber had the highest impact on ball size and the relationship between parameters and semi-principal axes are linear.

$$\text{Semi-Major Axis} = 0.20 \times P + 119.0 \quad (9)$$

$$\text{Semi-Minor Axis} = 5.40 \times P - 37.9 \quad (10)$$

$$\text{Semi-Major Axis} = 0.12 \times T + 79.4 \quad (11)$$

$$\text{Semi-Minor Axis} = -0.01 \times T - 37.9 \quad (12)$$

$$\text{Semi-Major Axis} = 4.85 \times L + 123.4 \quad (13)$$

$$\text{Semi-Minor Axis} = 43.86 \times L + 94.6 \quad (14)$$

where Semi-Major Axis and Semi-Minor Axis denote fitted ellipsoidal ball lens semi-principal axis's length in μm shown in **Figure 6**, P denotes heating power in W indicated in Splice Properties shown in Figure 7, T denotes on-duration while heating in seconds indicated in Splice Properties shown in Figure 7, and L denotes the length of coreless fiber to be pushed into heating area in μm adjusted by Splice Head position shown in Figure 8.

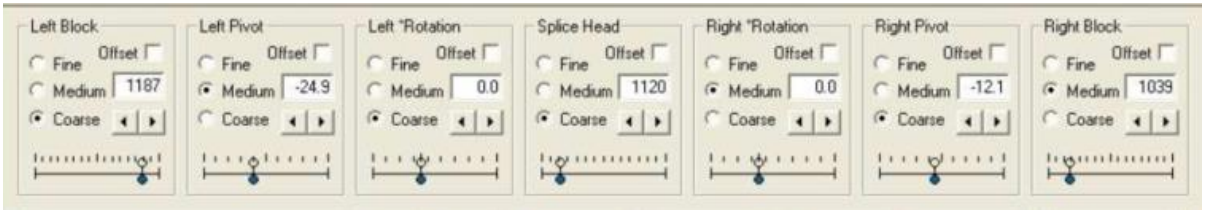

Figure 8. Vytran FFS2000 graphic user interface. Left block and right block control the left fiber and right fiber position, left pivot and right pivot are used to align two fibers, left rotation and right rotation are used to rotate two fibers, and splice head is used to move splice head position.

3.3 Customized Fiber Polishing Machine

After heating the CLF to ball lens, the distal tip was polished with an angle of 41° using a commercial fiber polisher (69-3000-160, Buehler) with custom modifications to enable ball lens polishing at precise angles for side viewing endoscopes. The 41° angle was chosen so that total internal reflection (TIR) would occur at the polished glass-air interface, hence obviating the need for reflective coatings on the polished surface. In addition to the angle, precise control of the polishing depth from unpolished ball is necessary in order to achieve good performance. The polishing holder is designed and fabricated to hold the fiber for polishing with vacuum shown in Figure 9. It was fabricated with aluminum and insert was fabricated with graphite to hold fiber ball lens securely but avoid damage on ball lens and fiber. The main part and insert were fabricated with groove, the shape and depth were designed for fiber diameter and ball lens size.

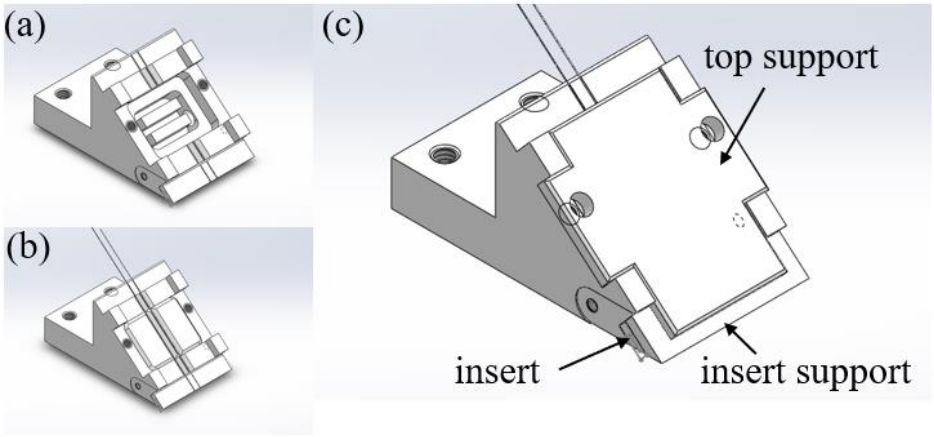

Figure 9. Polishing holder assembly. (a) polishing holder main part, it has two through holes to connect with Buehler polisher, and a cavity for vacuum system. (b) polishing holder support and insert (graphite) connected with main part. (c) top support and insert support connect with holder and securely hold the fiber.

3.4 Endoscope Accessories and Housing

The fiber endoscope was then enclosed in a customized torque coil (ASAHI INTECC) with high-speed torque transmission and high flexibility. The OD of the torque coil is 450 μm and the ID is 270 μm. The proximal end was connectorized with a custom FC/APC connector and strain relief boot, mating to a custom broadband fiber optic rotary joint [69]. The distal end was covered by a laser-cut silica tube (TSP530620, Polymicro) with an outer diameter of 620 μm and an inner diameter of 530 μm, shown in Figure 10. The silica tube serves both to protect the ball lens and preserve the air-glass interface at both the flat polished and curved surfaces of the endoscope even when submerged. The ID of silica tube was chosen so that the torque coil could fit inside and therefore make a strong bond between the two items. Using a smaller diameter for the silica tube would unnecessarily increase the astigmatism introduced by the tube.

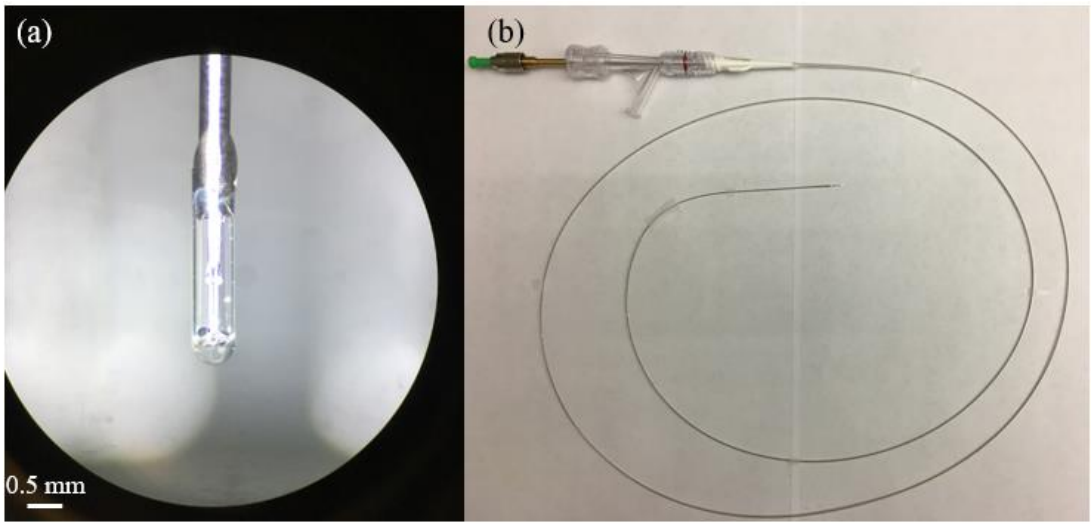

Figure 10. Ball lens-based endoscope images. (a) Ball lens enclosed within silica tube, and both ends of silica tube were sealed by glue. Scale bar: 0.5 mm (b) Endoscope enclosed inside catheter housing, the endoscope proximal end was connectorized by fiber connector.

A customized two-layer torque coil (ASAHI INTECC) has two layers of stainless steel, and the inner layer is right-hand wound direction and the outer layer is left-hand wound direction. For this reason, the torque coil can be rotated to only one direction to transmit torque, and the torque cannot be uniformly transmitted while rotating to the other direction. The fiber endoscope was glued with torque coil in endoscope distal end while maintaining 1 mm fiber out of the torque coil.

After glue curing after 12 hours, the endoscope proximal end and fiber connector were glued and connectorized with fiber connecter. The brass adaptor was designed and fabricated to connect fiber, torque coil and connector so that the torque could be transmitted from connector to endoscope distal end through torque coil. The adaptor was also designed to relieve strain between connector and fiber. The relative positions between each component were important to improve the coupling efficiency and reliability, and they were indicated in Figure 11.

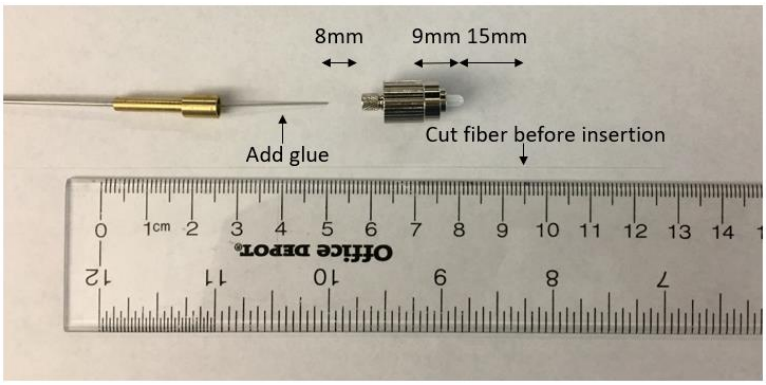

Figure 11. Fiber connectorization

3.5 Endoscope Sterilization

All invasive biomedical products should be properly sterilized to avoid transmission of microorganism [70, 71]. The endoscope which enters sterile tissue must be sterile by one of sterilization method, including but not limited to dry heat sterilization, steam striation, ethylene oxide (EtO) sterilization and radiation sterilization. A proper sterilization should be decided based

on biomedical instrument to be sterilized and a summary of common sterilization are summarized in Table 1 [70, 71].

Table 1. Advantages and disadvantages of sterilization methods

	Efficacy	Safety	Compatibility
Dry heat	Slow	Nontoxic to patient, staff and environment	Incompatible for heat-sensitive components (plastic and glue)
Steam	Fast	Nontoxic to patient, staff and environment	Incompatible for heat-sensitive or humid-sensitive components (plastic and glue)
Radiation	Fast	Carcinogenic	May cause components properties changes
EtO sterilization	Slow	Toxic, carcinogenic, flammable and explosive	Compatible with most components

EtO sterilization was chosen for endoscope sterilization in the application. EtO is an alkylating agent to disrupting microorganism DNA and is used for endoscope and multi-lumen tubing products. The whole process is at low temperature, compatible with plastic and other components which cannot withstand the heat. The endoscope includes different type of plastic and glue properties of which may change with high temperature or radiation. The endoscope was properly cleaned, packaged, and then EtO sterilized for in-vivo experiment.

4. BALL LENS-BASED INTRAVASCULAR TIME-DOMAIN FLUORESECENCE LIFETIME IMAGING MICROSCOPY ENDOSCOPE

This chapter explains a combined simulation, fabrication, and measurement method for ball lens-based endoscope based on multimode fiber and applied to intravascular time-domain fluorescence lifetime imaging microscope. Simulation is important to minimize manufacturing time by establishing a preferred shape for the partial ellipsoid lens before optimizing the manufacturing process. It also allows us, in conjunction with optical performance characterization techniques, to predict the performance of any given endoscope in the intravascular environment. Simulations of the endoscope's optical properties was done using a Super-Gaussian intensity profile in the optical design program, Zemax. A stable Super-Gaussian light source was developed for testing by carefully controlling the launch angle into a multimode fiber and the bend induced mode mixing. Using these techniques, a ball lens endoscope based on a 50 μm core multimode fiber was developed. The measured and simulated full width at half maximum over approximately the first 2 mm of beam propagation from the lens shows good agreement with RMS errors of 9.71 μm and 10.66 μm for the two orthogonal planes. The endoscope is demonstrated for fluorescence lifetime imaging by measuring fluorescence standards as well as fresh ex vivo human coronary arteries.

4.1 Materials and Methods

4.1.1 Simulation and Validation of Ball Lens-Based Endoscope Illumination Performance

We set out to simulate the performance of the endoscope via the optical ray-tracing program OpticStudio (Zemax), in order to optimize the ball lens design prior to manufacture. We quickly realized that while a few groups had constructed endoscopes starting with multimode fiber, there was no standard method to simulate or measure their performance. Simulation is important

to minimize manufacturing time by establishing a preferred shape for the partial ellipsoid lens before the manufacturing process. It also allows us, in conjunction with optical performance characterization techniques, to predict the performance of any given endoscope in the intravascular environment. The major impediment to establishing standard simulation and measurement protocols is the mixing of spatial modes within the multimode fiber leading to rapid variations in the intensity profile exiting the fiber.

In order to overcome this issue, we sought to identify an intensity profile that could be modeled in OpticStudio as well as reliably generated and measured using standard optical techniques. We chose the Super-Gaussian[72, 73] profile which approximates a top-hat profile with Gaussian tails on either side. The intensity profile is $I(r) = I_0 exp\left[-2\left(r / w_m\right)^n\right]$, where r is the radial dimension, w_m is the beam waist, and n is the order of the Super-Gaussian.

We developed the following methodology to reliably measure and manipulate the intensity profile to be approximately Super-Gaussian. We took several actions to insure a repeatable and stable output beam intensity distribution from the multimode fiber. A 488 nm laser (iBeam smart PT 488, Toptica) was focused into one end of multimode fiber (MMF) patch cable with a variable launch angle. The fiber was wrapped around a Ø1/2" standard optical post to extinguish the cladding mode and mix spatial modes. The other end of the patch cable was connected with the endoscope or a 2nd patch cable by a mating sleeve. Using the 2nd patch cable the intensity was tuned to a Super-Gaussian by adjusting the launch angle into the MMF. The camera was set to a relatively long integration time, e.g. 750 ms, in order to average over fluctuations in spatial mode structure. Once aligned, this experimental setup yielded repeatable and stable intensity profiles

even when adjusting laser output power either electronically or with an ND filter or changing out the 2nd patch cable.

The camera setup noted above consisted of a CMOS camera (MCE-B013-US) with a 5.2 μm pixel pitch and an objective lens (M-20X, Newport) with NA of 0.40. The system had an optical resolution of 2.76 μm and a spatial sampling of 1.37 μm as determined by imaging a 1951 USAF resolution test chart. The camera assembly was mounted on a translation stage and positioned perpendicular to the output of the fiber endoscope so that irradiance could be measured at several distances along the optical axis.

The output of the catheter was modeled in the following way. We rendered the ellipsoidal ball-lens using Solidworks and imported it into OpticStudio. The refractive index of the MMF and coreless fiber (CLF) was assumed to be unchanged during the manufacturing process with a value of n=1.463. The intensity profile impinging on the CLF was modeled based on the source_radial using non-sequential mode with OpticStudio. The angular distribution was based on the Super-Gaussian fitting of a series of far field measurements of beam profile from a cleaved fiber as detailed below.

4.1.2 Simulation of Ball Lens Endoscope Collection Performance

The collection efficiency is a critical aspect of a FLIM system, hence an important parameter to be considered for ball lens design. We simulated collection performance of the endoscope in a similar way as illumination. This allows us to make comparisons and rational decisions concerning trade-offs between collection and illumination performance.

Source and detector relative positions were swapped in the simulation of collection (relative to illumination). This was done instead of directly modeling fluorescence due to the limitations of Professional version of OpticStudio. The fluorescence profile from a specified

position was modeled based on the source_point, assuming the fluorescence as isotropic, radiating energy equally in all directions[72]. One detector was placed at the proximal end of the fiber to detect the percentage of fluorescence collected by the ball lens. The collection efficiency map was drawn by adjusting the source position within one specified area. The collection efficiency of the system is calculated by integrating the multiplication of simulated illumination beam profile and collection efficiency map.

4.1.3 Design of Ball Lens Endoscope

A fiber preparation and splice workstation (FFS2000, Vytran) was used for endoscope fabrication. The 1.55-meter FLIM endoscope was constructed starting with a 50 μm core MMF (FG050UGA, Thorlabs) with an NA of 0.22. The MMF was fusion spliced to a CLF (HCF-125-47, Coractive) with a coupling efficiency of >99%. Following splicing, the CLF was cleaved to a precise length, heated and shaped into an ellipsoid ball with predetermined semi-principal axes in the tungsten filament furnace of the workstation, shown in Figure 12. The ellipsoidal shape was designed to compensate for the astigmatism caused by the toroidal shape of the catheter sheath and the silica tube used to cover and protect the fiber endoscope. The distal ball lens was polished with an angle of 41° using a commercial fiber polisher (69-3000-160, Buehler) with custom modifications to enable ball lens polishing at precise angles for side viewing endoscopes. The 41° angle was chosen so that total internal reflection (TIR) would occur at the polished glass-air interface, hence obviating the need for reflective coatings on the polished surface. In addition to the angle, precise control of the polishing depth from unpolished ball is necessary in order to achieve good performance.

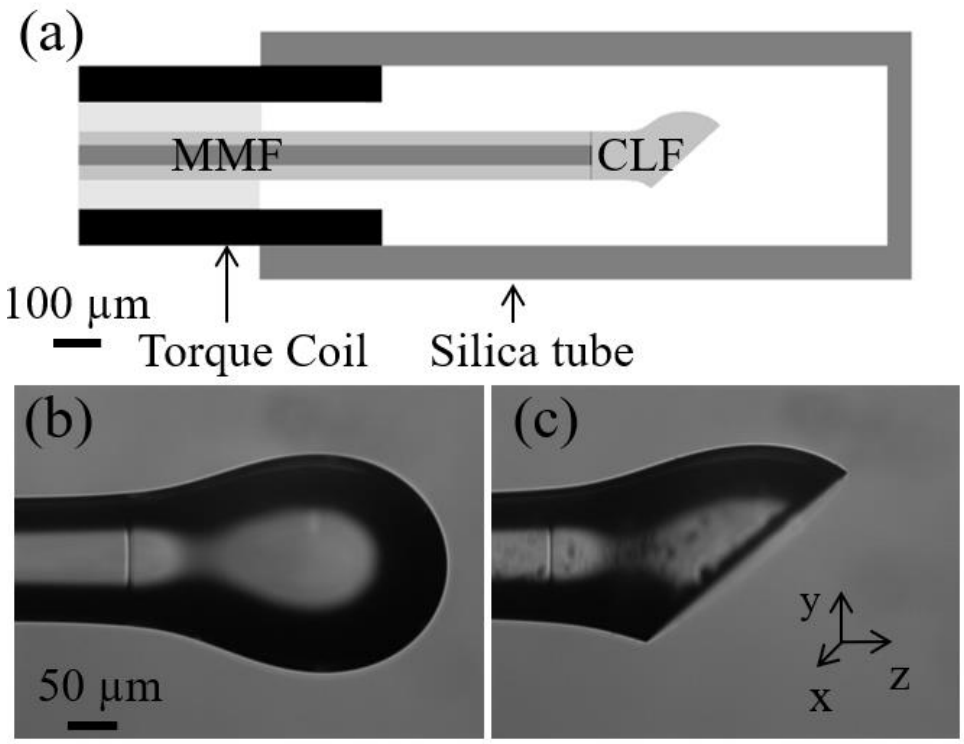

Figure 12. Schematic drawing of TDFLIM endoscope. (a): Schematic drawing of the catheter. Heated and shaped CLF fusion spliced to a stripped MMF, and the fiber was glued with torque coil and silica tube. Torque Coil's ID is 270 μm and OD is 450 μm. Silica Tube's ID is 530 μm and OD is 620 μm. Scale bar: 100 μm. MMF: multimode fiber. CLF: coreless fiber. (b): Side view of the fabricated ball lens before polishing. Heated and shaped CLF fusion spliced to a MMF. Scale bar: 50 μm. c: Side view of the ball lens after polishing by customized fiber polishers. The polishing angle is 41°.

The fiber endoscope was then enclosed in a customized torque coil (ASAHI INTECC) with high-speed torque transmission and high flexibility. The OD of the torque coil is 450 μm and the ID is 270 μm. The proximal end was connectorized with a custom FC/APC connector and strain relief boot, mating to a custom broadband fiber optic rotary joint [69]. The distal end was covered by a laser-cut silica tube (TSP530620, Polymicro) with an outer diameter of 620 μm and an inner diameter of 530 μm, shown in Figure 13. The silica tube serves both to protect the ball lens and preserve the air-glass interface at both the flat polished and curved surfaces of the endoscope even

when submerged. The ID of silica tube was chosen so that the torque coil could fit inside and therefore make a strong bond between the two. Using a smaller diameter for the silica tube would unnecessarily increase the astigmatism introduced by the tube.

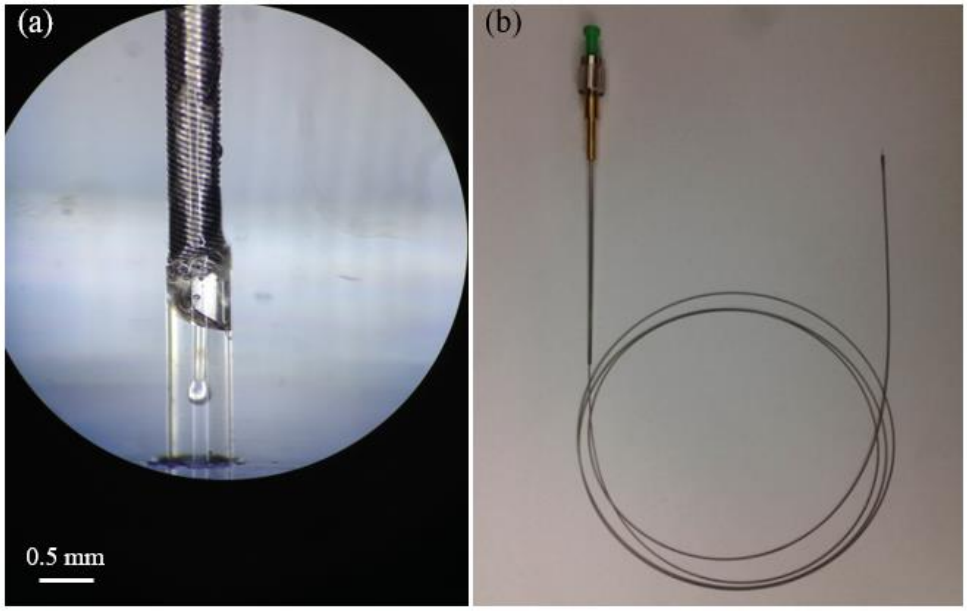

Figure 13. TDFLIM catheter's images. a: Ball lens enclosed within silica tube, and both ends of silica tube were sealed by glue. Scale bar: 0.5 mm b: Image of FLIM catheter, the proximal end was connectorized by FC/APC connector.

4.1.3 FLIM Instrumentation

The endoscope was attached via an ultra-broadband lensless fiber optic rotary joint[69] to a high-speed multispectral FLIM imaging system based largely on the design discussed in articles [27, 73]. The lensless rotary joint achieved very low insertion loss (less than 0.2 dB) even at high rotational velocity (8800 revolution per minute, rpm). The time-domain FLIM system utilized an actively Q-switched diode pumped solid state laser (SPOT 10-100-355, Elforlight) as the excitation source (355 nm, 40 kHz max repetition rate, <1.5 ns pulse width). The laser excitation was transmitted via a dichroic mirror (365DCLP, Chroma Technology) into the rotary joint and

endoscope. The fluorescence emission returning from the endoscope was separated from the excitation by the dichroic mirror and then further separated into two channels (Ch1 390/40 nm and Ch2 494/41 nm) using a set of dichroic mirrors and filters (Chroma Technology and Semrock). Each channel was launched into a fiber with different lengths (1 m, 50 m) chosen to provide a time interval between two channels. The 390/40 nm and 494/41 nm channels were coupled into the 43 m and 1 m fibers, respectively, to maximize dynamic range as the fluorescence was weaker in the 494/41 nm channel. The relatively long delay was used to temporally separate background fluorescence due to the optical fiber in the 390/40 nm channel from the fluorescence at the sample position in the 494/41 nm channel. The two consecutive decays were detected with a MCP-PMT with rise time of 160 ps (R3809U-50, Hamamatsu Photonics), and sampled with at 4 GS/s with a 1-channel 8-bit digitizer (GaGe CobraMax CS14G8). The energy of the incident light on the sample was maintained below 1.6 μJ/pulse (below the ANSI maximum permissible exposure for skin[74] considering single-pulse limit and average-power limit).

The time resolved fluorescence measurements were processed by first subtracting the optical-fluorescence background, and then deconvolving using an iterative nonlinear least squares exponential model as described previously[75]. A bi-exponential model was used when deconvolving tissue fluorescence, and a mono-exponential model was used when processing exogenous fluorescence. Optical-fluorescence background for both tissue and exogenous data was obtained by spatial averaging at least 100 pixels in a blank area of the image for each PMT gain. The blank area consisted of an area with no object at the sample position. Spatial averaging was performed to increase signal quality for both exogenous fluorophore and tissue images. A total of 8 longitudinal pixels were averaged for exogenous fluorophore images, 2 longitudinal pixels were averaged for tissue images, and no averaging was performed for air force chart images. The

absolute intensity images were obtained by integrating the observed fluorescence decays for each emission channel after subtracting the background. The normalized intensity image for a given channel and pixel was calculated as the absolute intensity of the channel divided by the sum of the absolute intensities across all channels at the given pixel. Spectral calibration was applied to the absolute intensity images by multiplying each emission channel by a predetermined scaling factor before computing the normalized intensity images. The goal of spectral calibration was to correct for optical loss in each channel that was not due to the dichroic mirrors (DM) and bandpass filters (BPF). POPOP was used as a reference to compute the calibration factors. First, POPOP was imaged with a spectrometer (PC1, ISS) to obtain a reference spectrum. The expected fluorescence spectrum measured by the endoscope for each emission channel was calculated by multiplying the reference spectrum by the DM and BPF transmission spectra for the given emission channel. The expected fluorescence ratios were calculated as the ratios of the integrated expected fluorescence spectra between each channel. POPOP was then imaged with the endoscope system to obtain the system fluorescence. The system fluorescence ratios were calculated as the ratios of the absolute intensities between each emission channel. The spectral calibration factors were computed to make the system fluorescence ratios equal to the expected fluorescence ratios. Subsequent images were spectrally corrected using these scaling factors. Three standard fluorophores with known emission spectra and lifetimes were selected to evaluate the FLIM system, POPOP in ethanol (emission peak 390 nm, reported lifetime 1.38±0.01 ns)[76], NADH is PBS (emission peak 450nm, reported lifetime 0.44 ns)[77], and FAD in PBS (emission peak 540 nm, reported lifetime 2.07 ns)[78]. The fluorophore concentrations (0.1 mM in POPOP, 1 mM in NADH, and 1 mM in FAD) were chosen such that the peak emission intensity from each fluorophore was comparable[79]. Each dye was loaded into a quartz cuvette and placed adjacent to the catheter prior to being imaged. Dyes were

imaged individually so that the PMT gain could be set to optimize the dynamic range and saturation.

4.1.4 Tissue Preparation and Imaging

Human coronary artery segments were obtained from autopsy cases within 5 days of the time of death, according to a protocol approved by the Texas A&M University Institutional Review Board. The arterial segment was imaged by placing the endoscope inside the lumen of the artery performing a pullback. Immediately after imaging, each segment was ink marked for correlation with histopathology, fixed in 10% formalin, and sent for histopathology analysis. Each image plaque segment was consecutively sectioned every 1 mm. The sections were stained with Movat pentachrome and evaluated by a cardiovascular pathologist.

4.2 Results and Discussion

4.2.1 Endoscope Simulation, Fabrication and Validation

In order to validate the performance of the developed intravascular FLIM system, measurements and simulations were completed on the optical and mechanical functionality. These tests included measures of optical throughput and resolution, mechanical function for the rotation and pull back uniformity and stability, as well as measurement of fluorescence intensity and lifetime of fluorescence standards.

The endoscope test bench was setup as noted above. In order to verify the stability and repeatability of the results, measurements were taken initially from a cleaved fiber. The camera assembly was placed with its optical axis parallel to the optical axis of the laser emission from the fiber. Measurements were made at five positions along the optical axis with an interval of 508 μm. Between measurements, the fiber was removed and replaced to ascertain the repeatability. A representative profile at each interval is shown in Figure 14. The solid black lines are the Super-

Gaussian fits for the respective profile. The mean and standard deviation of the full width at half maximum at each interval for n=9 measurements per interval was 48.1±0.48 μm, 146.8±0.91 μm, 255.1 ±1.03 μm, 300.1±3.03 μm, and 453.6±2.77 μm, measured over a 2 mm interval. NA of 0.09 for the diverging beam was fitted through half width at 5% maximum of generated beam profiles at different positions. Note this is different from the specified fiber NA because we do not populate all of the spatial modes. The stability of the Super-Gaussian output gave us confidence that we could expect a similar intensity profile at the interface of the coreless fiber and the multimode fiber. In order to generate the Super-Gaussian, a portion of the spatial modes of the fiber are populated, likely different from what will be populated in a typical intravascular imaging application. Hence, the resolution results derived from this intensity distribution can be considered an approximation to what will be achieved in an intravascular imaging experiment.

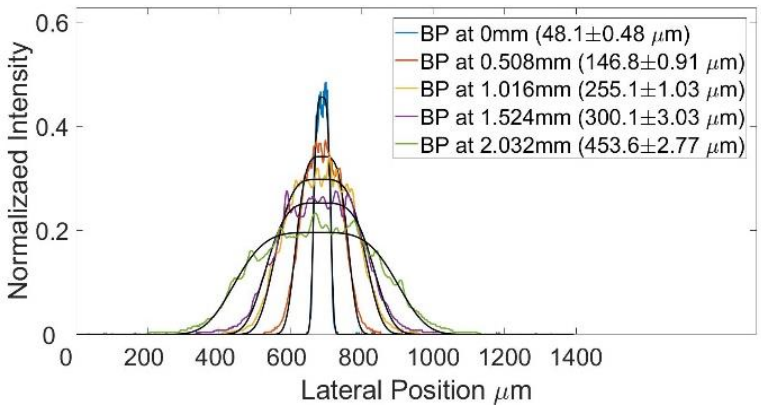

Figure 14. Cross-sectional plots of beam profiles for cleaved MMF measured at different relative positions. At each position, 9 beam profiles were acquired. The bare fiber was inserted and removed before each measurement. Mean and standard deviation were calculated at each position and are shown in the legend. Black lines are the results of fitting to a Super-Gaussian profile. The colored lines are representative curves.

The ball lens fiber endoscopes were measured in a similar way. The camera assembly was placed with its optical axis parallel to the optical axis of the laser emission from the endoscope. A comparison of measured and simulated output from a representative polished ball lens (Type 1) in air without the silica tube is shown in Figure 15. Similar results were obtained for a variety of different ball lens diameters, polishing depths and angles. The measured (solid lines) and simulated (dashed lines) results are in good agreement with an RMS error of 10.66 μm in the XY plane and 9.71 μm in the YZ plane for all data points in the plot. Nevertheless, we can readily identify several sources of error. The 350 ms heating period is sufficiently long that gravity leads to "drooping" in one axis resulting in the loss of rotational symmetry along the axis of the fiber, while retaining the reflection symmetry in the vertical plane. The ball lens drawn in Solidworks assumes rotational symmetry, hence the ellipsoid used for modeling does not account for "drooping". This is confounded by the fact that we do not control the rotational axis of the fiber endoscope in the fiber polishing system, hence the reflection symmetry plane is likely not in its preferred orthogonal position relative to the polishing plane. In other words, ideally the reflective symmetry plane would be orthogonal to the polished surface so that this reflective symmetry is retained after polishing.

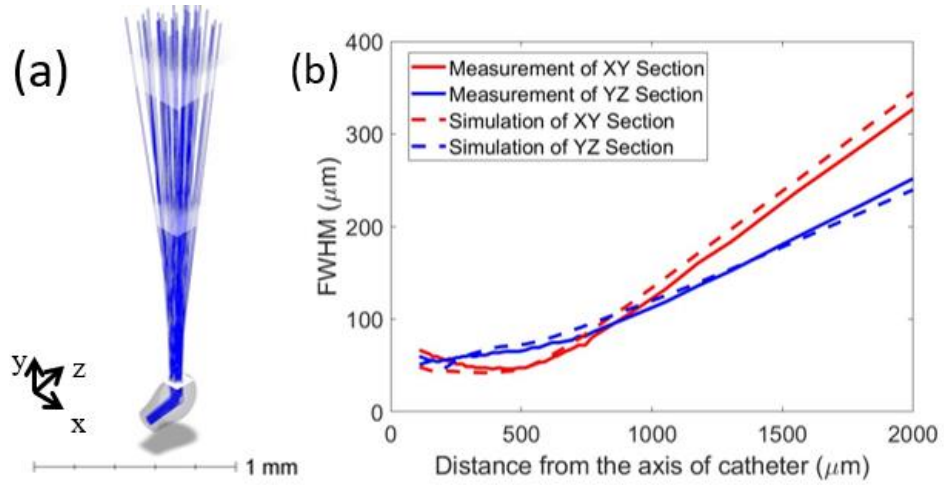

Figure 15. OpticStudio simulation of TDFLIM endoscope. (a) 3D layout of OpticStudio simulation. The grey object is the fabricated ball lens imported from SolidWorks. Blue rays are random layout rays launching from the source. White rectangle objects are detectors at different positions. (b) Simulation (dashed) and measurement (solid) of FWHM of beam intensity profiles from a representative polished ball lens (Type 1) in air without the silica tube at different positions.

Ultimately for intravascular imaging, the fiber endoscope will be placed in a catheter that is filled with flushing fluid (typically saline). Since directly measuring the optical performance in this environment is not practical, we simulated the result using the optical properties of salt water as an approximation to saline. Given the agreement between measurement and simulation in Figure 15, we can be confident that the simulated performance is a good estimation of what will be achieved during intravascular imaging.

A number of different geometries were modeled. Simulations for a pair of optimized designs, Type 1 (as in Figure 15) and Type 2 which had less astigmatism are shown in Figure 16. We also considered using a large core (100 μm) MMF to improve collection efficiency. Results for both lens types illumination are shown. The fluorescence collection efficiency for the Type 1 ball lens is 1.07 times higher than the Type 2 ball lens. However, if we move to 100 μm core fiber

the collection efficiency is improved by 1.27 over the Type 1 fiber with 50 µm core, however at the cost of substantially reduced resolution (Figure 16 (b)). Obviously both fiber core diameter and ball size affect the illumination and collection performance. In the end, we chose to fabricate the Type 1 lens with a 50 µm core MMF for the intravascular experiments described below. We felt it had the best trade-off between resolution and collection efficiency.

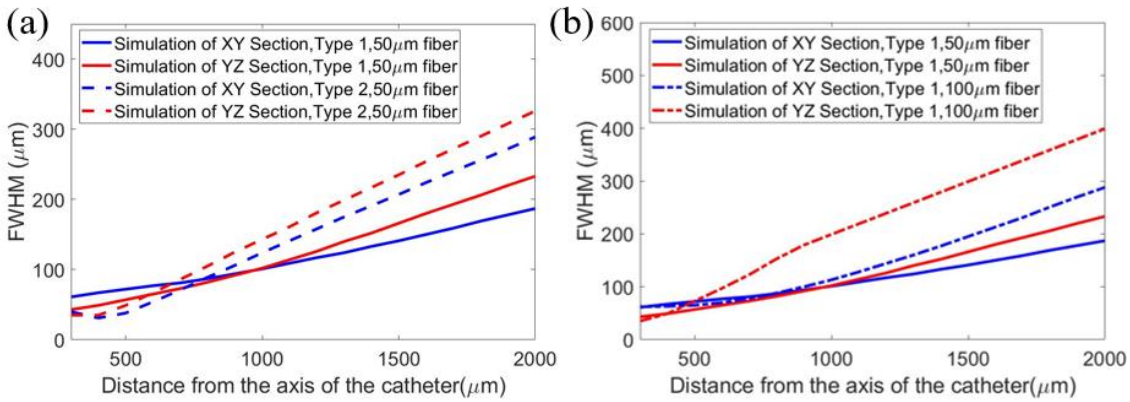

Figure 16. Simulation of FWHM of beam intensity profiles from endoscopes at different positions within a coronary artery where the saline flush was approximated by using the optical properties of salt water. (a) Type 1 ball lens representing by solid lines is the same endoscope as in Figure 15, and type 2 ball lens representing by dash lines has less astigmatism but larger FWHM. (b) FWHM by type 1 ball lens based on 50 µm and 100 µm core diameter MMF. Note the change in vertical axis scale.

4.2.2 Resolution Testing and Mechanical Testing

In order to estimate the resolution of the endoscope under more realistic imaging conditions we carried out experiments using a printed resolution target. Bars with widths ranging from 35 µm to 170 µm were printed on plain white paper. Resolution target widths were chosen based on expected resolution and what was achievable given the printer resolution. Bar widths were confirmed using a light microscope, and shown in Figure 17(a). The resolution target was wrapped

around a silica tube with 1mm ID and 2 mm OD. The tube was filled with PBS and the endoscope inserted.

Several pullback images were acquired with representative results shown in Figure 17. In Figure 17 (b) the endoscope was rotated at 2400 rpm and pulled back at a rate of 1.2 mm/s, with a laser pulse rate of 10 kHz. Under these conditions, the image sampling is 25.1 μm along the radial dimension and 30 μm along the longitudinal dimension at the surface of the resolution target. The fluorescence is attenuated in areas with ink, hence the bars show up dark in this gray scale image. The length of imaged segment is 38.4 mm. We can clearly differentiate bars with the width of 85 μm (red box in Figure 17 (b)) and line profiles were drawn (Figure 17 (c)). In Figure 17 (d) the endoscope was rotated at 6000 rpm and pulled back at a rate of 15 mm/s, and with a laser pulse rate of 12.5 kHz. Under these conditions, the image sampling is 60 μm along the radial dimension and 150 μm along the longitudinal dimension. The length of imaged segment is 60 mm. Radially, the 85 μm bars are still resolved. Longitudinally the 85 μm bars are washed out due to the under-sampling in this dimension. The first pullback experiment (Figure 17 (b)) demonstrates the resolution under imaging conditions, agreeing to within 10% of the simulation in Figure 16 (94 μm and 99 μm). Potential errors and limitations of the simulations are noted above. Experimentally, we expect deviations from the simulation based on the fact that we are imaging through a silica tube which has a higher refractive index than saline and therefore should lead to a smaller beam waist. Likewise, the endoscope is free to deviate from the center of the silica tube during rotation. The second experiment is closer to what we would like to achieve for intravascular imaging, i.e. imaging a 6 cm segment of artery in 4 s. The large artifacts in both images are due to wrinkles and nonuniform wrapping of the paper resolution target around the silica tube. However, close inspection of the resolutions bars reveals nonuniform rotational distortion (NURD) that leads

to radial errors in the position of the endoscope. This phenomenon has been reported by numerous other investigators[80, 81]. Based on Figure 17 (b), the absolute angle differences between expected bar positions and measured bar positions were normalized by expected bar positions, we estimated that the NURD contributed to mean angular error of 92.7 ± 83.3 mrad after rotating the endoscope 698 mrad in the radial dimension. While the measured NURD is appreciable, it is unlikely to lead to significant errors in the characterization of the atherosclerotic plaques with FLIM[27].

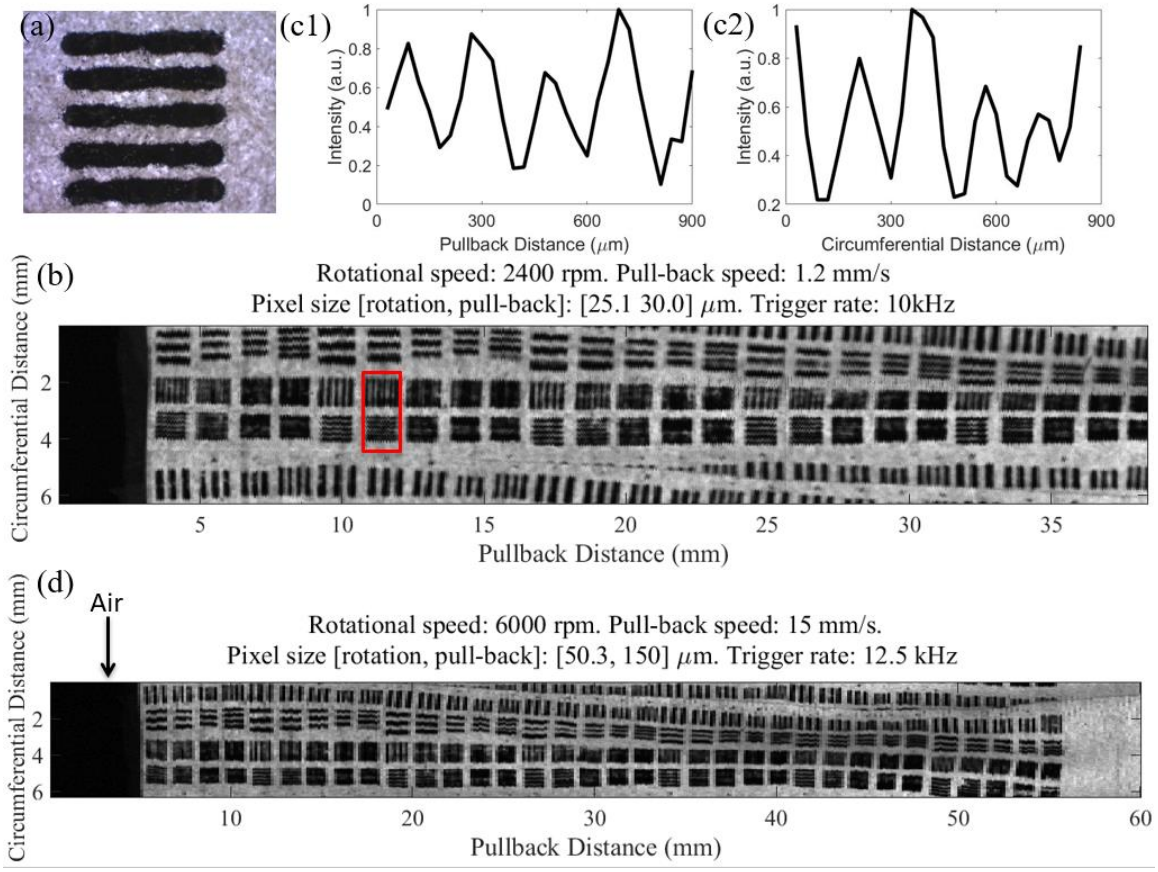

Figure 17. TDFLIM resolution demonstration experiments. (a) Resolution target with the width of 102 μm was imaged under microscope. (b) The length of imaged segment is 38.4 mm. The bars show up dark in this gray scale image, and we can clearly differentiate bars with the width of 85 μm. (c) Line profiles across bars with the width of 85 μm. (d) The length of imaged segment is 60 mm. The 85 μm bars longitudinally are washed out due to the under-sampling in this dimension.

4.2.3 Capillary Tubes Filled with Fluorophores

In order to validate the temporal and spectral calibration of the catheter imaging system we acquired images of a set of cuvettes containing well characterized fluorophores. The catheter was inserted into the silica tube with 2 mm OD. Cuvettes containing 0.1 mM POPOP, 1 mM NADH, and 1 mM FAD were placed adjacent to the silica tube for imaging. Images were acquired at a rotational velocity of 2000 rpm and pull back rate of 10 mm/s. The emission was spectrally resolved into two channels centered at 390 and 494 nm. A spectral intensity calibration to compensate for wavelength dependent losses was performed on the two spectral bands based on the measured POPOP spectrum, known transmission curves of filters and dichroic mirrors, and the POPOP spectrum[27] from the literature. The calculated average lifetimes were 1.31±0.04 ns for POPOP, 0.56±0.23 ns for NADH, 2.14±0.40 ns for FAD. The literature values for the average lifetime of POPOP, NADH, and FAD are 1.38±0.01 ns[76], 0.44 ns[77], and 2.07 ns[78], respectively. The results agreed with literature values within one standard deviation of our measurement except POPOP which differed by slightly more than one standard deviation. We consider this is to be a good agreement.

4.2.4 Ex Vivo Human Coronary Artery and Histology Analysis

Finally, we imaged a segment of human coronary artery obtained from autopsy. The catheter was inserted into the 2 mm OD silica tube which was then placed in the artery lumen. A pullback at 1.2 mm/s was performed at a rotational velocity of 2400 rpm and a pulse rate of 10 kHz. Representative calculated normalized emission intensity and lifetime images are shown in Figure 18 and Figure 19. After completing imaging, the artery segment was fixed in formalin and sent for histopathology processing.

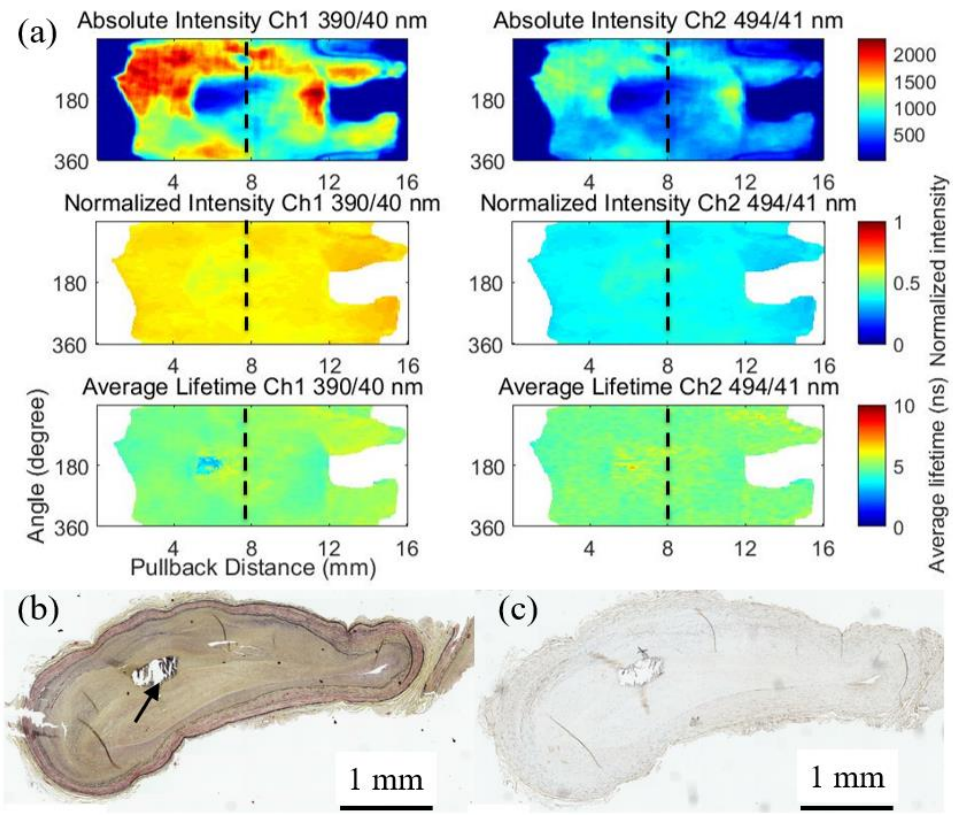

Figure 18. TDFLIM imaging and histology analysis example 1. (a) Ex vivo imaging of a segment of human coronary artery obtained from autopsy. The normalized intensity and average lifetime were calculated. (b) Histopathology result (Movat staining) and (c) Histopathology result (CD68 staining) shows that a fibrotic plaque rich in collagen and smooth muscle cells with a focal calcified region (black arrow) deep into the plaque and no observable macrophage infiltration.

The histopathology Figure 18 (b), (c) indicates a fibrotic plaque rich in collagen and smooth muscle cells with a focal calcified region (black arrow) deep in the plaque (Movat staining, panel b) and no observable macrophage infiltration (CD68 staining, panel c). Taking into account the expected FLIM interrogation depth (<200 μm), the observed homogeneous autofluorescence intensity and lifetime maps resembling collagen fluorescence (higher intensity in the Ch1, lifetimes ~5 ns) are consistent with the plaque histopathology.

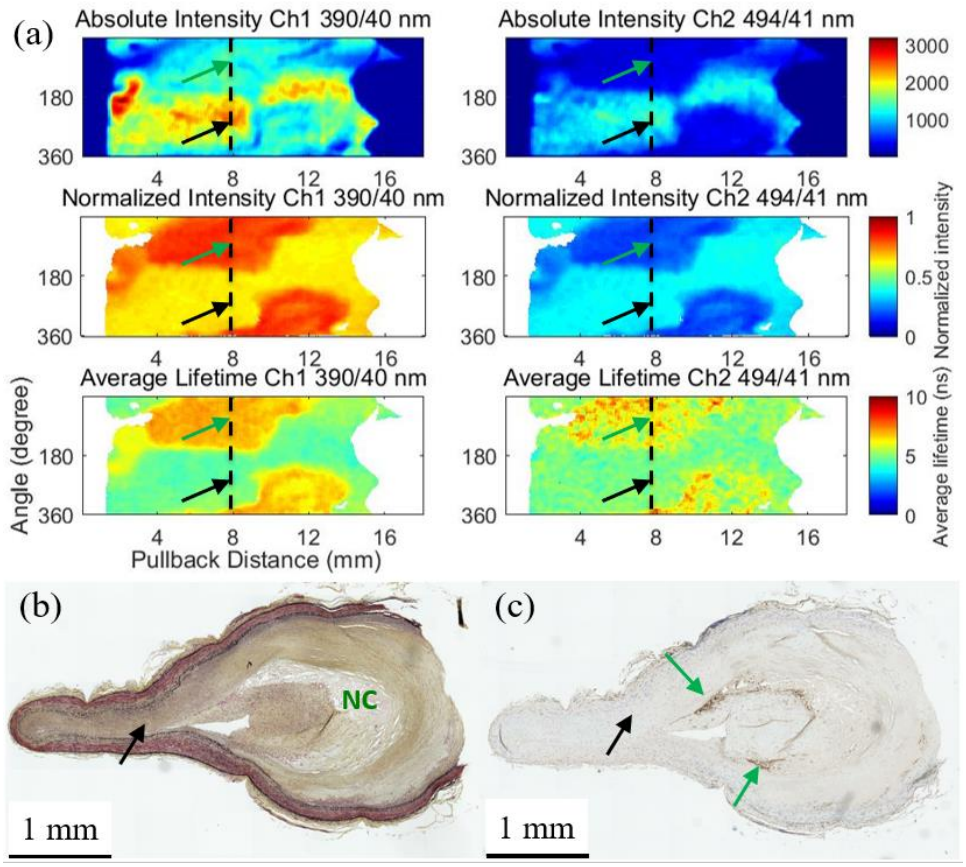

Figure 19. TDFLIM imaging and histology analysis example 2. (a) Ex vivo imaging of a segment of human coronary artery obtained from autopsy. The normalized intensity and average lifetime were calculated. (b) Histology result (Movat staining) and (c) Histology result (CD68 staining) shows a fibroatheroma with a thick cap rich in collagen and smooth muscle cell covering a large necrotic core (NC) with significant macrophage infiltration (green arrows). Black arrows and green arrows indicate two distinct regions, collagen and a combination of collagen and lipid, respectively.

The histopathology Figure 19 shows a fibroatheroma with a thick cap rich in collagen and smooth muscle cell covering a large necrotic core (NC) (Movat staining). The cap also shows significant macrophage infiltration (green arrows) (CD68 staining). The region next to the fibrotatheroma (black arrows) shows a thickened intima rich in collagen and smooth muscle cells (Movat staining) and no observable macrophage infiltration (CD68 staining). The

autofluorescence intensity and lifetime maps show two distinct regions resembling: a) collagen (higher intensity in the Ch1, lifetimes ~5 ns) reflecting the thickened fibrotic intima (black arrows), and b) a combination of collagen and lipid (weak fluorescence intensity in the Ch1, lifetimes >6 ns) reflecting the presence of the lipid rich necrotic core and macrophages (green arrows). These observations are also consistent with the described plaque histopathology.

4.3 Conclusions

This study demonstrates a simulation, fabrication, and measurement method for ball lens-based endoscopes based on multimode fiber. The simulation and measurement method can be used to design endoscopes with a wide range of sizes using a variety of MMF. Different types of MMF and ball size can be chosen to make a tradeoff between optical resolution and collection efficiency for a specific application. It also enables simulation of operating environments where it is not practical to make direct measures of optical properties, such as the coronary artery with a saline flush.

A FLIM endoscope designed and fabricated using this method exhibited optical performance comparable to the simulation. In conjunction with an intravascular FLIM imaging system we were able to show that the endoscope was able to measure fluorescence emission from a set of standard fluorophores with sufficient collection efficiency to enable lifetime estimation that was in good agreement with literature values. Finally, we were able to make FLIM measurements with the catheter on an ex vivo human coronary artery and found that the measure fluorescence intensity and lifetime were consistent with expectations from the arteries histopathology.

5. BALL LENS-BASED INTRAVASCULAR FREQUENCY-DOMAIN FLUORESECENCE LIFETIME IMAGING MICROSCOPY ENDOSCOPE [*]

This chapter explains a combined simulation, fabrication, and measurement method for ball lens-based endoscope based on DCF and applied them to intravascular FDFLIM system. The endoscope was simulated with OpticStudio to predict the performance of any given endoscope in the intravascular environment. Using the technique, a ball lens endoscope based on a DCF was developed. The endoscope was demonstrated for fluorescence lifetime imaging by measuring fluorescence standards as well as fresh ex vivo human coronary arteries.

5.1 Material and Methods

5.1.1 Simulation and Validation of Ball Lens Based Endoscope Performance

We chose the Super-Gaussian [72, 73] profile which approximates a top-hat profile with Gaussian tails on either side discussed in Chapter 4. The intensity profile is $I(r) = I_0 exp\left[-2\left(r / w_m\right)^n\right]$, where r is the radial dimension, w_m is the beam waist, and n is the order of the Super-Gaussian. Intensity profiles from the core and the inner cladding were measured respectively while the laser is transmitting through the core and the inner cladding respectively with the focusing system discussed in 5.2.1. Methodology to reliably measure and manipulate the intensity profile is discussed in Chapter 4.

The output of the endoscope was modeled with OpticsStudio in non-sequential mode. We rendered the ellipsoidal ball-lens using Solidworks and imported it into OpticStudio. The intensity

[*] Parts of this section have been reprinted with permission from X. Chen, W. Kim, M. J. Serafino, Z. Tan, J. A. Jo, and B. E. Applegate, "Dual-modality optical coherence tomography and frequency-domain fluorescence lifetime imaging microscope system for intravascular imaging," Biomed. Opt. **25**(9), 096010 (2020), doi: 10.1117/1.JBO.25.9.096010

profiles from the core and the inner cladding were modeled based on two source-radial sources with different ratio power depending on experiment setup. The beam profiles on artery could be estimated with the method.

The collection efficiency is a critical aspect of a FLIM system, hence an important parameter to be considered for ball lens design. Collection performance simulation of the endoscope was discussed in Chapter 4. This allows us to make comparisons and rational decisions concerning trade-offs between collection and illumination performance.

5.1.2 Design of Ball Lens Endoscope

A fiber preparation and splice workstation (FFS2000, Vytran) was used for endoscope fabrication. The 1.55-meter OCTFLIM endoscope was constructed starting with a DCF (SM-9/105/125-20A, Nufern). DCF was cleaved to a precise length and then fusion spliced to a CLF (HCF-125-47, Coractive). Following splicing, the CLF was cleaved to a precise length, heated and shaped into an ellipsoid ball with predetermined semi-principal axes in the tungsten filament furnace of the workstation, shown in Figure 20. The ellipsoidal shape was designed to compensate for the astigmatism caused by the toroidal shape of the catheter sheath and the silica tube used to cover and protect the fiber endoscope. The distal ball lens was polished with an angle of 41° using a commercial fiber polisher (69-3000-160, Buehler) with custom modifications to enable ball lens polishing at precise angles for side viewing endoscopes. The 41° angle was chosen so that total internal reflection (TIR) would occur at the polished glass-air interface, hence obviating the need for reflective coatings on the polished surface. In addition to the angle, precise control of the polishing depth from unpolished ball is necessary in order to achieve good performance.

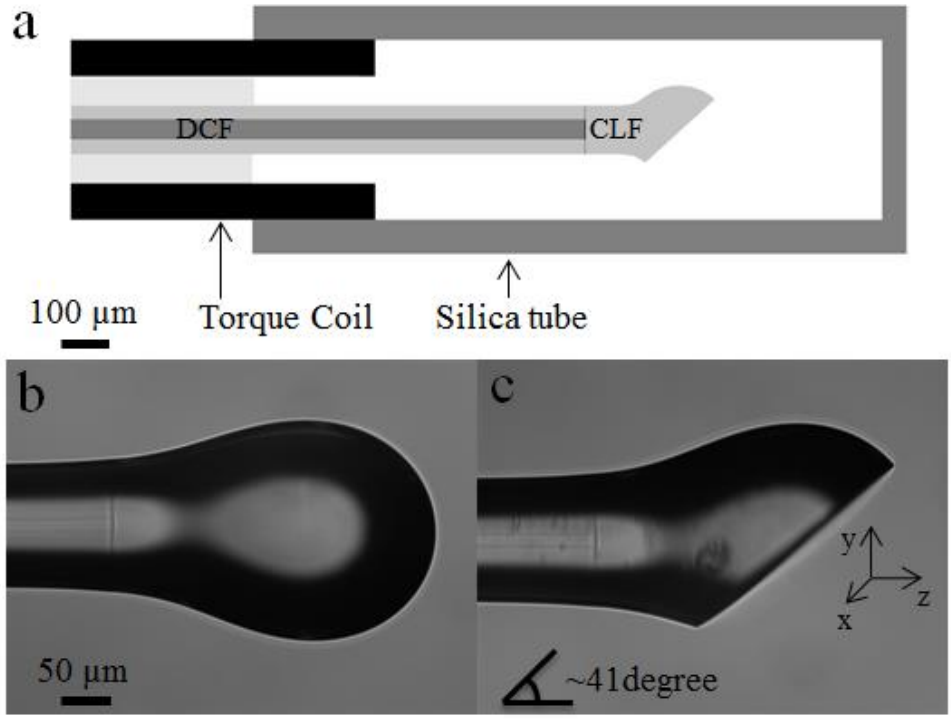

Figure 20. Schematic drawing of FDFLIM endoscope. (a): Schematic drawing of the catheter. Heated and shaped CLF fusion spliced to a stripped DCF, and the fiber was glued with torque coil and silica tube. Torque Coil's ID is 270 µm and OD is 450 µm. Silica Tube's ID is 530 µm and OD is 620 µm. Scale bar: 100 µm. DCF: double clad fiber. CLF: coreless fiber. (b): Side view of the fabricated ball lens before polishing. Heated and shaped CLF fusion spliced to a DCF. Scale bar: 50 µm. (c): Side view of the ball lens after polishing by customized fiber polishers. The polishing angle is 41°.

5.1.3 FLIM Instrumentation

The frequency-domain FLIM system shown in Figure 21, utilized an ultra-compact diode laser (IBEAM-SMART-375, Toptica) as the excitation source (375 nm). The laser excitation was reflected into the rotary joint and endoscope via an angle-tuned dichroic mirror (FF376-Di01, Semrock) for more refection. The fluorescence emission returning from the endoscope was separated from the excitation by the dichroic mirror and then further separated into three channels (Ch1 405/20 nm, Ch2 440/40 nm and Ch3 525/50 nm) using a set of dichroic mirrors and filters

(Chroma Technology and Semrock). Each channel was detected with a high-sensitivity APD (C5331-11, Hamamatsu) and a low noise amplifier (ZFL-500LN+) through optical fiber with custom SMA adapter plate for APD. Modulated emissions were sampled at 250Ms with a 4-channel, 500MHz analog bandwidth digitizer (NI-5761 National Instrument). The energy of the incident light on the sample was maintained below the ANSI maximum permissible exposure for skin [25].

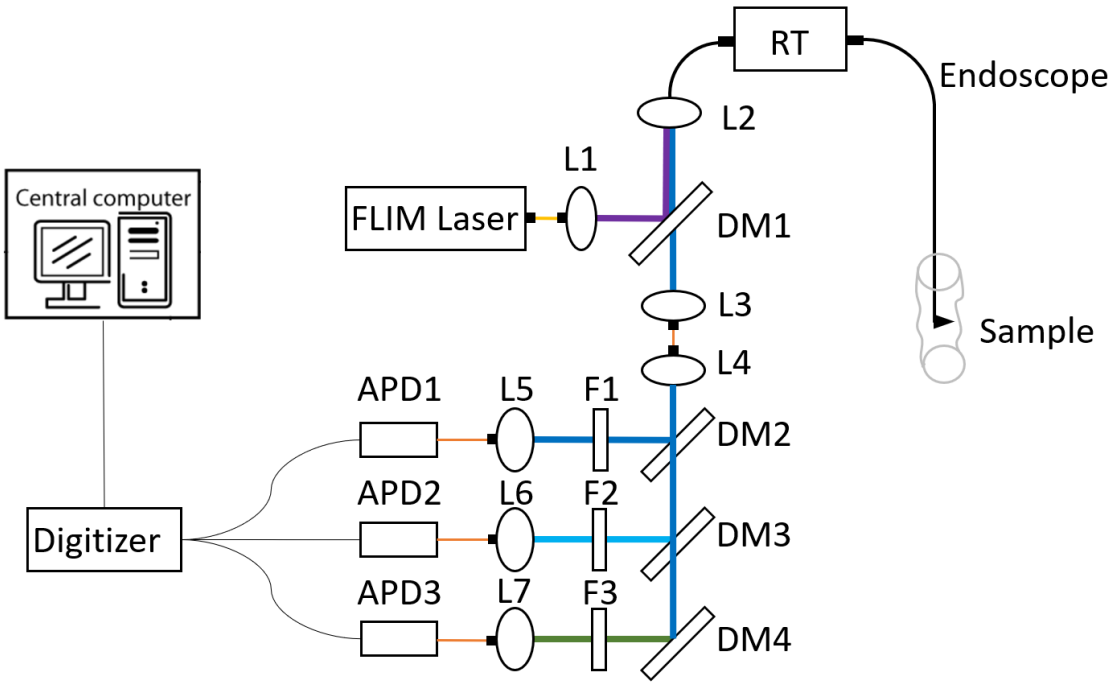

Figure 21. Schematic diagram of the FDFLIM system. L1 and L2: free-space collimation and coupling lenses, L3, L4: fiber-connected collimation and coupling lenses. DM1 – DM4: dichroic mirrors, F1-F3: bandpass filters, APD1-APD3: avalanched photodiodes, RT: rotary joint. Orange line indicates MMF fiber transmission. Yellow line indicates SMF transmission. Other thick colored lines indicate free-space transmission. Black thin line indicates electrical line.

5.1.4 Tissue Preparation and Imaging

Human coronary artery segments were obtained from autopsy cases within 3 days of the time of death, according to a protocol approved by the Texas A&M University Institutional Review Board. The arterial segment was imaged by placing the endoscope inside the lumen of the artery performing a pullback. Immediately after imaging, each segment was ink marked for correlation with histopathology, fixed in 10% formalin, and sent for histopathology analysis. Each image plaque segment was consecutively sectioned every 1 mm. The sections were stained with Movat pentachrome and CD68 staining and evaluated by a cardiovascular pathologist.

5.2 Results and Discussion

In order to validate the performance of the developed intravascular FLIM system, measurements and simulations were completed on the optical and mechanical functionality.

5.2.1 Power Ratio between Core and Inner Cladding

The laser from the source was shining from the SMF with ~3.5 μm MFD at 375nm and the beam was coupled into the DCF through two lenses (L1 and L2 in Figure 21). After the optical simulation and optimization, the combination of the collimator lens (A260-A, Thorlabs) and the focusing lens (A240-A, Thorlabs) were chosen to focus laser into DCF with specified NA and MFD. The relative position between collimator and the laser fiber, and the position between focusing lens and DCF can be adjusted for specific NA and MFD onto the DCF guiding by optical simulation, to control different power ratio into the core and the inner cladding.

The beam profiler (BP104-IR, Thorlabs) was mounted on a translation stage and positioned perpendicular to the optical axis so that beam profile after the focusing lens (L2) could be measured at several distances along the optical axis. The beam profiles with specific collimator (L1) position were measured by the beam profiler at different places and then were fitted according to Gaussian

beam propagation equation (3). Measured and fitted NA and beam waist after focusing lens were compared with the simulation and shown in Figure 22. The experiment results matched the simulation and it confirmed that the system could adjust the beam profile onto the DCF to change the power ratio between the core and the inner cladding.

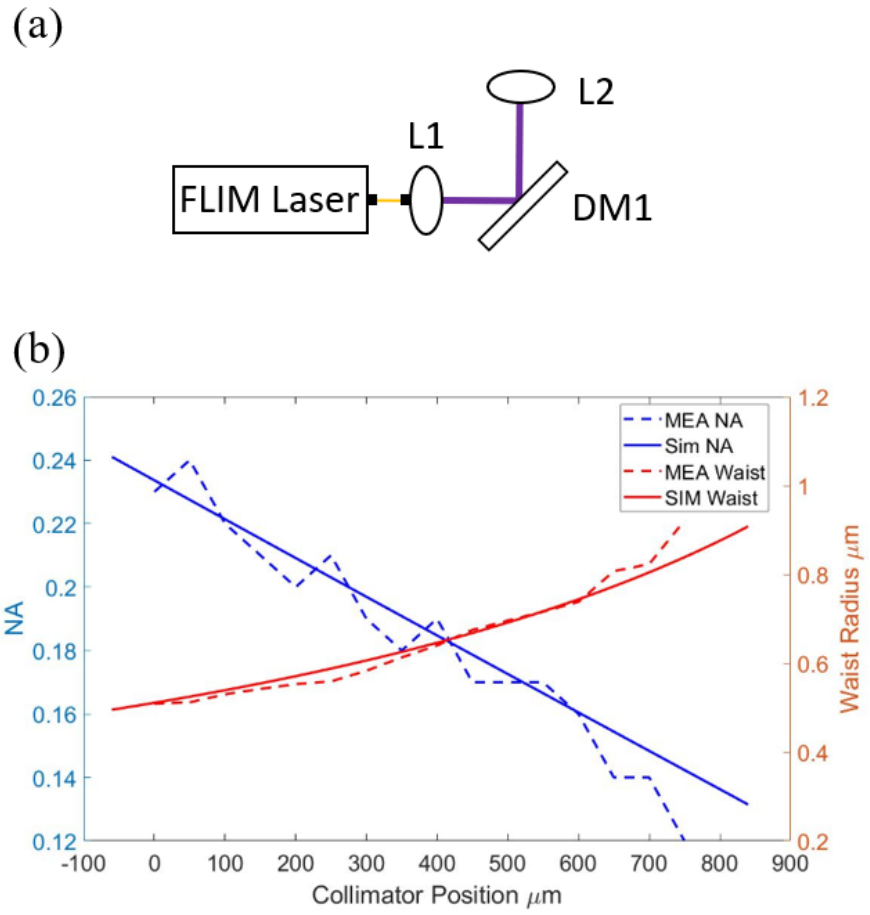

Figure 22. The excitation path beam focusing system. (a) Schematic diagram of the FDFLIM system excitation path. L1 and L2: free-space collimation and coupling lenses. DM1: dichroic mirror. Yellow line indicates SMF transmission. Purple thick colored lines indicate free-space transmission. (b) Measurement and simulation of beam profiles after focusing lens L2. Solid lines are simulation and dashed lines are measurement; blue lines are NA data and red lines are beam waist data.

5.2.2 Solarization and Two-Photon Absorption

Transmission loss due to absorption and solarization are important when coupling high power UV light into optical fibers as we do for FLIM excitation. As has been reported previously, high intensity pulses suffer greater losses due to two-photon absorption.17,27 Two-photon absorption has been shown to be the dominant process for the formation of radiation-induced defects in silica material.18 Similarly, solarization and thermal cumulative effects are known to become significant for high power UV transmission through the core.17,19,28 For our system, the intensity of light can be up to 0.1 MW/cm2 if transmitting through the core. Therefore, both processes should be considered carefully since they can degrade the fiber transmission and affect the optical performance.

The propagation of a laser pulse has nonlinear transmission properties including one- and two-photon absorption, and two photon absorption process is known to be the dominant process for formation for radiation-induced defects in silica material[82]. The transmission could be described by[83],

$$T^{-1} = (1+\beta)\exp(\alpha_0 l) - \beta \qquad (15)$$

where T is the fiber transmission, α_0 is the one-photon absorption coefficient, α_1 is the two-photon absorption coefficient, $\beta = \alpha_1 I_{input} / \alpha_0$ is the propagation constant and l is the fiber length.

The one-photon and two-photon absorption coefficient of the core were measured by cut-off method. The laser was focused to SMF (SMF28e, Corning) patch cable by adjusting collimating lens and focusing lens. The SMF patch cable was solarized thoroughly after shinning 375nm laser at 50mW for 5min and output was stable after 1-hour recovery time. SMF patch cable fiber was connected with DCF patch cable by mating sleeve, 0.5s pulse with different power was

incident into SMF patch cable and the output power from DCF patch cable was measured. Known distance of DCF patch cable was cut off and then the output power from DCF patch cable was measured again while shining 0.5s pulse with the respectively same power. The one-photon absorption and two-photon absorption of the core were calculated as $3.14\times10^{-3}cm^{-1}$ and $2.88\times10^{-1}cm/MW$ by fitting with the equation (15) and shown in Figure 23.

Similarly, the one-photon absorption and two-photon absorption of the inner cladding were calculated as $1.54\times10^{-3}cm^{-1}$ and $1.50cm/MW$ shown in Figure 23. The power was focused to MMF (FG105UCA, Thorlabs) patch cable by adjusting collimating lens and focusing lens. The MMF patch cable was noted as resistant to solarization but was solarized thoroughly after shinning 375nm laser at 50mW for 5min and output was stable after 1-hour recovery time to avoid solarization effect on the measurement. MMF patch cable was connected with another DCF patch cable by mating sleeve, 0.5s pulse with different power was incident into SMF and the output power from DCF patch cable was measured. Known distance of DCF patch cable was cut off and then the output power from DCF patch cable was measured again while shining 0.5s pulse with the respectively same power.

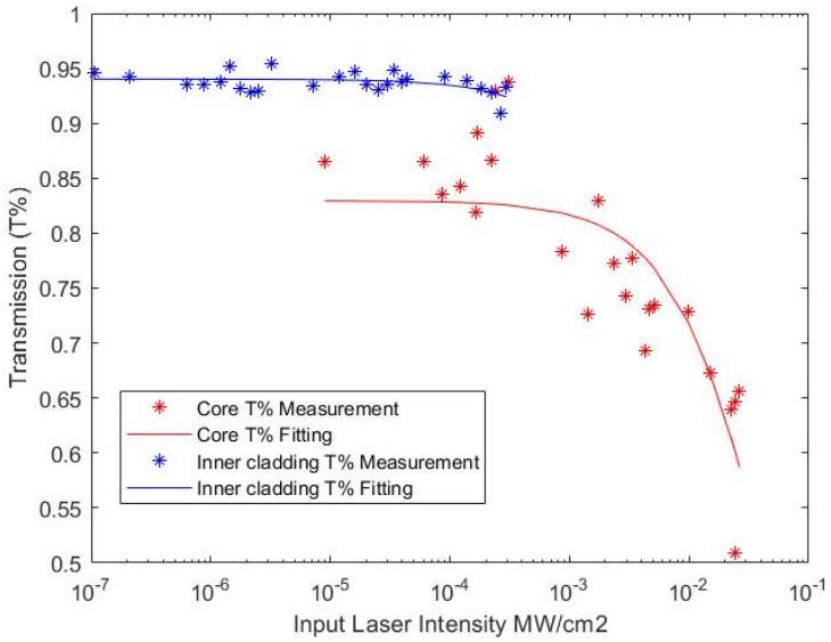

Figure 23. One-photon absorption and two-photon absorption at 375nm. Curves are fitting of equation (1). Transmission of the inner cladding is measured based on 40cm DCF, and transmission of the core is measured based on 59.5cm DCF.

Ultraviolet radiation degrades the fiber transmission (solarization), especially in high-OH fiber. The solarization rate of the DCF is important for our application since we want to be confident that the optical properties of the system are not changing over the course of an imaging session. In order to measure the solarization rate of the core we used the following technique. An SMF (SMF28e, Corning) patch cable was pre-solarized by illumination with 50 mW of 375 nm light so that the transmission was stable and solarization recovery didn't happen after 1 hour. This patch cable was connected to a 1.55m DCF patch cable so that the light from the core of the SMF was reliably transmitted to the core of the DCF. The output power from the DCF was then measured as a function of time to produce the curves in Figure 24. As expected, the solarization rate increases when the input power to the DCF is increased. We tried a similar experiment on the

inner cladding; however, we were not able to measure any change in transmission over the time course of the experiment, hence no significant solarization. We also measured the absorption coefficients using the same cut-off method noted above after the solarization experiment. The one-photon coefficient for the core more than doubled to $7.26\times10^{-3}cm^{-1}$ while the one-photon coefficient remained approximately the same for the inner cladding, $1.61\times10^{-3}cm^{-1}$. The small increase in the one-photon absorption can be explained by the fact that the measurements on the inner cladding includes light that propagates through the core. The two-photon coefficients cannot be measured because the 50 mW incident power cannot induce strong enough intensity for two-photon coefficients measurements when the one-photon absorption is so high.

It would be advantageous to illuminate the sample through the core in order to achieve ~4X higher spatial resolution than illumination through the inner cladding. However, given that an imaging session will likely require the illumination of the catheter for 10s of seconds, if we excite through the core, we will lose about 30-40% of the excitation light due to solarization. Since collection of the fluorescence is largely dependent on the inner cladding transmission, it should not be significantly impacted. Hence given a bright enough light source, it should be possible to illuminate through the core to gain higher spatial resolution. More generally, if longer wavelength illumination can be used, it would also mitigate the solarization issue.

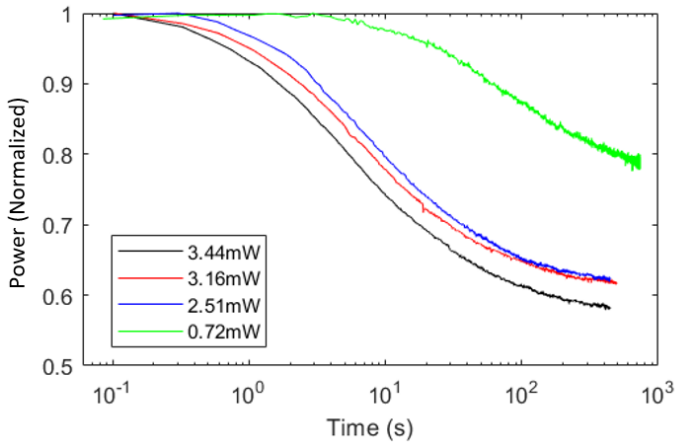

Figure 24. Solarization rate of DCF core. The DCF core could be solarized when the power is higher than 0.7mW and solarization rate is faster as the power increases.

5.2.3 Resolution Testing and Mechanical Testing

Given that we were testing a new system with imaging times that would lead to strong solarization and that DCF have been fabricated to guide UV either entirely through the core or the inner cladding[84], we chose to illuminate primarily through the inner cladding. We aligned the optical system to adjust the output power ratio between core (7%) and the inner cladding (93%) for a trade-off between spatial resolution and output power.

We optimized the mode mixing in the DCF to generate a Super-Gaussian profile. We found this to be stable even when the endoscope fiber is rotating rapidly. The stability of the Super-Gaussian output gave us confidence that we could expect a similar intensity profile at the interface of the coreless fiber and the DCF in the endoscope. The intensity profiles from the core and the inner cladding were modeled based on two source-radial sources. The collection efficiency was also modeled for resolution estimation. The 3-D layout from OpticStudio including rays from the core (green) and inner cladding (blue) are shown in (a). The plane (orange) represents the receiver where the beam profile was simulated. The resolution at 1 mm from the center of the fiber is shown

in Figure 25(b). The XY section FWHM resolution and YZ section FWHM resolution were 99 μm and 88 μm respectively while 70% (* in Figure 25(b)) power was transmitting out of the core and 30% power was transmitting out of the inner cladding. Under our planned experimental conditions, i.e. 7% power was transmitting out of the core, the XY section resolution and YZ section resolution were 111 μm and 99 μm respectively (* in Figure 25(b)). Nominally, the resolution can be tuned by adjusting the relative power transmitting through the core and the inner cladding.

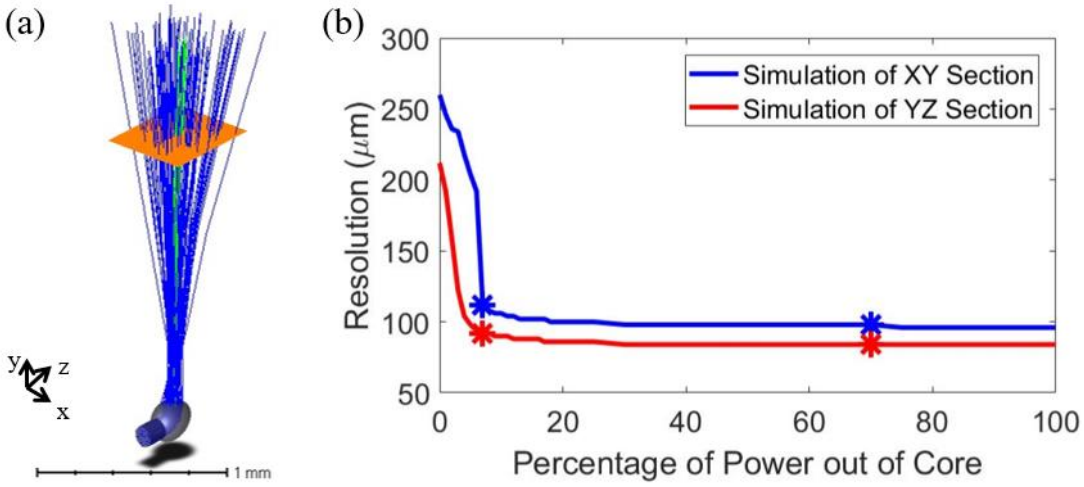

Figure 25. OpticStudio simulation FDFLIM endoscope. (a) 3D layout of OpticStudio simulation. The grey object is the fabricated ball lens imported from SolidWorks. Blue rays are random layout rays launching from the inner cladding, and green rays are random layout rays launching from the core. The orange plane represents the receiver that was translated along the beam bath in order to extract the resolution plotted in panel (b). (b) Simulation of resolution of XY section and YZ section at 1 mm from the center of the fiber with different power transmitting out of the core. Asterisks indicates simulated resolution with two scenarios mentioned in the text.

In order to confirm the resolution of the endoscope under realistic imaging conditions, a resolution target (53-715, Edmund Optics) was wrapped around a silica tube with 1 mm ID and 2 mm OD. The white paper has high fluorescence while the black ink has low fluorescence. The

fluorescence intensity maps were used to define FLIM spatial resolution. The tube was filled with PBS and the endoscope inserted. Several pullback images were acquired with representative intensity maps shown in Figure 26. In Figure 26(a), the endoscope was rotated at 2358 rpm and pulled back at a rate of 0.4 mm/s. Under these conditions, the image sampling is 9.5 μm along the radial dimension and 10.2 μm along the longitudinal dimension at the surface of the resolution target. The fluorescence is attenuated in areas with ink, hence the bars show up dark in this gray scale image. We can clearly differentiate bars with the width of 111 μm (Group 2 Element 2) in rotation direction and 99 μm (Group 2 Element 3) in longitudinal direction. In the Figure 26(b), the endoscope was rotated at 2358 rpm and pulled back at a rate of 0.35 mm/s. Under these conditions, the image sampling is 9.5 μm along the radial dimension and 8.9 μm along the longitudinal dimension at the surface of the resolution target. We can clearly differentiate bars with the width of 99 μm(Group 2 Element 3) in rotation direction and 88 μm (Group 2 Element 4) in longitudinal direction. Experimentally, we expect deviations from the simulation based on the fact that we are imaging through a silica tube which has a higher refractive index than saline and therefore should lead to a smaller beam waist. Likewise, the endoscope is free to deviate from the center of the silica tube during rotation.

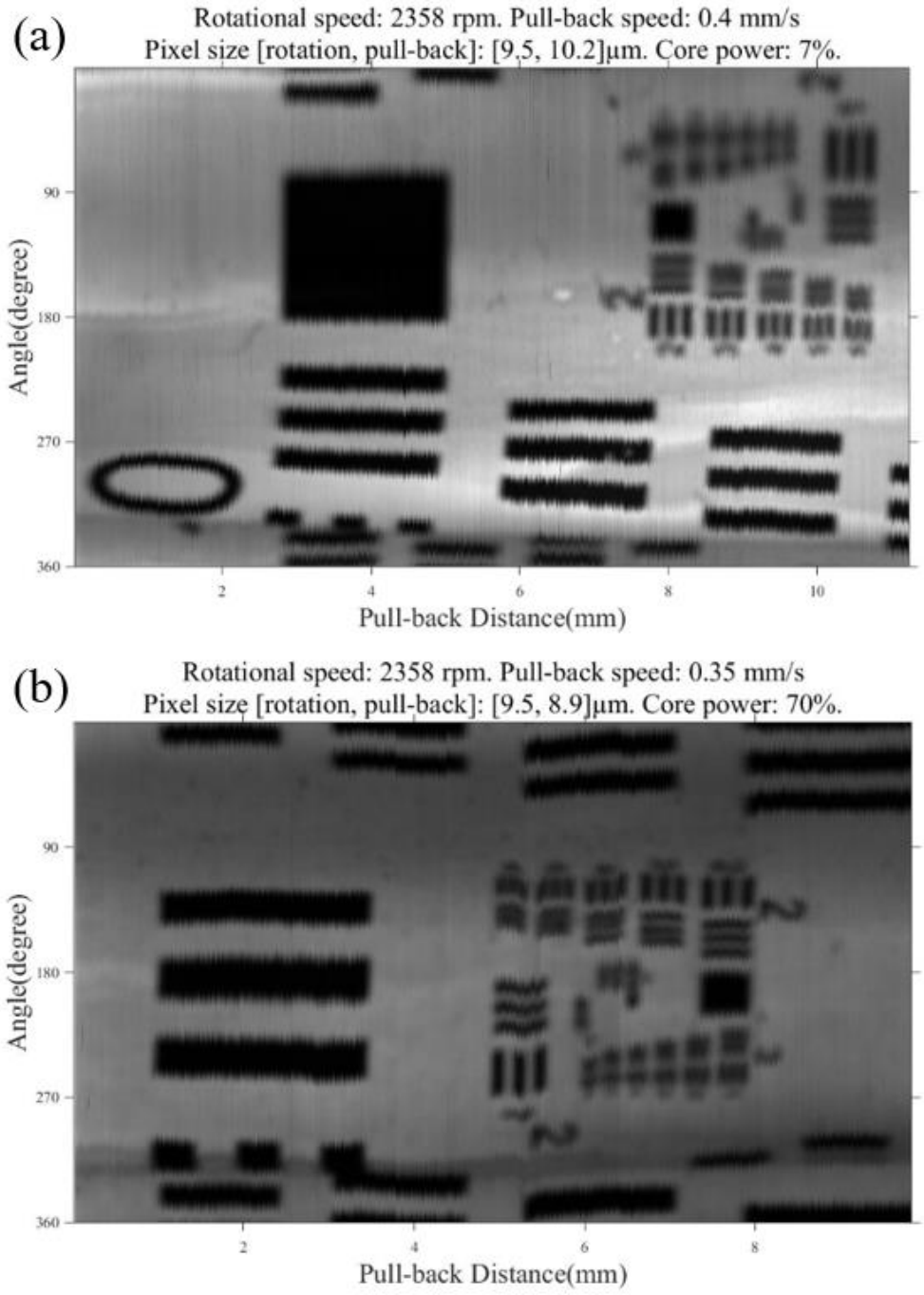

Figure 26. Pullback fluorescence intensity images of resolution targets. (a) The bars show up dark in this gray scale image, and we can clearly differentiate bars with the width of 99 μm radially and 111 μm longitudinally while 7% power transmitting out of the core. (b) we can clearly differentiate bars with the width of 88 μm radially and 99 μm longitudinally while 70% power transmitting out of the core.

5.2.4 Ex Vivo Human Coronary Artery and Histology Analysis

Finally, we imaged segments of human coronary artery obtained from autopsy. The catheter was placed in the artery lumen. A pullback at 2.24 mm/s was performed at a rotational velocity of 2253 rpm and excitation was modulated with 1.25 MHz, 20.83 MHz, 41.67 MHz, 62.5 MHz and 83.3 MHz. Representative calculated normalized emission intensity and lifetime images are shown in Figure 27 and Figure 28. After completing imaging, the artery segment was fixed in formalin and sent for histopathology processing.

The histopathology Figure 27 shows a fibroatheroma with a thick cap rich in collagen and smooth muscle cell covering a few small necrotic core (NC) (Movat staining). The cap also shows significant macrophage infiltration (green arrows) (CD68 staining). The region next to the fibrotatheroma (black arrows) shows a layer of intima rich in collagen and smooth muscle cells (Movat staining) and no observable macrophage infiltration (CD68 staining). The autofluorescence intensity and lifetime maps show two distinct regions resembling: a) a combination of collagen and lipid (weak fluorescence intensity in the Ch1, lifetimes >6 ns) reflecting the presence of the lipid rich necrotic core and macrophages (green arrows) and b) collagen (higher intensity in the Ch1, lifetimes ~5 ns) reflecting the thickened fibrotic intima (black arrows), These observations are also consistent with the described plaque histopathology.

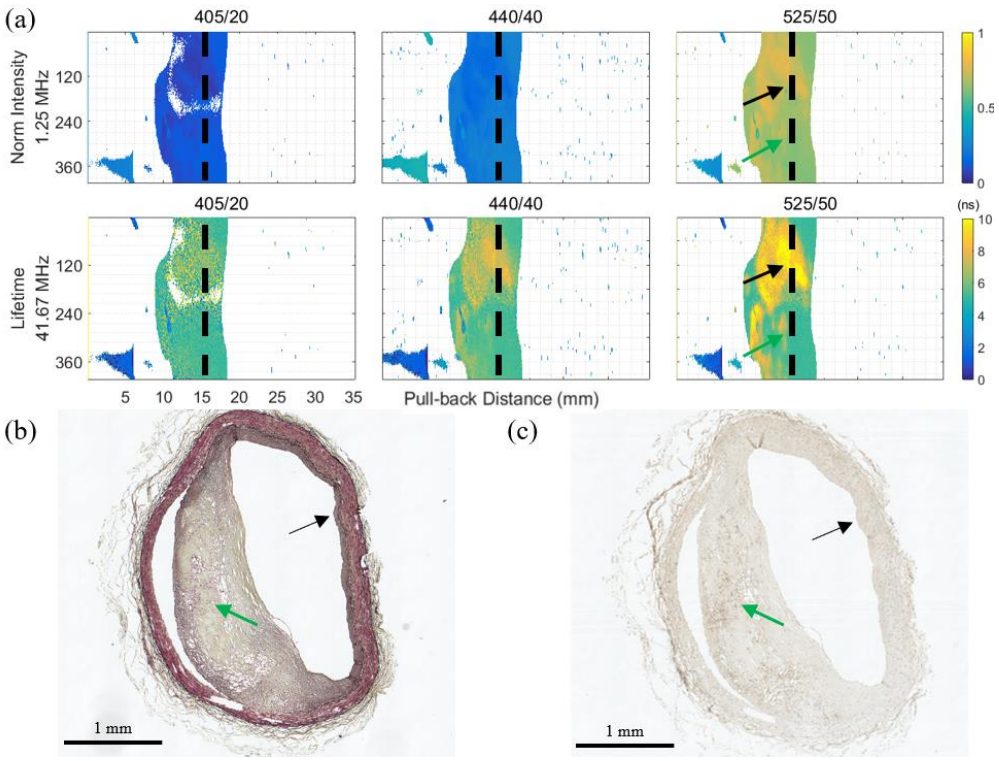

Figure 27. FDFLIM imaging and histology analysis example 1. (a) Ex vivo imaging of a segment of human coronary artery obtained from autopsy. The normalized intensity and average lifetime measured at 41.67 MHz were calculated. (b) Histopathology result (Movat staining) and (c) Histopathology result (CD68 staining) shows a fibroatheroma with a thick cap rich in collagen and smooth muscle cell covering a few small necrotic core (NC) with macrophage infiltration (green arrows). Black arrows and green arrows indicate two distinct regions, collagen and a combination of collagen and lipid, respectively.

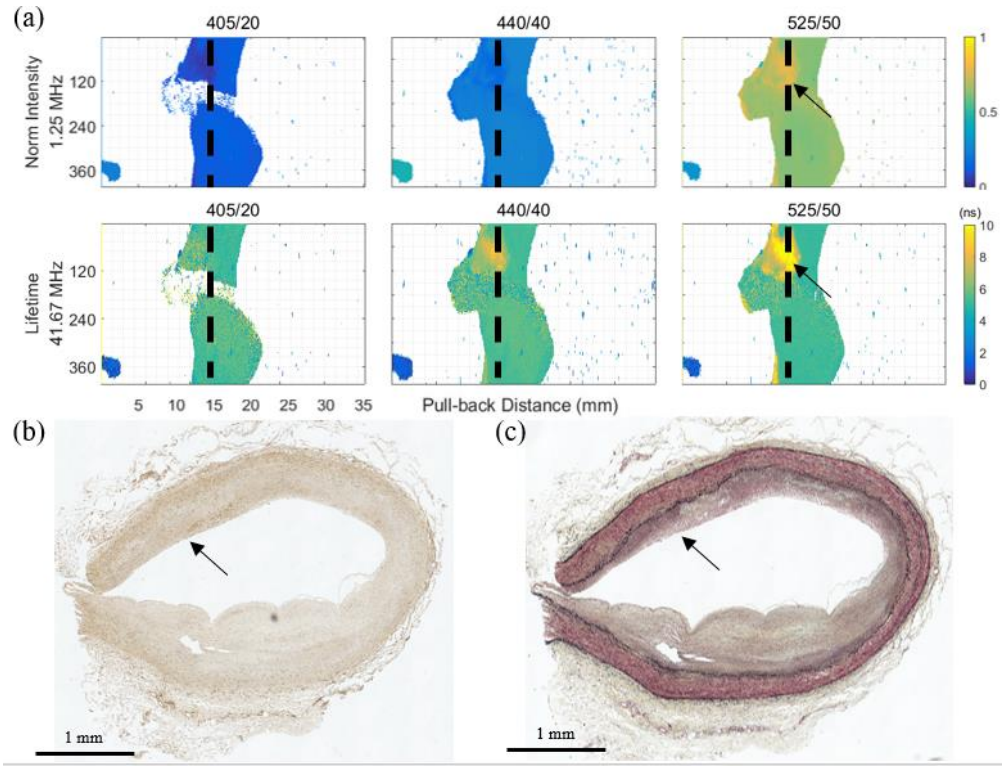

Figure 28. FDFLIM imaging and histology analysis example 2. (a) Ex vivo imaging of a segment of human coronary artery obtained from autopsy. The normalized intensity and average lifetime measured at 41.67 MHz were calculated. (b) Histopathology result (Movat staining) and (c) Histopathology result (CD68 staining) indicates a thick cap rich in collagen and smooth muscle cell with infiltrated macrophage in the area (black arrows).

The histopathology Figure 28 (b), (c) indicate a thick cap rich in collagen and smooth muscle cell (Movat staining, panel b) and a area of infiltrated macrophage (CD68 staining, panel c). The autofluorescence intensity and lifetime maps show the area with infiltrated macrophage (black arrows, lifetimes >6 ns) shows longer lifetime than area without observable infiltrated macrophage (lifetimes ~5 ns).

5.3 Conclusions

This study demonstrates a simulation, fabrication, and measurement method for ball lens-based endoscopes based on double clad fiber. The simulation and measurement method can be

used to design endoscopes with a wide range of sizes using a variety of DCF. It also enables simulation of operating environments where it is not practical to make direct measures of optical properties, such as the coronary artery with a saline flush. Due to the limitation of the current commercial DCF performance, the power would be attenuated while transmitting through the core, but the simulation could help make tradeoff between resolution and SNR.

A FLIM endoscope designed and fabricated using this method exhibited optical performance comparable to the simulation. In conjunction with an intravascular FLIM imaging system we were able to show that the endoscope was able to measure fluorescence emission from a set of standard fluorophores with sufficient collection efficiency to enable lifetime estimation that was in good agreement with literature values. Finally, we were able to make FLIM measurements with the catheter on an ex vivo human coronary artery and found that the measure fluorescence intensity and lifetime were consistent with expectations from the arteries histopathology.

6. BALL LENS-BASED INTRAVASCULAR DUAL-MODALITY OPTICAL COHERENCE TOMOGRAPHY AND FREQUENCY-DOMAIN FLUORESECENCE LIFETIME IMAGING MICROSCOPY ENDOSCOPE[†]

This chapter explains a combined simulation, fabrication, and measurement method for ball lens-based endoscope based on DCF and applied to intravascular OCT and FDFLIM system. Endoscope's optical properties was simulated with OpticStudio to predict the performance of any given endoscope in the intravascular environment. Optimization and fabrication tolerance analysis were analyzed and implemented for the application. Using the technique, a ball lens endoscope based on a DCF was developed. The endoscope is demonstrated for fluorescence lifetime imaging by measuring fluorescence standards as well as fresh ex vivo human coronary arteries.

6.1 Material and Methods

6.1.1 Simulation of OCT Endoscope

We set out to simulate the performance of the endoscope via the optical ray-tracing program OpticStudio, in order to optimize the ball lens design prior to manufacture. Simulation is important to minimize manufacturing time by establishing a preferred shape for the partial ellipsoid lens before the manufacturing process. OpticStudio could simulate wavefronts propagation while coherently interfering with themselves after the ball lens and predict beam profiles along two directions even with astigmatism, which is more accurate for side-viewing, circularly asymmetric, and non-paraxial ball lens than ABCD matrix method [13, 14].

[†] Parts of this section have been reprinted with permission from X. Chen, W. Kim, M. J. Serafino, Z. Tan, J. A. Jo, and B. E. Applegate, "Dual-modality optical coherence tomography and frequency-domain fluorescence lifetime imaging microscope system for intravascular imaging," Biomed. Opt. **25**(9), 096010 (2020), doi: 10.1117/1.JBO.25.9.096010

A sheath with toroidal shape is always installed around fiber endoscope, which causes astigmatism between XY and YZ sections shown in the Figure 29. To compensate for the astigmatism caused by the toroidal shape of the sheath and glass tube, the ball lens was intentionally heated to ellipsoid for OCT endoscope, like FLIM endoscope mentioned in Chapter 4 and Chapter 5. Unlike the FLIM endoscope, OCT endoscope design affects lateral resolution effectively, so the OpticStudio model was set up to optimize the ball lens shape and length, shown in the Figure 29.

(a)

	Surf:Type		Comment	Radius	Thickness	Material	Coating	Clear Semi-Dia	Chip Zone	Mech Semi-Dia	Conic	TCE x 1E-6	Par 1(unused	Par 2(unused	Par 3(unused
0	OBJECT	Standard		Infinity	0.0000	F_SILICA		0.0000	0.0000	0.0625	0.0000	-			
1	(aper)	Standard		Infinity	0.3510 V	F_SILICA		0.0625 U	0.0000	0.0625	0.0000	-			
2	STOP	Standard		Infinity	0.1419	F_SILICA P		0.0317	0.0000	0.0625	0.0000	-			
3		Standard		Infinity	0.0000	F_SILICA P		0.0445	0.0000	0.0625	0.0000	-			
4		Coordinate Break	Element Tilt		0.0000	-		0.0000	-	-		-	0.0000	0.0000	4.0000
5		Coordinate Break			0.0000	-		0.0000	-	-		-	0.0000	0.0000	45.0000
6		Biconic		Infinity	0.0000	MIRROR		0.0756	-	-	0.0000	0.0000	0.0000	0.0000	
7		Coordinate Break			0.0000 T	-		0.0000	-	-		-	0.0000	0.0000	45.0000 P
8		Coordinate Break	Element Tiltreturn		0.0000 P	-		0.0000	-	-		-	0.0000 P	0.0000 P	-4.0000 P
9		Standard		Infinity	0.0000	F_SILICA P		0.0455	0.0000	0.0455	0.0000	-			
10		Coordinate Break	Element Tilt		0.0000	-		0.0000	-	-		-	0.0000	0.0000 P	0.0000
11		Standard	Dummy	Infinity	-0.1238	F_SILICA P		0.0455	0.0000	0.0706	0.0000	-			
12		Biconic		0.1626 Z	0.1238 T			0.0706	-	-	0.3138 Z	0.0000	0.1238 P	0.0000	
13		Coordinate Break	Element Tiltreturn		-0.1238 P	-		0.0000	-	-		-	0.0000 P	0.0000	0.0000 P
14		Standard		Infinity	-0.1412 T			0.0726	0.0000	0.0726	0.0000	0.0000			
15		Standard		Infinity	0.0000			0.0898	0.0000	0.0898	0.0000	0.0000			
16	(aper)	Biconic		Infinity	-0.0450	F_SILICA P		0.2000 U	-	-	0.0000	-	0.2650	0.0000	
17	(aper)	Biconic		Infinity	-0.0960 T	WATER		0.2000 U	-	-	0.0000	-	0.3100	0.0000	
18		Standard		Infinity	0.0000 P	WATER		0.1024	0.0000	0.3000	0.0000	-			
19		Standard		Infinity	0.0000	WATER		0.1024	0.0000	0.3000	0.0000	-			
20	(aper)	Biconic		Infinity	-0.1270	1.34,0.0 M		0.3000 U	-	-	0.0000	0.0000	0.4064	0.0000	
21	(aper)	Biconic		Infinity	-0.9670 T	WATER		0.3000 U	-	-	0.0000	-	0.5334	0.0000	
22		Standard		Infinity	0.0000	WATER		0.2030	0.0000	0.2030	0.0000	-			
23	IMAGE	Standard		Infinity	-	WATER		0.2030	0.0000	0.2030	0.0000	-			

(b)

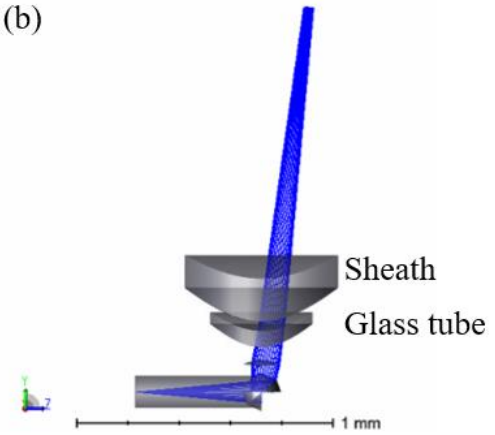

(c)

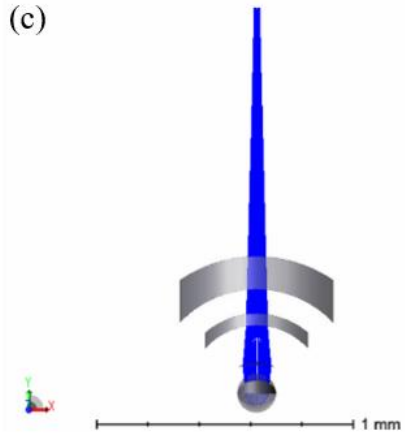

Figure 29. OpticStudio simulation of OCT endoscope. (a): Lens Data Editor. (b) 3D layout of OpticStudio model, sheath and glass tube are indicated. Saline and water are hidden in the layout for visualization. The ball lens shape is ellipsoid, but the visualization in OpticStudio doesn't shown correctly.

Ball lens was molded from surface 1 to surface 13. Surface 1 represents CLF and material is fused silica. The ellipsoid ball lens itself was modeled with biconic surface on surface 6 in Figure 29 (a), which was a surface with different curvature and conic in the orthogonal directions. In XY direction, the cross section is circle and conic parameter is 0 and the radius is semi-minor axis length. On the contrary, the cross section of YZ direction is ellipse with two parameters, radius and conic parameter, which were modeled with semi-major axis length and semi-minor axis length according to the following equations,

$$\frac{1}{c} = R = \pm\frac{b^2}{a} \tag{16}$$

$$k = -\varepsilon^2 = -[\frac{a^2 - b^2}{a^2}] \tag{17}$$

where a is the semi major axis length, b is the semi minor axis length, and k is the conic constant. The semi-major axis length and semi-minor axis length were defined on surface 2 and surface 11 in Figure 29 (a), which were used to determine distance between surfaces. Radius of ball lens and conic constant were respectively calculated based on the semi-major axis length and semi-minor axis length by macro. The optical axis was tilted and modeled with two pairs of coordinate breaks to represent polished surface (surface 5 and 7, and surface 4 and 8), both of which was for 41-degree polished surface and the 2nd of which itself was also for tolerance analysis discussed later.

Sheath and glass tube were also modeled with biconic surface. The cross section of XY direction was planar and the cross section of YZ direction was circle. The thickness on surface 12 indicating silica tube inner surface was solved maintaining the “z” distance from surface 6. With the configuration editor, thickness on surfaces 12, 14 and 17 were also solved which will be discussed later.

For more accurate simulation of Gaussian light propagation from DCF or SMF, Physical Optics Propagation (POP) was used to simulate for OCT endoscope. OpticStudio has ray-based diffraction computations, but they are simplified approximation which complex amplitude wavefronts are calculated according to rays transmitting through the optical system. However, the approximation doesn't work well within intermediate focus with truncation or collimated beam. On the contrary, POP is capable of providing accurate computation with all information, such as waist radius, beam waist position, and Rayleigh Range along orthogonal directions, which are important parameters for OCT design discussed in Chapter 2.

The endoscope cannot be guaranteed in the middle of the housing and artery, so 5 different configurations were modeled with configuration editor and 2 typical configurations are illustrated in Figure 30. Due to the gap between torque coil OD of 0.45mm and silica tube ID of 0.53mm, the distance between torque coil and silica tube is any possible value between +0.036mm to -0.036mm. Also, the distance between silica tube and housing is from +0.096mm to -0.096mm, due to the gap between silica tube OD of 0.62mm and housing ID of 0.812mm. More detailed tolerance between each component was also analyzed in tolerance study.

(a)

	Active : 1/5		Config 1*	Config 2	Config 3	Config 4	Config 5
1	THIC	15	0.0000	-0.0360	-0.03...	0.0360	0.0360
2	THIC	19	0.0000	-0.0960	0.0960	-0.09...	0.0960
3	THIC	22	0.0000	0.0000	0.0000	0.0000	0.0000

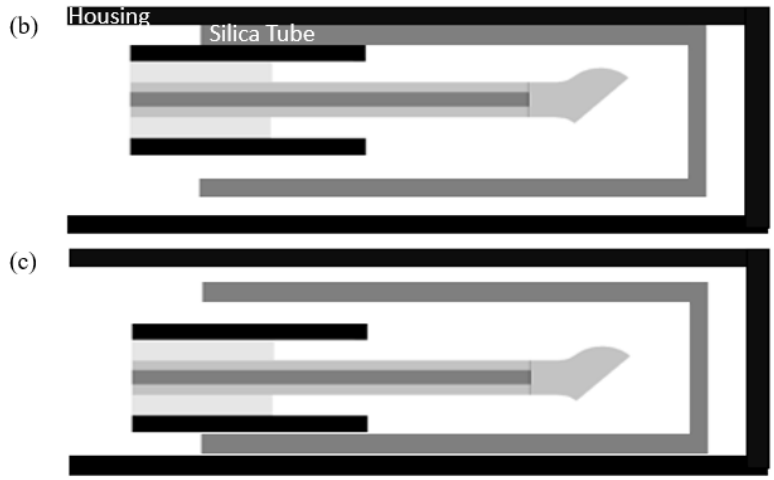

Figure 30. OCT endoscope configuration settings. (a): Configuration editor. (b) Config 2 typical drawing, endoscope, silica tube and catheter housing are adjacent to each on one side. (c) Config 5 typical drawing, endoscope, silica tube and catheter housing are adjacent to each on the other side.

Ball lens was optimized for 5 configurations and optimization editor of configuration 1 was shown in the Figure 31. Physical Optics Propagation Data (POPD) operand extracted POP outputs, including waist position, Rayleigh range, and waist radius in XY section and YZ section, represented on row 1 to row 8 in merit function editor shown in Figure 31. Ball lens shape was constrained with Vytran production capability, including maximum and minimum semi major axis length, semi minor axis length and polishing distance, on row 9 to row 15 in Figure 31. The gap between semi major axis length and semi minor axis length was also constrained partially which could be longer than 20um with tight tolerance on row 16 to row 19 in Figure 31.

Then XY direction and YZ direction optimization process were written respectively. OCT resolution is calculated as 1.18 times of beam waist radius and were optimized to be smaller than

40 μm. Waist position simulated by POPD was originally referenced to image surface defined in POP editor and the was re-referenced to fiber axis. Axial FOV was simulated by waist position and Rayleigh Range, and the area of interest should be covered. XY direction was optimized and constrained from row 20 to row 44 and YZ direction was optimized and constrained from row 45 to row 61 respectively. Also, the waist gap between XY section and YZ section was also optimized to <0.4mm on row 62 to row 64 in Figure 31.

	Type	Op#	Cfg#							Target	Weight	Value	% Contrib
1	CONF	1											
2	BLNK	3 and 6 are position, 4 and 7 are Rayleigh, 5 and 8 are 1/e2 waist radius											
3	POPD	0	0	0	5	0.0000	0.0000			0.0000	0.0000	0.2678	0.0000
4	POPD	0	0	0	6	0.0000	0.0000			0.0000	0.0000	2.1872	0.0000
5	POPD	0	0	0	7	0.0000	0.0000			0.0000	0.0000	0.0263	0.0000
6	POPD	0	0	0	8	0.0000	0.0000			0.0000	0.0000	0.7065	0.0000
7	POPD	0	0	0	9	0.0000	0.0000			0.0000	0.0000	1.3039	0.0000
8	POPD	0	0	0	10	0.0000	0.0000			0.0000	0.0000	0.0203	0.0000
9	BLNK	Constrain the size of ball lens											
10	MXCG	2	2							0.1420	1.0000E+06	0.1420	0.0000
11	MNCG	2	2							0.1000	-1.0000E+05	0.1000	0.0000
12	MXCG	3	3							1.0000E-02	-1.0000E+05	1.0000E-02	0.0000
13	MNCG	3	3							-1.0000E-02	-1.0000E+05	-1.0000E-02	0.0000
14	MXCG	11	11							-0.0850	-1.0000E+05	-0.0850	0.0000
15	MNCG	11	11							-0.1240	1.0000E+06	-0.1240	0.0000
16	TTHI	2	3							0.0000	0.0000	0.1419	0.0000
17	TGTH	11	12							0.0000	0.0000	0.1238	0.0000
18	DIFF	16	17							0.0000	0.0000	0.0181	0.0000
19	OPLT	18								0.0200	1.0000E+05	0.0200	0.0000
20	BLNK	X direction, radial section											
21	BLNK	Constrain the waist position											
22	CONS									1.5000	0.0000	1.5000	0.0000
23	SUMM	3	22							0.0000	0.0000	1.7678	0.0000
24	OPLT	23								3.0000	1.0000	3.0000	0.0000
25	OPGT	23								1.0000	1.0000	1.0000	0.0000
26	BLNK	Calculate resolution											
27	PROB	5	1.1800							0.0000	0.0000	0.0310	0.0000
28	OPLT	27								0.0400	10.0000	0.0400	0.0000
29	BLNK	Calculate the axial field of view											
30	DIFF	23	4							0.0000	0.0000	-0.4194	0.0000
31	SUMM	23	4							0.0000	0.0000	3.9550	0.0000
32	CONS									1.0000	0.0000	1.0000	0.0000
33	CONS									3.5000	0.0000	3.5000	0.0000
34	MCOV	1	1							0.0000	0.0000	0.0000	0.0000
35	MCOV	2	1							0.0000	0.0000	0.0000	0.0000
36	SUMM	34	35							0.0000	0.0000	0.0000	0.0000
37	BLNK	Clostest boudary FOV is closer to ball lens than required distance											
38	DIFF	32	36							0.0000	0.0000	1.0000	0.0000
39	DIFF	38	30							0.0000	0.0000	1.4194	0.0000
40	OPGT	39								0.0000	100.0000	0.0000	0.0000
41	BLNK	Farthest bo											
42	DIFF	33	36							0.0000	0.0000	3.5000	0.0000
43	DIFF	31	42							0.0000	0.0000	0.4550	0.0000
44	OPGT	43								0.0000	100.0000	0.0000	0.0000
45	BLNK												
46	BLNK	Y direction, longitudinal Section											
47	SUMM	6	22							0.0000	0.0000	2.2065	0.0000
48	OPLT	47								2.5000	1.0000	2.5000	0.0000
49	OPGT	47								1.0000	1.0000	1.0000	0.0000
50	BLNK	Calculate resolution											
51	PROB	8	1.1800							0.0000	0.0000	0.0239	0.0000
52	OPLT	51								0.0400	10.0000	0.0400	0.0000
53	BLNK	Calculate the axial field of view											
54	DIFF	47	7							0.0000	0.0000	0.9026	0.0000
55	SUMM	47	7							0.0000	0.0000	3.5103	0.0000
56	BLNK	Clostest boudary FOV is closer to ball lens than required distance											
57	DIFF	38	54							0.0000	0.0000	0.0974	0.0000
58	OPGT	57								0.0000	100.0000	0.0000	0.0000
59	BLNK	Farthest boundary FOV is farther from ball lens than required distance											
60	DIFF	55	42							0.0000	0.0000	0.0103	0.0000
61	OPGT	60								0.0000	100.0000	0.0000	0.0000
62	BLNK	Astigmatism, gap between two focusing positions											
63	DIFF	23	47							0.0000	0.0000	-0.4387	0.0000
64	ABLT	63								0.4000	100.0000	0.4387	18.8676

Figure 31. OCT endoscope optimization editor.

Due to ball lens shape tolerance induced by Vytran fabrication capability, and manual fabrication tolerance induced by polishing and glue, the optimal ball lens dimension also need to be carefully analyzed to avoid affecting optical performance, which is shown in Figure 32. Zemax provides a flexible and useful tolerance and sensitivity analysis capability, including variations in specific parameters settings. Monte Carlo analysis estimated the aggregate performance considering all tolerance effects by a series of random combination with specified tolerances for each one. Each tolerance parameter was measured by large amount of endoscope fabrication process and Gaussian distribution was estimated. Ball lens size tolerance, including total length, semi-major and semi-minor axis lengths are defined in line 1-3. Polishing related tolerance, such as polishing angle and polishing depth are defined in line 4 and line 5. Assembly tolerance between fiber axis and silica tube are defined in line 6 – 9.

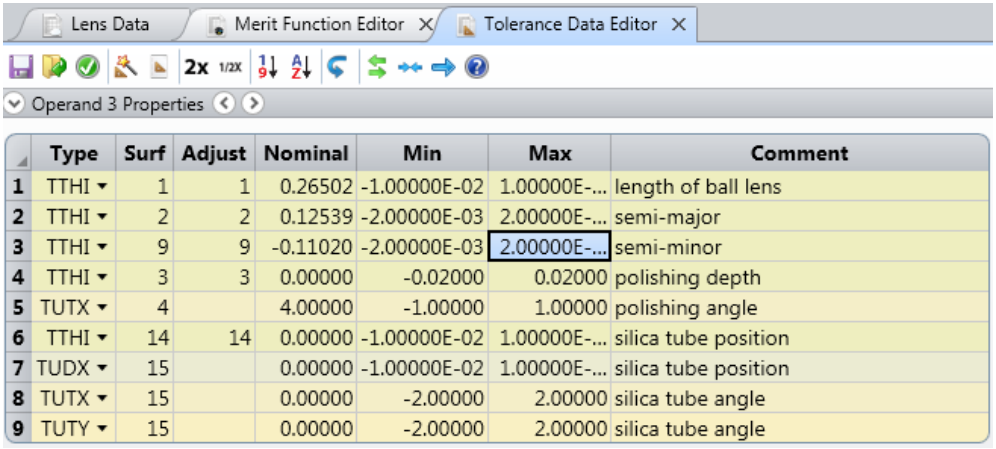

	Type	Surf	Adjust	Nominal	Min	Max	Comment
1	TTHI	1	1	0.26502	-1.00000E-02	1.00000E-...	length of ball lens
2	TTHI	2	2	0.12539	-2.00000E-03	2.00000E-...	semi-major
3	TTHI	9	9	-0.11020	-2.00000E-03	2.00000E-...	semi-minor
4	TTHI	3	3	0.00000	-0.02000	0.02000	polishing depth
5	TUTX	4		4.00000	-1.00000	1.00000	polishing angle
6	TTHI	14	14	0.00000	-1.00000E-02	1.00000E-...	silica tube position
7	TUDX	15		0.00000	-1.00000E-02	1.00000E-...	silica tube position
8	TUTX	15		0.00000	-2.00000	2.00000	silica tube angle
9	TUTY	15		0.00000	-2.00000	2.00000	silica tube angle

Figure 32. OCT endoscope tolerance editor. Ball lens size tolerance, including total length, semi-major and semi-minor axis lengths are defined in line 1-3. Polishing related tolerance, such as polishing angle and polishing depth are defined in line 4 and line 5. Assembly tolerance between fiber axis and silica tube are defined in line 6 – 9.

6.1.2 Simulation of FDFLIM Endoscope

General MMF simulation method was illustrated in Chapter 4 and the specific DCF simulation method was illustrated in Chapter 5. The preferred ball lens for OCT was simulated and optimized with Zemax illustrated in the previous section and then analyzed the optical performance for FLIM system with the method illustrated in Chapter 5.

6.1.3 Endoscope Fabrication

A fiber preparation and splice workstation (FFS2000, Vytran) was used for endoscope fabrication. The 1.55-meter OCTFLIM endoscope was constructed starting with a DCF (SM-9/105/125-20A, Nufern). The DCF was fusion spliced to a MMF (FG105UCA, Thorlabs). MMF was cleaved to a precise length and then fusion spliced to a CLF (HCF-125-47, Coractive). Following splicing, the CLF was cleaved to a precise length, heated and shaped into an ellipsoid ball with predetermined semi-principal axes in the tungsten filament furnace of the workstation, shown in Figure 33. The ellipsoidal shape was designed to compensate for the astigmatism caused by the toroidal shape of the catheter sheath and the silica tube used to cover and protect the fiber endoscope. The distal ball lens was polished with an angle of 41° using a commercial fiber polisher (69-3000-160, Buehler) with custom modifications to enable ball lens polishing at precise angles for side viewing endoscopes. The 41° angle was chosen so that total internal reflection (TIR) would occur at the polished glass-air interface, hence obviating the need for reflective coatings on the polished surface. In addition to the angle, precise control of the polishing depth from unpolished ball is necessary in order to achieve good performance.

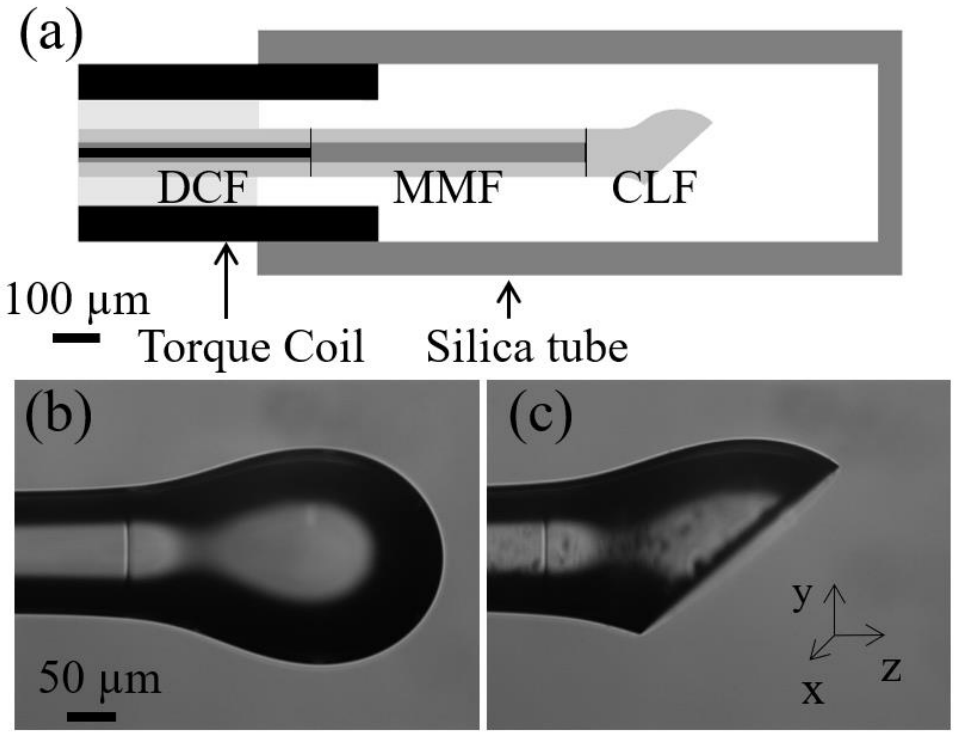

Figure 33. Schematic drawing of OCT/FLIM endoscope. a: Schematic drawing of the catheter. Heated and shaped CLF fusion spliced with a MMF and then with a DCF, and the fiber was glued with torque coil and silica tube. Torque Coil's ID is 270 μm and OD is 450 μm. Silica Tube's ID is 530 μm and OD is 620 μm. Scale bar: 100 μm. DCF: double clad fiber. MMF: multimode fiber. CLF: coreless fiber. b: Side view of the fabricated ball lens before polishing. Heated and shaped CLF fusion spliced to a MMF (DCF was not shown due to small FOV of machine). Scale bar: 50 μm. c: Side view of the ball lens after polishing by customized fiber polishers. The polishing angle is 41°.

The fiber endoscope was then enclosed in a customized torque coil (ASAHI INTECC) with high-speed torque transmission and high flexibility. The OD of the torque coil is 450 μm and the ID is 270 μm. The proximal end was connectorized with a custom FC/APC connector and strain relief boot, mating to a custom broadband fiber optic rotary joint [69]. The distal end was covered by a laser-cut silica tube (TSP530620, Polymicro) with an outer diameter of 620 μm and an inner diameter of 530 μm. The silica tube serves both to protect the ball lens and preserve the air-glass interface at both the flat polished and curved surfaces of the endoscope even when submerged.

The ID of silica tube was chosen so that the torque coil could fit inside and therefore make a strong bond between the two. Using a smaller diameter for the silica tube would unnecessarily increase the astigmatism introduced by the tube. The fiber endoscope was inserted into the home-made flexible housing with ID of 0.812 mm and 1.066 mm.

6.1.4 OCT/FLIM Instrumentation

A schematic diagram of the dual-modality imaging system is shown in Figure 34. The diagram can be divided into the OCT module, FLIM module and Common Path. The Common Path refers to the portion of the optical system which is common to both OCT and FLIM, i.e. the respective beams are co-propagating.

6.1.4.1 OCT module

A fiber-based swept-source OCT system was implemented as the OCT module. The light source was a fiber-coupled wavelength-tunable laser (ESS-1310nm-100kHz, Exalos) with a center wavelength of 1310 nm and a spectral bandwidth of 100 nm. The light exited the laser via a single-mode fiber (SMF-28e, Corning) and was coupled into a 90:10 fiber coupler, directing 90% to the sample arm and 10% to the reference arm. The sample arm light was directed to a circulator and then on to the rotary joint and endoscope, as described below. The backscattered light exiting port 3 (P3) of the circulator was recombined with the reference arm (P3) in a standard 2x2 (50:50 C) fiber coupler.

It is well known that, rotating catheter endoscopes, as described here, generate fluctuations in the light polarization in the sample arm. In order to overcome this, polarization diverse detection was implemented[85]. The two outputs of the 2x2 coupler (50:50 C) that combined the reference and sample arm were each coupled into a polarizing 1x2 coupler (P2, PBS-31-P-2-L-3-1, General Photonics). The s-polarization from each coupler was input into one balanced photodiode detector

and the p-polarization to the other. In order to have equal reference s- and p-polarization intensity the reference arm light was adjusted with a set of polarization paddles. The signal from the two balanced photodiode detectors (WL-BPD600MA, Wieserlabs UG) were digitized at 200 MS/s simultaneously using an acquisition card NI-5772 (800MS/s, 12-Bit, 2-Channel Digitizer Adapter) with an inline FPGA (NI, PXIe-7966). The signal from a reference interferometer was used to calibrate the laser sweep once before each imaging session before the experiment. The A-line was taken as the vector sum of the two channels, i.e. $s = \sqrt{s_1^2 + s_2^2}$, where sn is the amplitude of the corresponding FFT. This served to minimize the modulation of the A-line amplitude due to polarization variations. The sample arm of the interferometer will be described in the Common Path section below.

6.1.4.2 FLIM module

The FLIM module was similar to that described in the previous paper[86]. A fiber-based diode laser (iBeam-SMART-375-S, Toptica) with a modulation of up to 250 MHz was used as an excitation light source for FLIM. The excitation/emission light co-propagates with the OCT light as discussed below, in Common Path. The fluorescence emission exiting the common path was directed into the multispectral detection module by a dichroic mirror (DM2) (FF376-Di01-25x36, Semrock). A short, semi-arbitrary length of 200 μm MMF (FG200UEA, Thorlabs) was used to transmit light to the fluorescence detection system. After transmitting through the ~0.4 m of MMF, the emission was directed into a multi-spectral detection system, with a set of dichroic mirrors (D3, ZT405rdc; D4, ZT488rdc; D5, T560LPXR, Chroma) and bandpass filters (F1: ZET405/20x, Semrock; F2: FF-1-440/40; F3, FF03-525/50, Chroma) to divide the emission into three bands (Ch1 405/20, Ch2 440/40 and Ch3 525/50). Each channel had its own pre-amplifier (ZFL-500LN+,

Mini Circuits) and APD (C12702-11, Hamamatsu) detector. Outputs from the 3 APDs were digitized at 250 MS/s with 14-bit resolution and processed on an FPGA (NI5761 and PXIe7962, National Instruments).

The digitized time-domain fluorescence signal was processed in the following way. A discrete Fourier transform was calculated at 1.25, 20.83, 41.67, 62.50, and 83.33 MHz. Then a background fluorescence signal was subtracted before computing the phase and modulation lifetimes. The background was measured by recording the FLIM image without a sample (i.e. an air sample) and taking the mean of the entire image. In order to compensate for the system response, fluorescence from POPOP was recorded as a standard (τ=1.35 ns) and used to calculate correction factors which were applied directly to the phase and modulation lifetimes. The DFT was performed on the FPGA while all other processing was performed on the host computer.

6.1.4.3 Common Path

The OCT sample arm light and FLIM excitation light were combined by a dichroic mirror DM1 (FF700-SDi01-25x36, Semrock) and then coupled into a double clad fiber with an off-axis parabolic reflective collimator, L4 in Figure 34 (RC04APC-F01, Thorlabs). The parabolic reflective collimator was chosen to mitigate chromatic aberration over this extremely wide bandwidth of light source (375nm – 1360nm). The coupling efficiency was 79% for 1310 nm light into the single mode core and 87% for the 375 nm FLIM excitation light into the inner cladding. The fiber endoscope, described above, was connected to an ultra-broadband lensless fiber optic rotary joint[69]. The lensless rotary joint achieved very low insertion loss and noise variance (less than 0.2 dB) even at high rotational velocity (8800 revolution per minute, rpm).

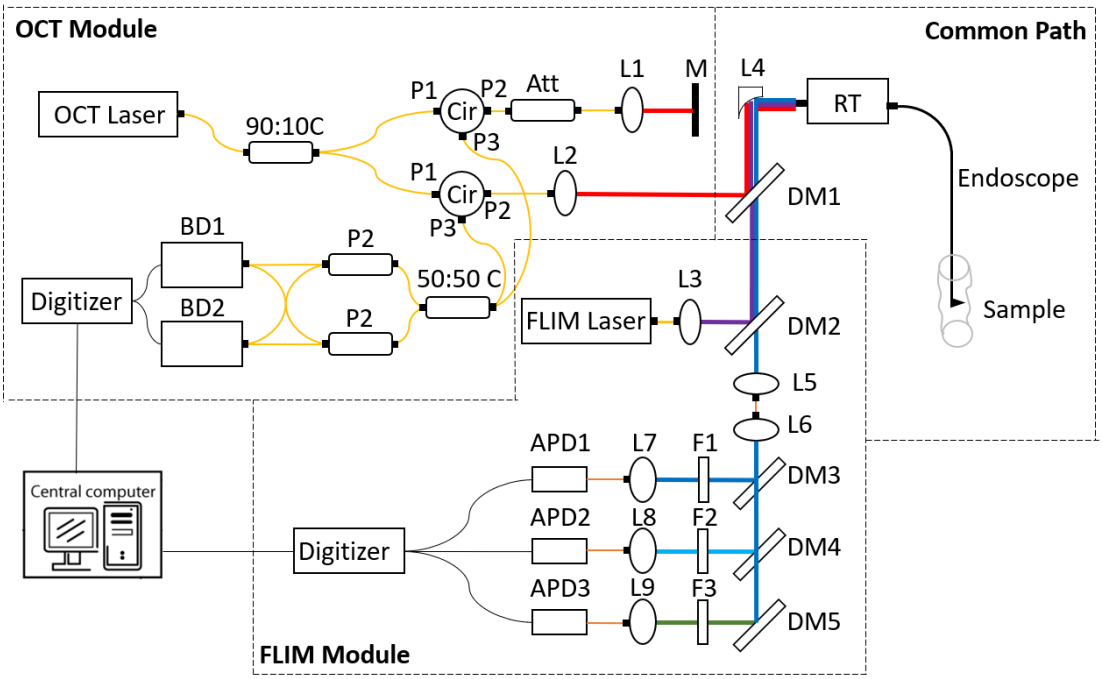

Figure 34. Schematic diagram of the dual-modality imaging system, including OCT Module, FLIM Module and Common Path. L1-L3, L7-L9: free-space collimation and coupling lenses, L4, reflective collimator, L5, L6: fiber-connected collimation and coupling lenses. M: mirror, DM1 – DM5: dichroic mirrors, F1-F3: bandpass filters, PL: polarizer, BD: balanced detectors, Cir: circulators, P1-P3: circulator port 1 - 3, APD1-APD3: avalanched photodiodes, RT: rotary joint. Orange line indicates MMF fiber transmission. Yellow line indicates SMF transmission. Other thick colored lines indicate free-space transmission. Black thin line indicates electrical line.

6.1.5. Tissue Preparation and Imaging

Human coronary artery segments were obtained from autopsy cases within 3 days of the time of death, according to a protocol approved by the Texas A&M University Institutional Review Board. The arterial segment was imaged by placing the endoscope inside the lumen of the artery performing a pullback. Immediately after imaging, each segment was ink marked for correlation with histopathology, fixed in 10% formalin, and sent for histopathology analysis. Each image plaque segment was consecutively sectioned every 1 mm. The sections were stained with Movat pentachrome and CD68 staining and evaluated by a cardiovascular pathologist.

6.2 Results and Discussion

In order to validate the performance of the developed intravascular OCT/FLIM system, measurements and simulations were completed on the optical and mechanical functionality.

6.2.1 Resolution Testing and Mechanical Testing

We developed the following methodology to reliably measure and manipulate the beam profile from DCF. A 1310 nm laser (LPS-1310-FC, Thorlabs) was coupled into the end of DCF endoscope. The DCF endoscope tip was securely placed inside fiber rotator (HFR007, Thorlabs) so that the beam went to the side of the endoscope. The beam profiler (BP104-IR, Thorlabs) was mounted on a translation stage and positioned perpendicular to the output of the fiber endoscope so that beam profile could be measured at several distances along the optical axis.

The measured beam profile of polished endoscope was measured at different places and then fitted according to Gaussian beam propagation equation and compared with simulation result, and a representative profile at each interval is shown in Figure 35. The dashed lines are the Gaussian fits for the measurement dots in two sections. The beam profiles from the endoscope with silica tube and endoscope housing were also measured and compared with simulation. The measurement confirmed the polished OCT endoscope simulation matched the measurement, and that biconvex surface or non-circularly asymmetrical surface could be accurately simulated which would also work for glass tube and catheter housing which were not included inside this experiment due to high fabrication tolerance.

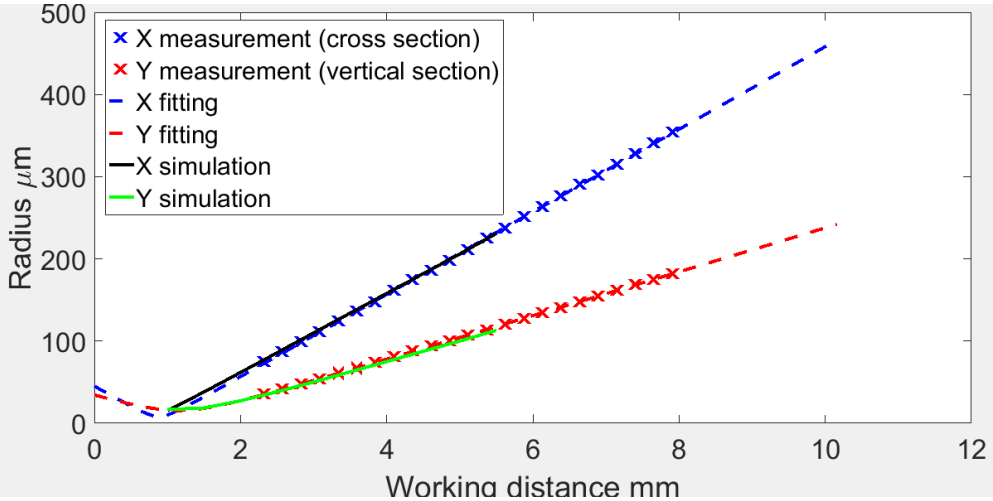

Figure 35. OCT simulation and measurement. The dashed lines are the Gaussian fits for the measurement dots in two sections, black and green lines are simulation results.

6.2.2 Ex Vivo Human Coronary Artery and Histology Analysis

Finally, we imaged a segment of human coronary artery obtained from autopsy. The catheter endoscope was inserted into the flexible catheter which was then placed in the artery lumen. A pullback at 1.87 mm/s was performed at a rotational velocity of 3000 rpm. Representative OCT image and overlapped fluorescence lifetime map are shown in Figure 36 and Figure 37. After completing imaging, the artery segment was fixed in formalin and sent for histopathology processing.

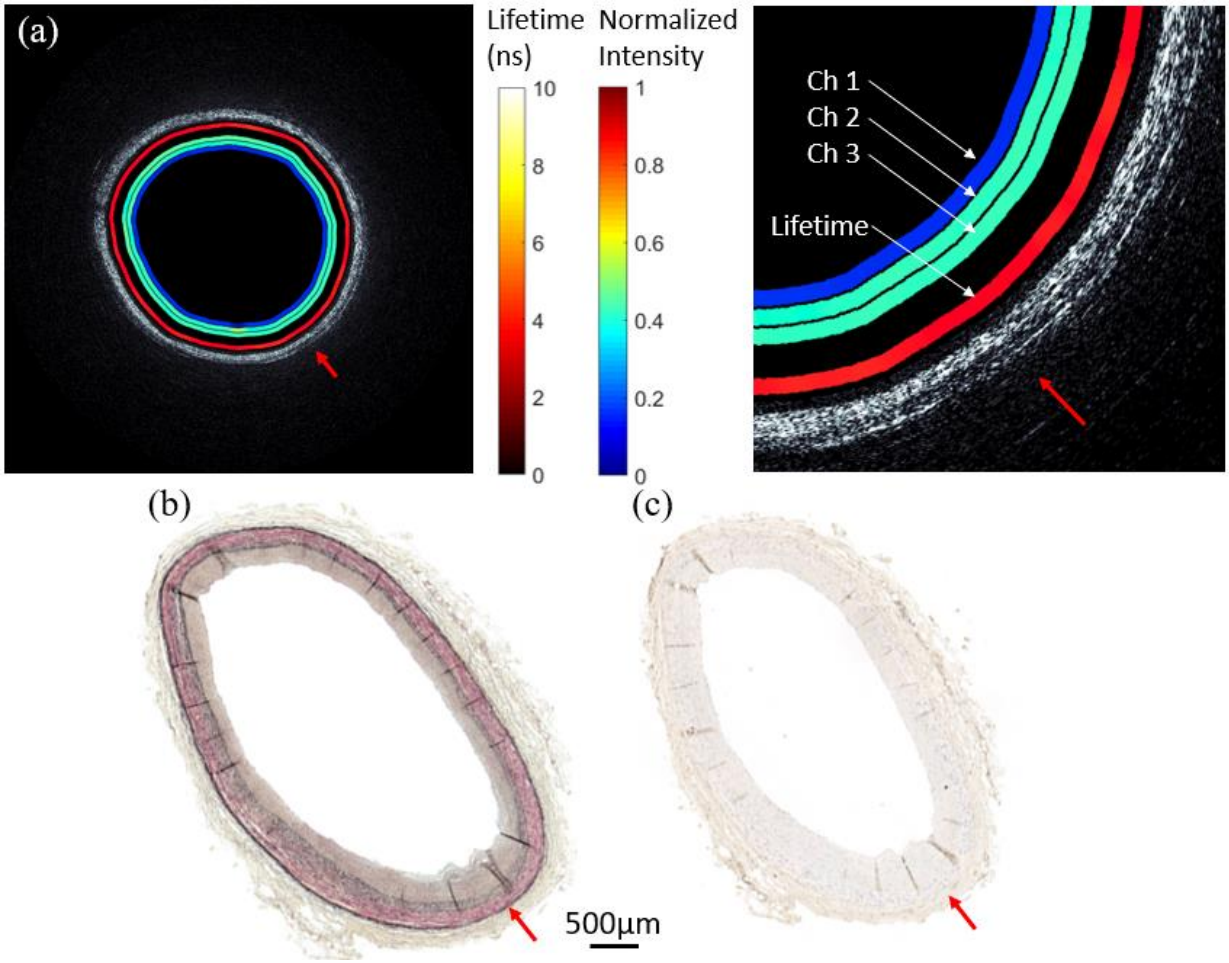

Figure 36. OCT/FLIM imaging and histology analysis example 1. (a) OCT/FLIM cross-sectional image of ex vivo of human coronary artery obtained from autopsy. The OCT is rendered in gray scale. The four color rings on the inside of the lumen are from inner to outer normalized intensity maps from channels 1, 2, 3 and lifetime map (channel 3 at 40 MHz). (b) Histopathology result (Movat staining) and (c). Histopathology result (CD68 staining). Red arrow provides a point of reference for all four images.

The histopathology (Figure 36) indicates a fibrotic plaque rich in collagen and smooth muscle cells around the entire lumen with no observable macrophage infiltration. IVOCT figure shows a layered architecture, with highly backscattering intima and adventitia and low backscattering media. The intima area is region of thickened collagen which has lifetime of ~5ns.

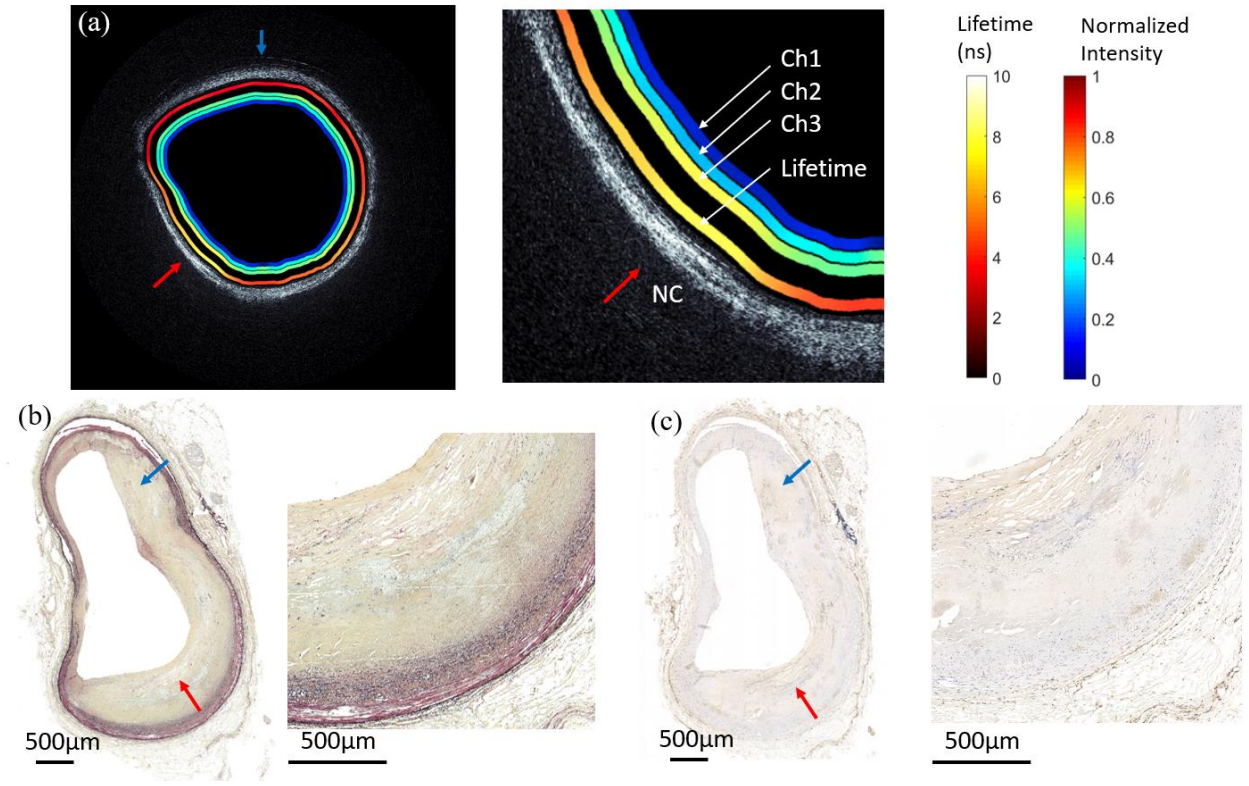

Figure 37. OCT/FLIM imaging and histology analysis example 2. (a) OCT/FLIM cross-sectional image of ex vivo of human coronary artery obtained from autopsy. The OCT is rendered in gray scale. The four color rings on the inside of the lumen are from inner to outer normalized intensity maps from channels 1, 2, 3 and lifetime map (channel 3 at 40 MHz). (b) Histopathology result (Movat staining) and (c). Histopathology result (CD68 staining). Red arrow points at a fibroatheroma with a thick cap and a small necrotic core (shown in zoomed view). Blue arrow points at the thickened intima.

The histopathology of the second artery sample (Figure 37) shows a fibroatheroma with a thick cap rich in collagen and smooth muscle cell covering a small necrotic (NC) (RED arrow on Figure 37.b) showing extensive macrophage infiltration (RED arrow on Figure 37.c). The region next to the fibroatheroma shows a thickened intima rich in collagen (BLUE arrow on Figure 37.b) and minimal macrophage infiltration (BLUE arrow on Figure 37.c). The OCT figure overlapped with FLIM lifetime map show two distinct regions resembling: a) a region (blue arrow) of

thickened collagen (homogeneous IVOCT signal low signal drop-off and fluorescence lifetime ~5ns), and b) a region (red arrow) of combination of collagen and lipid (a fast IVOCT signal drop-off and fluorescence lifetime > 6ns[87]) reflecting the presence of the lipid rich necrotic core and macrophage.

6.3 Conclusions

In conclusion, we have developed a dual-modality intravascular swept-source OCT and frequency-domain FLIM catheter system in order to capture both structural and biochemical information on atherosclerotic plaques. We demonstrated a combined simulation and measurement approach for designing ball lens endoscopes that could be applied to a wide range of ball sizes using any available DCF. This approach enables careful optimization of the design before fabrication and allows us to simulate the performance of the endoscope in environments where it is not practical to make direct measures of optical properties, such as the coronary artery with a saline flush. We demonstrated that the resolution of the FLIM system could be tuned by varying the relative power distributed to the core and inner cladding. With UV excitation, this approach is confounded by solarization of the optical fiber which introduces significant optical loss. This can be overcome by either using a higher power light source to compensate for solarization losses or utilizing longer wavelengths for excitation to avoid solarization.

We have experience developing and using both time-domain and frequency domain FLIM systems for imaging atherosclerotic plaques. We believe that the frequency domain approach offers key advantages over time-domain systems. The ability to achieve higher spatial resolution and tune that resolution could enable more detailed images of the plaques. While we did not demonstrate it here, in principle it should be possible to use higher average power for excitation because the peak power is orders of magnitude lower. This should translate to higher signal to

noise. Finally, in our experience the system cost is substantially lower for frequency domain systems[86] compared to time domain systems we have developed before[88]. This is important if the technology is to be translated to the clinic.

7. DISCUSSION

In this dissertation, a dual-modality OCT-FLIM imaging system was built and three types of ball lens-based endoscopes were designed and fabricated. The 1st endoscope based on MMF was designed for TDFLIM system, the 2nd endoscope based on DCF was designed for FDFLIM system, and the 3rd endoscope based on DCF was designed for SSOCT and FDFLIM system.

Using different types endoscope and respective optical imaging system, we imaged post mortem human coronary artery ex vivo. Results were presented to support the validation of the system and capability for imaging atherosclerosis. In addition, the simulation and design process for endoscopes could be used for design and fabrication ball lens-based endoscope for cochlear and rigid endoscope for FLIM for oral cancer.

Atherosclerosis is the leading cause of morbidity and mortality and requires more information for understanding progression and developing treatment. The Swept-Source OCT and Frequency-Domain FLIM system could provide morphological and biochemical information of atherosclerosis, which would help and improve the atherosclerosis diagnosis.

Some of the limitations of the current OCT-FLIM system was the SNR of the whole system is not good enough for in vivo imaging and the supporting accessories were readily designed for in vivo imaging. Also, ball lens-based endoscope fabrication process could control tolerance which would affect optical performance and fabrication yield.

Future work includes improvement of the endoscope design and fabrication process. With 3D printing technology, the tolerance could be controlled more easily and optical performance will be improved a lot with the help of robust and convenient optical simulation. Also, the supporting accessories should be developed including robust catheter housing to be inserted and pulled back inside artery.

A few limitations should be overcome too for better optical performance. First, the DCF with low auto-fluorescence which is resistant to solarization should be developed with vendor, and it will improve the resolution of the FLIM system a lot by allowing more power transmitting through the core. Second, the rotary joint with high coupling efficiency and convenient alignment should be developed, and it will help couple light through smaller core which is not well supported and also help transform the research to industry.

8. SUMMARY

Research in biomedical optical imaging focuses on research and application on technique for non-invasively or minimally invasive optical imaging method for diseases. Atherosclerosis is the leading cause of morbidity and mortality in the United States and other industrialized countries. In general, diagnostical imaging system detect the biomarkers of atherosclerosis, and a few biomarkers have been identified which is related with progression. Because the atherosclerosis is complex, combination of two imaging modalities has been adopted by a number of groups to increase sensitivity and specificity for characterization. Future development of treatment for atherosclerosis also will depend on a more detailed understanding of plaque development.

The goal of the project is to develop a development of ball-lens based endoscope for Optical Coherence Tomography and Fluorescence Lifetime Imaging Microscopy system for intravascular disease diagnosis and detection in-vivo. OCT provides high resolution morphological information of atherosclerosis. On the contrary, FLIM provides biochemical information based on tissue fluorophores. The dual-modality OCT and FLIM system was designed and developed. The OCT subsystem is designed to have a scan depth of more than 1mm with high axial resolution, fast scanning speed and large enough field of view. The FLIM subsystem is designed to have a good lateral resolution of smaller than 100 μm while collecting emission from the tissue. The shared common path is also developed to combine both optical imaging systems with high efficiency and to be compatible with endoscope.

Also, a general simulation, fabrication, and measurement method for ball lens-based endoscope based on MMF, SMF, and DCF. Different optical propagation algorithm was analyzed and the optimal optical simulation models were proposed according to different applications. The fabrication approach was also analyzed and standard operating process was proposed to minimize

fabrication duration and tolerance. Finally, the measurement method and setup were alsso prepared to validate the simulation and fabrication process.

Future work for this project involves in vivo imaging of atherosclerosis and classification of atherosclerosis according to OCT-FLIM images.

REFERENCES

1. E. J. Benjamin, S. S. Virani, C. W. Callaway, A. M. Chamberlain, A. R. Chang, S. Cheng, S. E. Chiuve, M. Cushman, F. N. Delling, and R. Deo, "Heart disease and stroke statistics—2018 update: a report from the American Heart Association," Circulation **137**, e67-e492 (2018).

2. W. G. MEMBERS, E. J. Benjamin, M. J. Blaha, S. E. Chiuve, M. Cushman, S. R. Das, R. Deo, S. D. de Ferranti, J. Floyd, and M. Fornage, "Heart disease and stroke statistics—2017 update: a report from the American Heart Association," Circulation **135**, e146 (2017).

3. R. Ross, "Pathogenesis of Atherosclerosis-Atherosclerosis is an inflammatory disease," Am. Heart J. **138**, S419 (1999).

4. K. Yahagi, F. D. Kolodgie, F. Otsuka, A. V. Finn, H. R. Davis, M. Joner, and R. Virmani, "Pathophysiology of native coronary, vein graft, and in-stent atherosclerosis," Nature Reviews. Cardiology **13**, 79 (2016).

5. P. Libby, P. M. Ridker, and A. Maseri, "Inflammation and atherosclerosis," Circulation **105**, 1135-1143 (2002).

6. J. F. Bentzon, F. Otsuka, R. Virmani, and E. Falk, "Mechanisms of plaque formation and rupture," Circulation research **114**, 1852-1866 (2014).

7. T. Seimon and I. Tabas, "Mechanisms and consequences of macrophage apoptosis in atherosclerosis," Journal of lipid research **50**, S382-S387 (2009).

8. R. Virmani, A. P. Burke, A. Farb, and F. D. Kolodgie, "Pathology of the vulnerable plaque," J. Am. Coll. Cardiol. **47**, C13-C18 (2006).

9. R. Virmani, J. Narula, M. B. Leon, and J. T. Willerson, *The vulnerable atherosclerotic plaque: strategies for diagnosis and management* (John Wiley & Sons, 2008).

10. M. O. Grootaert, M. Moulis, L. Roth, W. Martinet, C. Vindis, M. R. Bennett, and G. R. De Meyer, "Vascular smooth muscle cell death, autophagy and senescence in atherosclerosis," Cardiovascular research **114**, 622-634 (2018).

11. A. P. Burke, A. Farb, G. T. Malcom, Y.-h. Liang, J. E. Smialek, and R. Virmani, "Plaque rupture and sudden death related to exertion in men with coronary artery disease," Jama **281**, 921-926 (1999).

12. R. Virmani, F. D. Kolodgie, A. P. Burke, A. Farb, and S. M. Schwartz, "Lessons from sudden coronary death a comprehensive morphological classification scheme for atherosclerotic lesions," Arterioscler., Thromb., Vasc. Biol. **20**, 1262-1275 (2000).

13. A. J. Welch, M. J. van Gemert, and W. M. Star, "Definitions and overview of tissue optics," in *Optical-thermal response of laser-irradiated tissue* (Springer, 2010), pp. 27-64.

14. S.-J. Park, D.-W. Park, A. K. Jacobs, C. E. Jackson, J. R. Dalzell, and K. J. Hogg, "Contemporary Reviews in Interventional Cardiology," (2009).

15. J. T. Salonen and R. Salonen, "Ultrasound B-mode imaging in observational studies of atherosclerotic progression," Circulation **87**, II56-65 (1993).

16. S. L. Bridal, P. Fornès, P. Bruneval, and G. Berger, "Parametric (integrated backscatter and attenuation) images constructed using backscattered radio frequency signals (25–56 MHz) from human aortae in vitro," Ultrasound in medicine & biology **23**, 215-229 (1997).

17. V. Amirbekian, M. J. Lipinski, K. C. Briley-Saebo, S. Amirbekian, J. G. S. Aguinaldo, D. B. Weinreb, E. Vucic, J. C. Frias, F. Hyafil, and V. Mani, "Detecting and assessing macrophages in vivo to evaluate atherosclerosis noninvasively using molecular MRI," Proceedings of the National Academy of Sciences **104**, 961-966 (2007).

18. C. Yuan and W. S. Kerwin, "MRI of atherosclerosis," Journal of Magnetic Resonance Imaging **19**, 710-719 (2004).

19. C. Yuan, W. S. Kerwin, V. L. Yarnykh, J. Cai, T. Saam, B. Chu, N. Takaya, M. S. Ferguson, H. Underhill, and D. Xu, "MRI of atherosclerosis in clinical trials," NMR in Biomedicine **19**, 636-654 (2006).

20. M. J. Lipinski, V. Amirbekian, J. C. Frias, J. G. S. Aguinaldo, V. Mani, K. C. Briley‐Saebo, V. Fuster, J. T. Fallon, E. A. Fisher, and Z. A. Fayad, "MRI to detect atherosclerosis with gadolinium‐containing immunomicelles targeting the macrophage scavenger receptor," Magnetic resonance in medicine **56**, 601-610 (2006).

21. F. J. Van der Meer, D. J. Faber, D. M. B. Sassoon, M. C. Aalders, G. Pasterkamp, and T. G. van Leeuwen, "Localized measurement of optical attenuation coefficients of atherosclerotic plaque constituents by quantitative optical coherence tomography," Medical Imaging, IEEE Transactions on **24**, 1369-1376 (2005).

22. N. A. Patel, D. L. Stamper, and M. E. Brezinski, "Review of the ability of optical coherence tomography to characterize plaque, including a comparison with intravascular ultrasound," Cardiovascular and interventional radiology **28**, 1-9 (2005).

23. J. A. Schaar, C. L. de Korte, F. Mastik, R. Baldewsing, E. Regar, P. de Feyter, C. J. Slager, A. F. van der Steen, and P. W. Serruys, "Intravascular palpography for high-risk vulnerable plaque assessment," Herz **28**, 488-495 (2003).

24. H. Yabushita, B. E. Bouma, S. L. Houser, H. T. Aretz, I.-K. Jang, K. H. Schlendorf, C. R. Kauffman, M. Shishkov, D.-H. Kang, and E. F. Halpern, "Characterization of human atherosclerosis by optical coherence tomography," Circulation **106**, 1640-1645 (2002).

25. P. Wilder‐Smith, K. Lee, S. Guo, J. Zhang, K. Osann, Z. Chen, and D. Messadi, "In vivo diagnosis of oral dysplasia and malignancy using optical coherence tomography:

preliminary studies in 50 patients," Lasers in Surgery and Medicine: The Official Journal of the American Society for Laser Medicine and Surgery **41**, 353-357 (2009).

26. K. Arakawa, K. Isoda, T. Ito, K. Nakajima, T. Shibuya, and F. Ohsuzu, "Fluorescence analysis of biochemical constituents identifies atherosclerotic plaque with a thin fibrous cap," Arterioscler., Thromb., Vasc. Biol. **22**, 1002-1007 (2002).

27. J. Park, P. Pande, S. Shrestha, F. Clubb, B. E. Applegate, and J. A. Jo, "Biochemical characterization of atherosclerotic plaques by endogenous multispectral fluorescence lifetime imaging microscopy," Atherosclerosis **220**, 394-401 (2012).

28. M. Monici, "Cell and tissue autofluorescence research and diagnostic applications," Biotechnology annual review **11**, 227-256 (2005).

29. J. M. I. Maarek, L. Marcu, M. C. Fishbein, and W. S. Grundfest, "Time‐resolved fluorescence of human aortic wall: Use for improved identification of atherosclerotic lesions," Lasers Surg. Med. **27**, 241-254 (2000).

30. L. I. Laifer, K. M. O'Brien, M. L. Stetz, G. R. Gindi, T. J. Garrand, and L. I. Deckelbaum, "Biochemical basis for the difference between normal and atherosclerotic arterial fluorescence," Circulation **80**, 1893-1901 (1989).

31. J. Chen, C.-H. Tung, U. Mahmood, V. Ntziachristos, R. Gyurko, M. C. Fishman, P. L. Huang, and R. Weissleder, "In vivo imaging of proteolytic activity in atherosclerosis," Circulation **105**, 2766-2771 (2002).

32. L. Marcu, J. A. Jo, Q. Fang, T. Papaioannou, T. Reil, J.-H. Qiao, J. D. Baker, J. A. Freischlag, and M. C. Fishbein, "Detection of rupture-prone atherosclerotic plaques by time-resolved laser-induced fluorescence spectroscopy," Atherosclerosis **204**, 156-164 (2009).

33. G. J. Ughi, H. Wang, E. Gerbaud, J. A. Gardecki, A. M. Fard, E. Hamidi, P. Vacas-Jacques, M. Rosenberg, F. A. Jaffer, and G. J. Tearney, "Clinical characterization of coronary atherosclerosis with dual-modality OCT and near-infrared autofluorescence imaging," JACC: Cardiovascular Imaging (2016).

34. H. Wang, J. A. Gardecki, G. J. Ughi, P. V. Jacques, E. Hamidi, and G. J. Tearney, "Ex vivo catheter-based imaging of coronary atherosclerosis using multimodality OCT and NIRAF excited at 633 nm," Biomedical optics express **6**, 1363-1375 (2015).

35. J. K. Barton, F. Guzman, and A. Tumlinson, "Dual modality instrument for simultaneous optical coherence tomography imaging and fluorescence spectroscopy," Journal of biomedical optics **9**, 618-623 (2004).

36. J. Park, J. A. Jo, S. Shrestha, P. Pande, Q. Wan, and B. E. Applegate, "A dual-modality optical coherence tomography and fluorescence lifetime imaging microscopy system for

simultaneous morphological and biochemical tissue characterization," Biomedical optics express **1**, 186-200 (2010).

37. J. Bec, H. Xie, D. R. Yankelevich, F. Zhou, Y. Sun, N. Ghata, R. Aldredge, and L. Marcu, "Design, construction, and validation of a rotary multifunctional intravascular diagnostic catheter combining multispectral fluorescence lifetime imaging and intravascular ultrasound," J. Biomed. Opt. **17**, 1060121-10601210 (2012).

38. X. Li, J. Li, J. Jing, T. Ma, S. Liang, J. Zhang, D. Mohar, A. Raney, S. Mahon, and M. Brenner, "Integrated IVUS-OCT imaging for atherosclerotic plaque characterization," Selected Topics in Quantum Electronics, IEEE Journal of **20**, 196-203 (2014).

39. A. J. Beer, J. Pelisek, P. Heider, A. Saraste, C. Reeps, S. Metz, S. Seidl, H. Kessler, H.-J. Wester, and H. H. Eckstein, "PET/CT imaging of integrin αvβ3 expression in human carotid atherosclerosis," JACC: Cardiovascular Imaging **7**, 178-187 (2014).

40. M. A. Bruckman, K. Jiang, E. J. Simpson, L. N. Randolph, L. G. Luyt, X. Yu, and N. F. Steinmetz, "Dual-modal magnetic resonance and fluorescence imaging of atherosclerotic plaques in vivo using VCAM-1 targeted tobacco mosaic virus," Nano letters **14**, 1551-1558 (2014).

41. F. Sharif and R. T. Murphy, "Current status of vulnerable plaque detection," Catheter Cardiovasc Interv **75**, 135-144 (2010).

42. I.-K. Jang, G. J. Tearney, B. MacNeill, M. Takano, F. Moselewski, N. Iftima, M. Shishkov, S. Houser, H. T. Aretz, and E. F. Halpern, "In vivo characterization of coronary atherosclerotic plaque by use of optical coherence tomography," Circulation **111**, 1551-1555 (2005).

43. M. J. Suter, S. K. Nadkarni, G. Weisz, A. Tanaka, F. A. Jaffer, B. E. Bouma, and G. J. Tearney, "Intravascular optical imaging technology for investigating the coronary artery," JACC: Cardiovascular Imaging **4**, 1022-1039 (2011).

44. L. Marcu, "Fluorescence lifetime in cardiovascular diagnostics," J. Biomed. Opt. **15**, 011106 (2010).

45. L. Marcu, Q. Fang, J. A. Jo, T. Papaioannou, A. Dorafshar, T. Reil, J.-H. Qiao, J. D. Baker, J. A. Freischlag, and M. C. Fishbein, "In vivo detection of macrophages in a rabbit atherosclerotic model by time-resolved laser-induced fluorescence spectroscopy," Atherosclerosis **181**, 295-303 (2005).

46. Z. Wang, D. Durand, M. Schoenberg, and Y. Pan, "Fluorescence guided optical coherence tomography for the diagnosis of early bladder cancer in a rat model," The Journal of urology **174**, 2376-2381 (2005).

47. S. Warren, K. Pope, Y. Yazdi, A. J. Welch, S. Thomsen, A. L. Johnston, M. J. Davis, and R. Richards-Kortum, "Combined ultrasound and fluorescence spectroscopy for physico-

chemical imaging of atherosclerosis," Biomedical Engineering, IEEE Transactions on **42**, 121-132 (1995).

48. P. Libby, M. DiCarli, and R. Weissleder, "The vascular biology of atherosclerosis and imaging targets," J. Nucl. Med. **51**, 33S-37S (2010).

49. J. W. Kim and F. A. Jaffer, "Emerging molecular targets for intravascular imaging of high-risk plaques," Curr Cardiovasc Imaging Rep **3**, 237-247 (2010).

50. U. Utzinger and R. R. Richards-Kortum, "Fiber optic probes for biomedical optical spectroscopy," J. Biomed. Opt. **8**, 121-147 (2003).

51. Z. Yaqoob, J. Wu, E. J. McDowell, X. Heng, and C. Yang, "Methods and application areas of endoscopic optical coherence tomography," Journal of biomedical optics **11**, 063001-063001-063019 (2006).

52. H. G. Bezerra, M. A. Costa, G. Guagliumi, A. M. Rollins, and D. I. Simon, "Intracoronary optical coherence tomography: a comprehensive review: clinical and research applications," JACC: Cardiovascular Interventions **2**, 1035-1046 (2009).

53. G. Tearney, M. Brezinski, J. Fujimoto, N. Weissman, S. Boppart, B. Bouma, and J. Southern, "Scanning single-mode fiber optic catheter–endoscope for optical coherence tomography," Opt. Lett. **21**, 543-545 (1996).

54. V. X. D. Yang, Y. X. Mao, N. Munce, B. Standish, W. Kucharczyk, N. E. Marcon, B. C. Wilson, and I. A. Vitkin, "Interstitial Doppler optical coherence tomography," Opt. Lett. **30**, 1791-1793 (2005).

55. W. Jung, W. Benalcazar, A. Ahmad, U. Sharma, H. Tu, and S. A. Boppart, "Numerical analysis of gradient index lens–based optical coherence tomography imaging probes," Journal of biomedical optics **15**, 066027-066027-066010 (2010).

56. K. S. Lee and F. S. Barnes, "Microlenses on the end of single-mode optical fibers for laser applications," Applied optics **24**, 3134-3139 (1985).

57. C. Duan, J. Sun, S. Samuelson, and H. Xie, "Probe alignment and design issues of microelectromechanical system based optical coherence tomography endoscopic imaging," Applied optics **52**, 6589-6598 (2013).

58. S. Y. Ryu, H. Y. Choi, J. Na, W. J. Choi, and B. H. Lee, "Lensed fiber probes designed as an alternative to bulk probes in optical coherence tomography," Applied optics **47**, 1510-1516 (2008).

59. U. Sharma and J. U. Kang, "Common-path optical coherence tomography with side-viewing bare fiber probe for endoscopic optical coherence tomography," Review of Scientific Instruments **78**, 113102 (2007).

60. W. A. Benalcazar, W. Jung, and S. A. Boppart, "Aberration characterization for the optimal design of high-resolution endoscopic optical coherence tomography catheters," Opt. Lett. **37**, 1100-1102 (2012).

61. J. Eom, Y. Kim, S. Lee, E. Min, S. Park, and B. Lee, "Ball lens based lensed patch cord probes for optical coherence tomography in the field of dentistry," Optics Communications **285**, 4333-4337 (2012).

62. M. Abran, G. Cloutier, M.-H. R. Cardinal, B. Chayer, J.-C. Tardif, and F. Lesage, "Development of a Photoacoustic, Ultrasound and Fluorescence Imaging Catheter for the Study of Atherosclerotic Plaque," Biomedical Circuits and Systems, IEEE Transactions on **8**, 696-703 (2014).

63. Y.-C. Chang, J. Y. Ye, T. Thomas, Y. Chen, J. R. Baker, and T. B. Norris, "Two-photon fluorescence correlation spectroscopy through a dual-clad optical fiber," Optics express **16**, 12640-12649 (2008).

64. H. Yoo, J. W. Kim, M. Shishkov, E. Namati, T. Morse, R. Shubochkin, J. R. McCarthy, V. Ntziachristos, B. E. Bouma, F. A. Jaffer, and G. J. Tearney, "Intra-arterial catheter for simultaneous microstructural and molecular imaging in vivo," Nat. Med. **17**, 1680-1684 (2011).

65. B. E. Saleh, M. C. Teich, and B. E. Saleh, *Fundamentals of photonics* (Wiley New York, 1991), Vol. 22.

66. F. Mitschke and F. Mitschke, *Fiber optics* (Springer, 2016).

67. D. Marcuse, "Loss analysis of single‐mode fiber splices," Bell System Technical Journal **56**, 703-718 (1977).

68. J. R. Lakowicz, *Principles of fluorescence spectroscopy* (Springer Science & Business Media, 2013).

69. W. Kim, X. Chen, J. A. Jo, and B. E. Applegate, "Lensless, ultra-wideband fiber optic rotary joint for biomedical applications," Opt. Lett. **41**, 1973-1976 (2016).

70. W. A. Rutala and D. J. Weber, "Disinfection and sterilization: an overview," American journal of infection control **41**, S2-S5 (2013).

71. M. Silindir and A. Y. Özer, "Sterilization methods and the comparison of E-beam sterilization with gamma radiation sterilization," Fabad Journal of Pharmaceutical Sciences **34**, 43 (2009).

72. T. Treibitz, Z. Murez, B. G. Mitchell, and D. Kriegman, "Shape from fluorescence," in *European Conference on Computer Vision*, (Springer, 2012), 292-306.

73. Y. Sun, R. Liu, D. S. Elson, C. W. Hollars, J. A. Jo, J. Park, Y. Sun, and L. Marcu, "Simultaneous time-and wavelength-resolved fluorescence spectroscopy for near real-time tissue diagnosis," Opt. Lett. **33**, 630-632 (2008).

74. A. N. S. Institute, *American National Standard for Safe Use of Lasers* (Laser Institute of America, 2007).

75. S. Shrestha, M. J. Serafino, J. Rico-Jimenez, J. Park, X. Chen, S. Zhaorigetu, B. L. Walton, J. A. Jo, and B. E. Applegate, "Multimodal optical coherence tomography and fluorescence lifetime imaging with interleaved excitation sources for simultaneous endogenous and exogenous fluorescence," Biomedical Optics Express **7**, 3184-3197 (2016).

76. M. Zuker, A. Szabo, L. Bramall, D. Krajcarski, and B. Selinger, "Delta function convolution method (DFCM) for fluorescence decay experiments," Review of scientific instruments **56**, 14-22 (1985).

77. H. D. Vishwasrao, A. A. Heikal, K. A. Kasischke, and W. W. Webb, "Conformational dependence of intracellular NADH on metabolic state revealed by associated fluorescence anisotropy," Journal of Biological Chemistry **280**, 25119-25126 (2005).

78. Q. Fang, T. Papaioannou, J. A. Jo, R. Vaitha, K. Shastry, and L. Marcu, "Time-domain laser-induced fluorescence spectroscopy apparatus for clinical diagnostics," Review of Scientific Instruments **75**, 151-162 (2004).

79. J. Park, J. A. Jo, S. Shrestha, P. Pande, Q. Wan, and B. E. Applegate, "A dual-modality optical coherence tomography and fluorescence lifetime imaging microscopy system for simultaneous morphological and biochemical tissue characterization," Biomed. Opt. Express **1**, 186-200 (2010).

80. Y. Kawase, Y. Suzuki, F. Ikeno, R. Yoneyama, K. Hoshino, H. Q. Ly, G. T. Lau, M. Hayase, A. C. Yeung, and R. J. Hajjar, "Comparison of nonuniform rotational distortion between mechanical IVUS and OCT using a phantom model," Ultrasound in medicine & biology **33**, 67-73 (2007).

81. G. van Soest, J. G. Bosch, and A. F. van der Steen, "Azimuthal registration of image sequences affected by nonuniform rotation distortion," IEEE Transactions on Information Technology in Biomedicine **12**, 348-355 (2008).

82. I. Nuritdinov, K. Y. Masharipov, and M. Doniev, "Formation of radiation-induced defects in silica glasses at high irradiation temperatures," Glass physics and chemistry **29**, 11-15 (2003).

83. P. S. Hsu, W. D. Kulatilaka, S. Roy, and J. R. Gord, "Investigation of optical fibers for high-repetition-rate, ultraviolet planar laser-induced fluorescence of OH," Applied optics **52**, 3108-3115 (2013).

84. B. E. Sherlock, C. Li, X. Zhou, A. Alfonso-Garcia, J. Bec, D. Yankelevich, and L. Marcu, "Multiscale, multispectral fluorescence lifetime imaging using a double-clad fiber," Opt. Lett. **44**, 2302-2305 (2019).

85. A. M. Lee, H. Pahlevaninezhad, V. X. Yang, S. Lam, C. MacAulay, and P. Lane, "Fiber-optic polarization diversity detection for rotary probe optical coherence tomography," Opt. Lett. **39**, 3638-3641 (2014).

86. M. J. Serafino, B. E. Applegate, and J. A. Jo, "Direct frequency domain fluorescence lifetime imaging using field programmable gate arrays for real time processing," Review of Scientific Instruments **91**, 033708 (2020).

87. J. J. Rico-Jimenez, M. J. Serafino, S. Shrestha, X. Chen, W. Kim, J. Adame, L. M. Buja, D. Vela, B. E. Applegate, and J. A. Jo, "Automated detection of superficial macrophages in atherosclerotic plaques using autofluorescence lifetime imaging," Atherosclerosis **285**, 120-127 (2019).

88. S. Shrestha, B. E. Applegate, J. Park, X. Xiao, P. Pande, and J. A. Jo, "High-speed multispectral fluorescence lifetime imaging implementation for in vivo applications," Opt. Lett. **35**, 2558-2560 (2010).